THEORETICAL AND EXPERIMENTAL STUDIES OF WAVE PROPAGATION IN VISCOELASTIC MATERIALS

Thesis by

Robert James Arenz

In Partial Fulfillment of the Requirements

For the Degree of

Doctor of Philosophy

California Institute of Technology

Pasadena, California

1964

ACKNOWLEDGMENTS

It is a pleasure to express my appreciation to Professor M. L. Williams for suggesting the problem areas considered and for his direction of this study.

I am also indebted to Drs. R. A. Schapery and W. G. Knauss for helpful discussions, and to Dr. R. F. Landel of the California Institute of Technology Jet Propulsion Laboratory for making his laboratory facilities available for the determination of material properties.

Thanks are due to Mrs. Martha Lamson and Mr. Marc Kaufman of the California Institute of Technology Computing Center for their assistance in programming the numerical calculations for the Burroughs 220 and IBM 7090 computers.

I wish to thank Mrs. Elizabeth Fox for her excellent work in typing the manuscript and Mrs. Betty Wood for her assistance in lettering the figures.

Three David L. Murray and Institute scholarships during the course of this research are also gratefully acknowledged. Part of this research was supported by the United States Navy Bureau of Ordnance, Naval Ordnance Test Station, China Lake, California and the United States Air Force Special Weapons Center, Kirtland Air Force Base, New Mexico.

ABSTRACT

The phenomenon of wave propagation in viscoelastic materials is investigated both theoretically and experimentally, with attention directed to two areas. First, analytical methods of solution are developed for certain wave propagation problems in one and two dimensions utilizing realistic material properties. This is accomplished by use of time-dependent material property characterization through a Dirichlet series representation to overcome the limitations of the widely-used simple spring and dashpot models involving two or three elements. The Laplace transformed solutions are then inverted by an extension of the Schapery collocation method to dynamic situations.

The second topic deals with dynamic photoelasticity applied to viscoelastic materials. It is shown that the relationships between stress optic and strain optic coefficients for linearly viscoelastic materials can be formulated. Then the time-dependent birefringence characteristics of a typical low modulus polymer material are determined from constant strain rate tests for a full range of dynamic loading rates by taking advantage of the time-temperature shift phenomenon. Much recent work in dynamic photoviscoelasticity has been based on static calibrations only. Hence to put the technique on a firm foundation and indicate the general necessity of including the time dependency in treatment of material properties, a comparison is made of predicted fringe patterns with experimental results for both one- and two-dimensional situations. The cases considered are the rod and semi-infinite plate geometries under quasi-step pressure inputs, for which viscoelastic solutions are obtained from the wave propagation analysis in the first part of the thesis. The results indicate the feasibility of quantitative photoviscoelasticity for dynamic stress analysis.

TABLE OF CONTENTS

PART	TITLE	PAGE
	INTRODUCTION	1
I	LINEAR THEORY OF ONE-DIMENSIONAL WAVE PROPAGATION	4
	A. WAVES IN ELASTIC RODS	4
	B. VISCOELASTIC ANALYSIS	5
	1.1 Mathematical Formulation	6
	1.2 Standard Linear Solid Material	11
	1.3 Realistic Viscoelastic Material	18
	1.4 Results	20
	1.5 Discussion	23
II	WAVES IN TWO DIMENSIONS	24
	A. VISCOELASTIC HALF-SPACE	25
	2.1 Mathematical Formulation	25
	2.2 Stress-Strain Relations	31
	2.3 Laplace Transform Inversion	33
	B. SEMI-INFINITE THIN PLATE	42
III	DYNAMIC BIREFRINGENCE IN VISCOELASTIC MATERIAL	48
	A. GENERAL PHOTOVISCOELASTIC CONSIDERATIONS	48
	B. CHARACTERIZATION OF PHOTOVISCOELASTIC MATERIALS	51
	3.1 Test Apparatus and Procedure	52
	3.2 Determination of Stress Relaxation Modulus	55
	3.3 Determination of Relaxation Birefringence-Strain Coefficient	60
	3.4 Conversion to Creep Birefringence-Stress Coefficient	64

INTRODUCTION

Dynamic analysis in viscoelastic media has received increasing attention in recent years. Distinguished by a strong sensitivity to rate and temperature effects, viscoelastic materials are making their appearance in such diverse uses as binder for solid propellant rockets, shock-absorbing mountings and various structural applications, many of which are subject to impulsively applied loads. Hence in addition to the usual effect of the time parameter in the resulting vibration or stress wave phenomena, there arises the possibility of direct interaction between loading input and basic material properties. This interplay leads to analytical complications which so far have been adequately resolved only in elementary geometries or simple mathematical characterizations of the viscoelastic material in question.

Pioneering work in the treatment of materials possessing both elastic and viscous characteristics centered on theoretical representation of mechanical properties by simple spring and dashpot models of two or three elements. Lacking a stimulus to further refinement for many years, the analysis remained largely on this level until the introduction of materials with broad-band response characteristics demonstrated the necessity of more realistic material representation.

The first portion of this dissertation presents a method of dynamic analysis in linearly viscoelastic media involving a special series representation of mechanical properties designed to overcome the limitations of the simple model approach. Indeed, it seems appropriate to take up again the whole field of dynamic viscoelastic

analysis; hence a solution technique is proposed involving the extension to dynamic situations of a collocation Laplace transform inversion procedure previously used for static problems. The combination of these two features makes possible the more accurate solution of many problems in viscoelastodynamics. Part I treats the problem of the wave propagation in a semi-infinite uniaxial rod subjected to a step load input at its end. Associated two-dimensional problems for the plane strain and plane stress analysis of a semi-infinite medium loaded by a step pressure pulse moving along the boundary are considered in Part II.

The subject of quantitative photoviscoelasticity also requires development inasmuch as the optical as well as mechanical properties of pertinent materials are also time and temperature dependent. It appears that until very recently experimentalists have not made a comprehensive attempt to characterize these properties simultaneously, especially for dynamic investigations where they are important factors. Indeed, much of the present research originated in a photoelastic test program to simulate the dynamic stresses due to ground shock loading. The results of this program, reported in Part IV, are based upon the theoretical relations and dynamic birefringence calibration methods detailed in Part III as illustrated experimentally using Hysol 8705, a high polymer synthetic rubber. It will be seen that a number of the analytical features of the early part of the thesis prove to be equally powerful in developing the photoviscoelastic relations.

Predicted photoviscoelastic fringe patterns from the theoretical stress solutions of Parts I and II using the birefringence data of Part III are compared with high-speed camera results from similar experimental

situations in Part IV, where the equipment and procedures used in the tests are also described.

The research reported here is designed to provide more accurate analytic solutions to dynamic viscoelastic problems by using realistic material property representations, to serve as a means of checking the applicability of the simple model approach, and to illustrate the feasibility of quantitative photoviscoelastic analysis for the determination of dynamic stresses.

PART I

LINEAR THEORY OF ONE-DIMENSIONAL WAVE PROPAGATION

The analysis of wave propagation in solid media generally involves two rather different sorts of problems. The first consists of writing the differential equation of motion and associated boundary and initial conditions for the geometry and material considered. The other and frequently more difficult task is the solution of this equation. Wave effects in viscoelastic materials illustrate this point quite strikingly.

A. WAVES IN ELASTIC RODS

Before treating the viscoelastic problem, a brief survey of the approaches taken in the case of elastic wave propagation in a rod will illuminate several aspects of the situation. Kolsky (1) has outlined the basic problem involving low-frequency plane longitudinal waves in a semi-infinite rod which result in non-dispersive propagation. The effect of lateral inertia was incorporated by Rayleigh (2) in a first order correction applicable at the low end of the frequency spectrum.

The exact equations from linear elasticity for an infinite train of waves were derived by Pochhammer (3) and Chree (4); their solution, in which a frequency equation is generated by the requirement of a traction-free rod surface, pointed out the nature of the geometric dispersion to be expected. At input wave lengths either small or large compared to the thickness of the rod, a constant wave propagation speed is expected; in between these limits a gradual

reduction in the speed of the fundamental mode with decreasing wave length occurs. Basically this represents the effect of a boundary with associated reflections as the wave moves down the rod. Precise numerical solutions of the Pochhammer-Chree equations by Davies (5) indicated the propagation characteristics of the various modes. At the conclusion of the present analysis some comments will be made regarding the effect of these factors on the waves in viscoelastic media.

B. VISCOELASTIC ANALYSIS

The specific case of a one-dimensional viscoelastic rod loaded dynamically in compression has been discussed previously by Lee and Morrison (6) using idealized model representations of the viscoelastic material. It is proposed to treat the same problem using a more general and complete representation (7) of mechanical properties based on the actual rate or time dependency of real viscoelastic materials; this dependency is found to spread over a fairly large number of decades of logarithmic time (or frequency of input).

The Laplace transform approach is suited to problems involving the propagation of transient effects and forms the basis for this analysis. As compared to the case of elastic solids however, with viscoelastic media one faces the two additional complications of representing the time-dependent material properties and then inverting the transformed equations of motion subject to this added complexity.

Information of a sort can usually be extracted if a wave front expansion and long-time solution are employed (8), but it is always

hoped that a more complete solution is possible. An approach widely applied in the past ten years is the use of model representation. Kolsky (9) has pointed out that most researchers have found that a realistic material representation extending over about ten decades of log time leads to a prohibitive numerical calculation problem. As a result the use of simple spring and dashpot models incorporating two to four elements has been customary. These are adequate to cover one or two decades of log time but fail quite badly for larger ranges of time (or equivalently, frequency). To overcome this rather basic limitation, especially in engineering as opposed to qualitative situations, the present analysis provides techniques suitable for solving certain wave propagation problems using realistic broad-band viscoelastic material properties. It depends on a method of material characterization utilizing a Dirichlet series representation of the operational modulus, and then a numerical collocation inversion process to obtain the wave propagation solution. As with all numerical techniques, the example is more restrictive than a fully analytical solution, but it nevertheless reveals several features believed to be typical of wave propagation in viscoelastic media.

1.1 Mathematical Formulation

To illustrate the method of solution, consider the one-dimensional problem of wave propagation in a thin semi-infinite rod. The loading on the end of the rod will consist of a step input which can be either a stress or a displacement boundary condition. Since primary interest is centered in viscoelastic effects, we assume no geometric dispersion, i.e., no lateral inertia effects

will be taken into account. As noted above, several authors have treated this aspect in elastic analysis; hence we can estimate the importance of this effect to the viscoelastic problem. Indeed, it will be seen that the higher frequency components of the step loading are rapidly attenuated. Consequently, the geometric dispersion is less severe than it otherwise would be.

If x is the coordinate along the rod axis, the corresponding one-dimensional equation of motion is

$$\partial\sigma/\partial x = \rho\, \partial^2 u/\partial t^2 \tag{1.1}$$

where

$\sigma(x,t)$ = uniaxial stress

ρ = mass density of the material

$u(x,t)$ = displacement in the x-direction.

The boundary condition imposed at the end is assumed to be either

$$\sigma(0,t) = \sigma_0 H(t) \tag{1.2a}$$

or

$$u(0,t) = u_0 H(t) \tag{1.2b}$$

where H(t) is the Heaviside step function.

Assuming the rod to be initially undisturbed, the Laplace transform (designated by a bar over the variable) of (1.1) yields an ordinary differential equation,

$$d\bar{\sigma}/dx = \rho\, p^2\, \bar{u} \tag{1.3}$$

because the transform parameter p can be treated as a constant until the final inversion.

To complete the formulation of a displacement equation of motion from 1.3 requires a relation between the stress and displacement. The most general kind of linear stress-strain relation is deduced by means of Boltzmann's superposition principle and takes the form of an integral equation. Gross (10) gives two alternative forms for this equation:

$$\epsilon(t) = \int_{-\infty}^{t} \chi(t-\tau) \frac{d\sigma(\tau)}{d\tau} d\tau \tag{1.4}$$

$$\sigma(t) = \int_{-\infty}^{t} \phi(t-\tau) \frac{d\epsilon(\tau)}{d\tau} d\tau \tag{1.5}$$

where $\chi(t)$ and $\phi(t)$ are "memory" functions and the integrals are described as "hereditary." If, following the formulation of Berry and Hunter (11), we put

$$\chi(t) = a + bt + \theta(t) \tag{1.6}$$

$$\phi(t) = a' + b'\delta(t) + \psi(t) \tag{1.7}$$

where a, b, a', b' are numerical constants (which may assume the value zero depending on the particular material), and $\delta(t)$ is the Dirac delta function, then the functions $\theta(t)$ and $\psi(t)$ correspond, respectively, to the creep and relaxation functions of Gross. The former, $\theta(t)$, is associated with the strain response to a step stress input and is monotonic increasing with the value zero at $t = 0$. The latter, $\psi(t)$, is associated with the stress response to a step strain input and is

monotonic decreasing with the value zero at t = ∞. Gross (10) derives the conditions under which the equations 1.4 and 1.5 are compatible.

The creep function $\theta(t)$ is often represented in terms of a retardation spectrum $L(\tau)$, which is a distribution function of retardation times of strain, by the integral

$$\theta(t) = \theta(\infty) \int_0^\infty L(\tau)\ (1 - e^{-t/\tau})\ d\tau \tag{1.8}$$

where $\theta(\infty)$ serves as a normalizing factor. In a similar way, the relaxation function $\psi(t)$ can be expressed in terms of a relaxation spectrum $H(\tau)$ thus:

$$\psi(t) = \psi(0) \int_0^\infty H(\tau)\ e^{-t/\tau}\ d\tau\ . \tag{1.9}$$

When the distributions degenerate into discontinuous line spectra, that is, when

$$\theta(\infty)\ L(\tau) = \sum_i A_i\ \delta(\tau - \tau_i) \tag{1.10}$$

and

$$\psi(0)\ H(\tau) = \sum_i B_i\ \delta(\tau - \tau_i') \tag{1.11}$$

it is found (11) that

$$\theta(t) = \sum_i A_i\ (1 - e^{-t/\tau_i}) \tag{1.12}$$

and

$$\psi(t) = \sum_i B_i \, e^{-t/\tau_i'} \tag{1.13}$$

In this case it can be shown that the stress-strain relation can be written as the partial differential equation

$$a_0 \sigma + a_1 \frac{\partial \sigma}{\partial t} + \ldots + a_n \frac{\partial^n \sigma}{\partial t^n} = b_0 \epsilon + b_1 \frac{\partial \epsilon}{\partial t} + \ldots + b_m \frac{\partial^m \epsilon}{\partial t^m} \tag{1.14}$$

where the $a_0, \ldots, a_n, b_0, \ldots, b_m$ are numerical constants (for isothermal conditions). The line spectra and 1.14 can be shown to represent physically a combination of spring and/or dashpot elements in series or parallel whose spring moduli and dashpot viscosities are proportional to the constants. In the limit as n and m approach infinity, the two formulations 1.14 and 1.4 (or 1.5) become equivalent.

It is the differential equation form that is found here more convenient. Hence the one-dimensional viscoelastic stress-strain relationship (12) is formulated as

$$P\sigma = Q\epsilon \tag{1.15}$$

where P and Q stand for the linear differential operators of the form $\sum_{i=0}^{n} a_i \, \partial^i/\partial t^i$. Transforming 1.15 and using the strain-displacement relation gives

$$\bar{\sigma}(x,p) = [Q(p)/P(p)] \; \bar{\epsilon}(x,p) = [Q(p)/P(p)] \; d\bar{u}(x,p)/dx \tag{1.16}$$

where P and Q now become algebraic operators in the Laplace transform parameter p. If the indicated division can be carried out, the operational tensile modulus is defined as

$$E(p) = Q(p)/P(p) \ . \tag{1.17}$$

Combining 1.16 and 1.17 with 1.3 gives

$$E(p)d^2\bar{u}/dx^2 = \rho p^2 \bar{u} \tag{1.18}$$

which has only the solution

$$\bar{u}(p) = Ae^{-xp/c(p)} \tag{1.19}$$

where

$$c(p) = \sqrt{E(p)/\rho} = \text{"operational" wave speed} \tag{1.20}$$

because the positive exponential solution has been rejected since only outgoing waves are permitted by the physics of the situation.

1.2 Standard Linear Solid Material

In general, a large number of terms would be required in the operators P and Q of 1.15 to represent a real material; however, as pointed out above, the studies done heretofore have employed only very restricted model representations of two to four elements. Hence, in order to compare later with the method of analysis to be proposed, we first consider the case of a standard linear solid to which an integral solution has been given by Morrison (13). The model consists of three elements, a spring of modulus E' in series with a dashpot of viscosity coefficient $1/\mu$, both in parallel with a spring E. In Morrison's notation, the relationship of stress (σ') to strain (ϵ) is

$$(1/E')\, d\sigma'/dt + \mu\sigma' = (1 + E/E')\, d\epsilon/dt + E\mu\epsilon \ . \tag{1.21}$$

Thus an analytic expression of the form of 1.15 is available for this simple model representation. Morrison has shown that the resulting one-dimensional differential equation of motion in terms of stress is identical in form to that for displacement; hence the solution expressions have the same form also, provided the initial and boundary conditions are of the same type. In terms of the dimensionless time τ' after the arrival of the fastest (glassy) wave where c_G is the dimensionless glassy wave speed in the material, Morrison's transformed solution for a step pressure input of magnitude σ_0 and the special case E = E' is

$$\overline{S}'(\xi,p') = (1/p') \exp\{-\xi p'[(1+p')^{\frac{1}{2}}/(1+2p')^{\frac{1}{2}} - 1/(2)^{\frac{1}{2}}]\} \qquad (1.22)$$

where

$S' = \sigma'/\sigma_0$ = dimensionless stress

$\xi = (\rho E)^{\frac{1}{2}} \mu x$ = dimensionless distance

$\tau = E\mu t$ = dimensionless time

$\tau' = \tau - \xi/c_G$

p' = Laplace transform parameter corresponding to τ'.

Morrison carries out an inversion by a rather involved numerical integration of the inversion integrals to obtain the final solution for S'. Of course, an asymptotic expansion of $p'\overline{S}'$, evaluated as $p' \to \infty$, gives the wave front stress.

Before discussing the Morrison results, we briefly describe and then apply a more widely applicable method of Laplace transform inversion to be used in several phases of this study. Actually two inversion techniques are proposed; both methods have been formulated

in some detail for other applications by Schapery (11, 12). The first is a very rapid approximation technique suitable for step function inputs termed the direct method; it depends on the condition that the derivative with respect to log time of the ultimate time dependent solution $(dS'(\tau')/d(\log \tau'))$ is a slowly varying function of log time. Correspondingly it is found that $d[p'\bar{S}'(p')]/d[\log p']$ must be a slowly varying function of log p'. If this condition holds over approximately a two-decade interval, then a Taylor's series expansion of the solution shows that a reasonably good approximate inversion is given by

$$S'(\tau') = [p'\bar{S}'(p')]_{p'=\frac{1}{2\tau'}} . \tag{1.23}$$

This is an extremely rapid method to apply and as we shall see yields very informative results. The short time limit ($p' \to \infty$) is recognized as giving the glassy wave front stress value while the long-time stress behavior is given by the limit as $p' \to 0$.

The second and more versatile inversion technique, in contrast to the direct method, is readily used with the Duhamel integral to give the response to other than step function loads. It is a collocation procedure in which the transient part of the solution is represented by a Dirichlet series of decaying exponentials:

$$\Delta S'_D(\tau') = \sum_{i=1}^{n} S_i e^{-\tau'/\gamma_i} . \tag{1.24}$$

Again without going into details, it suffices to point out heuristically that viscoelastic materials have exponential stress relaxation characteristics and the above expression ingeniously allows a wide spectrum

of relaxation times, e.g., a reasonably large number of springs and dashpots may be incorporated in the material representation.

The γ_i in 1.24 are positive constants prescribed in such a way as to provide adequate coverage of the time spectrum and the S_i are unspecified constants to be evaluated by minimizing the total square error between the actual $\Delta S'$ and $\Delta S'_D$ given by the series. This minimizing procedure for a step loading leads to the relations

$$\sum_{j=1}^{n} \frac{S_j}{1+\frac{\gamma_i}{\gamma_j}} = [p'\Delta \bar{S}'(p')]_{p'=\frac{1}{\gamma_i}} \; ; \; i = 1, 2, \ldots\ldots, n \qquad (1.25)$$

which constitute a set of simultaneous equations for n different values of p' which are solved for S_i. Thus the collocation consists of a matching up of the summation on the left hand side of 1.25 with the calculated values of $p'\Delta\bar{S}'(p')$ for various values of real, positive p'. Hence the inversion procedure consists essentially in being able to determine the values of the transform all along the positive real p' axis. By considering the thermodynamics of irreversible processes and certain variational principles, Schapery (12) has shown for static and quasi-static situations the singularities of the Laplace transform of viscoelastic stress or strain occur only on the non-positive real axis. His analysis did not consider the question of the validity of this representation in dynamic problems. But besides the encouraging fact that it is a least squares procedure, the series representation $\sum_{i=1}^{\infty} S_i e^{-\tau'/\gamma_i}$ turns out to be complete under certain conditions. Erdelyi (13) has shown that an infinite sequence of functions $e^{-\tau'/\gamma_i}$ is complete with respect to all quadratically integrable functions

over $0 < \tau' < \infty$ if the infinite series

$$\sum_{i=1}^{\infty} \gamma_i/(1 + \gamma_i^2)$$

is divergent. Since we use only a finite number of terms of the series, the divergence requirement can be satisfied by proper choice of the γ_i for large i. Thus it is mathematically guaranteed that the square error can be made arbitrarily small.

A note of caution is necessary on the use of this series. Increased accuracy is normally expected by taking successively larger numbers of terms in the series. However, at the same time, commensurate accuracy in the evaluation of $p\overline{S}'(p)$ is required in order that minor deviations in the transformed values, which sometimes occur in series representations and usually introduce amplified departures from the correct inverted values, are held to an acceptably small level.

With these conditions satisfied, the total time solution from 1.24 with the S_i obtained from 1.25 is given by

$$S'(\tau') = S_0 + \sum_{i=1}^{n} S_i e^{-\tau'/\gamma_i} \tag{1.26}$$

where S_0 can be evaluated by examining the behavior of $p'\overline{S}'(p')$ as p' tends to zero (long time solution).

We are now in a position to complete the comparison of Morrison's solution with the new results. Applying these various inversion procedures to the problem of wave propagation in standard linear solid

material gives the results shown in fig. 1 for the position $\xi = 2$. The direct method solution is of course the same curve as that of $p'\overline{S}'(p')$ but is associated with the abscissa $\log \tau'$ rather than $\log p'$. The collocation solution was carried out with a ten term series and is shown only as a number of computed points since it is too close to Morrison's integral solution to require drawing another curve.

It may be noted that the direct solution has a less steep rise than the more exact methods; this proves to be true in general for these methods. Another item of interest is the inflection point on the direct solution curve. Calculations for other positions along the rod show that the farther one goes down the rod, the closer the inflection point approaches τ'_R, the arrival time of the slowest moving or rubbery wave component of the input loading.

Indeed we can show theoretically that this is generally true for viscoelastic rods provided the point of interest is far enough from the loaded end. If the transformed solution 1.22 is substituted in the inflection condition

$$\frac{d^2(p'\overline{S}')}{d(\log p')^2} = 0 \qquad (1.27a)$$

and simplified by using the representation in 1.19, we have

$$e^{-\frac{\xi p'}{c}} \left\{ \frac{d^2(\frac{\xi p'}{c})}{d(\log p')^2} + \left[\frac{d(\frac{\xi p'}{c})}{d(\log p')} \right]^2 \right\} = 0 .$$

Introducing the appropriate derivatives gives

$$-\frac{1}{c^2}\frac{d^2c}{d(\log p')^2}+\frac{2}{c^3}\left(\frac{dc}{d\log p'}\right)^2+\left(1-\frac{\xi p'}{c}\right)\left[2\left(-\frac{1}{c^2}\frac{dc}{d\log p'}+\frac{1}{c}\right)\right]$$

$$-\xi p'\left[-\frac{1}{c^2}\frac{dc}{d\log p'}\right]^2=0\ .$$

Employing the definition 1.20 and simplifying gives

$$\left(1-\frac{\xi p'}{c}\right)\left[1-\frac{1}{2}\frac{d(\log E)}{d(\log p')}\right]^2=\frac{d^2(\log E)}{d(\log p')^2}\ . \qquad (1.27b)$$

Since the value of c is always bounded, when ξ becomes large p' must become small to satisfy this equation, which implies that c approaches the rubbery wave speed c_R. Indeed, for small p' the operator derivatives in 1.27b approach zero so that $\xi p' \doteq c$ and the relation of ξ and p' is explicitly demonstrated.* Hence for the condition of increasing ξ where the rubbery arrival time t_R from the instant of loading approximates t'_R (since the glassy speed is roughly 30 times greater than the rubbery speed), the inflection point in $p'\overline{S}'$ does converge to the rubbery arrival time.

In fig. 1, the glassy wave front stress level corresponds to the horizontal asymptote to the left at a value of $S'_G = 0.702$; this front arrives at $\tau'_G = 0$ or in terms of time from the instant of loading, $\tau_G = (2)^{\frac{1}{2}}$. Also to be noted is the fact that the entire build up of the response occurs in approximately two decades of log time; this rather

* Note also that a similar argument for the degenerate case of large p' indicates as it should that $\xi \to 0$, i.e., the inflection point coincides with the end of the bar where there is a step response to the applied step load.

narrow spread in the response is the result of the somewhat fictitious simple model representation of the mechanical properties of the medium, including the fact that the low to high modulus ratio is a factor of only two (since E = E').

These same response curves plotted versus actual time from initiation of loading are shown in fig. 2. The collocation solution closely approximates the integral solution, the difference being nowhere greater than 2%. In addition, the integral solution was evaluated numerically and hence may be subject to some error itself. It may also be noted that a 20-term collocation fit produced essentially the same values as the 10 term, thus indicating a high degree of exactness in the results obtained.

The above comparisons, admittedly restricted for illustrative purposes to one station $\xi = 2^*$, are believed to indicate the usefulness and accuracy of the proposed inversion techniques. Hence we next proceed to apply them to the case of an actual viscoelastic material.

1.3 Realistic Viscoelastic Material

The specific material to be considered next is a polyurethane synthetic rubber, chosen because material data are available (14) and because it approximates the material used in some recent experimental wave propagation studies (15). The only new feature in this case is the representation of the material. Whereas we previously had an analytical expression for the stress-strain relationship, i.e. 1.21, the experimental data for the actual material are given in terms of the

*However, similar results were obtained for calculations at $\xi = 1$ and $\xi = 3\sqrt{2}$.

dynamic compliance (reciprocal of modulus) in shear (fig. 3) where the test points have been omitted for clarity. Noticeable immediately is the considerably larger range of ten decades of log time (or equivalently log frequency) between the maximum and minimum compliance values. Consequently a simple model representation as in the case of the standard linear solid will not be sufficient. As a matter of fact, since one spring-dashpot combination works fairly well over one decade, the desired representation might be viewed as a series or summation of such simple models, each responding predominantly to a different decade of the frequency range. Indeed, general linear viscoclastic analysis (16) shows that the approximate representation can be taken as the Kelvin model for which the real part of the complex shear compliance for a fixed temperature is given by

$$J'(\omega) = J_G + \sum_{i=1}^{n} \frac{J_i}{1 + \omega^2 \tau_i^2} \tag{1.28}$$

where

J_G = glassy (high frequency) compliance

J_i = component spring compliances

τ_i = $\eta_i J_i$ = component retardation times

η_i = component dashpot viscosities.

Thus the model is a glassy spring plus n Voigt (parallel spring and dashpot) elements in series.

Using values of $J'(\omega)$ from the experimental data, the values of the J_i for an appropriate choice of the τ_i values can be obtained by

once more using a collocating procedure at n values ω_i. It is usually sufficient to choose the τ_i at one decade intervals so that in the present case n = 9. Once the J_i are determined, the operational compliance required for the transformed solution is given from viscoelastic theory as

$$J(p) = J_G + \sum_{i=1}^{n} \frac{J_i}{1 + p\tau_i} \quad . \tag{1.29}$$

For the case of a polyurethane rod, this time using a step displacement input of magnitude u_0, the transformed solution analogous to 1.22 for the standard linear solid material is given by

$$\frac{p\bar{u}(p)}{u_0} = \exp\left\{-\frac{px}{c_G}\left[\left(\frac{D(p)}{D_G}\right)^{\frac{1}{2}} - 1\right]\right\} \tag{1.30}$$

where D(p) is the operational tensile compliance and c_G is the glassy wave speed. For simplicity, an incompressible material has been assumed so that D = J/3. This assumption is realistic except for the highest frequencies which as we shall see are rapidly attenuated. The exponential in 1.30 can in principle be expanded in powers of 1/p to obtain the glassy wave front value, but it is also more easily available by the computation of $p\bar{u}(p)/u_0$ as $p \to \infty$.

1.4 Results

The matrix inversion of the collocation solution for 1.30 and the summation processes have been carried out on the Burroughs 220 computer; they are standard procedures and are easily accomplished.

The resulting non-dimensional responses are plotted in fig. 4 for three different positions x_1, x_2 and x_3 corresponding to glassy wave arrival times of 10^{-8}, 10^{-4}, and 10^{-2} seconds, respectively. As with the standard linear solid case, the results would be numerically equal in the case of the stress response to a step stress input of the same magnitude. The transform curves of $p\bar{u}(p)/u_0$ and the corresponding direct method solutions (in which p is replaced by $1/2\ t'$) are similar to those of the previous case and again we see the convergence of the inflection point and the "rubbery" arrival time, t'_R, as x increases.

Several striking differences from the former case are evident however in the collocation solution. First is the spread of the response over about five decades of log time compared to two decades for the standard linear solid. This is a result of the inability of the simple model to represent the real viscoelastic properties of such a material as polyurethane*.

Secondly, the glassy wave front decays extremely rapidly as shown by the curve for $x_1 = 0.00167$ cm where the glassy response is $u_G/u_0 = 0.09$. A wave front expansion shows this response at any point x to be given by

$$\frac{u_G(x,t')}{u_0} = H(t')\, e^{-\frac{x}{2c_G D_G} \sum_{i=1}^{9} \frac{D_i}{\tau_i}} . \qquad (1.31)$$

* Subsequent solution of the problem using a standard linear solid representation of the polyurethane material fitted at the inflection point also indicates a shorter overall response time; however, some portions of the response curves in the two cases exhibit comparable slopes.

The predominant term in the summation is for i = 9, and since $\tau_9 = 10^{-9}$ seconds, the relaxation is extremely fast. This corresponds to high viscosity in this element of the model and hence very rapid attenuation of the high frequency components of the input. Consequently we have also verified the earlier comment that geometric dispersion would play a less serious role in this analysis than in the case of an elastic rod. However, this conclusion might well be modified if the applied loading were different from a step function, which has a Fourier spectrum gradually decreasing in amplitude with increasing frequency of the component; the strength of the dispersive effect would be altered, for example, in the case of a delta-function input. As an incidental note, the limit case of purely elastic material is readily apparent from 1.31 since then all the τ_i would be infinite (hence exhibiting no stress relaxation or attenuation).

A third difference is the appearance of dispersion in the response at x_2 and x_3 with the resulting oscillation in the neighborhood of t'_R. This behavior could be predicted by considering a Fourier analysis of the step input into its sinusoidal components, each with a different propagation speed. All the components superpose to produce the input compressive displacement at x = 0 but will disperse as they travel down the rod, some places reinforcing and other places interfering to the extent of producing a tension. It is believed that this phenomenon did not appear in the case of the standard linear solid because its response has only a two decade spread and in addition its change in modulus from low to high

frequency is relatively small (a factor of two compared to approximately 1000 in the polyurethane material under consideration here).

The amplitude of the dispersive oscillations appears to be growing gradually with distance down the rod. However, considerations associated with a Fourier series representation for a step input imply that their ultimate amplitude is limited.

A corresponding plot of the response at a fixed position, x_2, along the bar is shown as a function of time in fig. 5. While the major portion of the rise in response in the figure appears to be somewhat spread out in time due to the scale used, it actually occurs in about 0.003 seconds around t_R.

1.5 Discussion

The foregoing one-dimensional analysis indicates the characteristic behavior to be expected from waves traveling in realistic viscoelastic materials. The high frequency components of the response to a step loading are very rapidly attenuated with distance and the major portion of the stress or displacement rise occurs near the "rubbery" arrival time. This feature suggests additional benefits from the viscoelastic analysis which will be exploited in the two-dimensional solutions to be discussed in Part II. Furthermore the methods of inversion proposed here can be made as accurate as desired for any application simply by taking more terms in the series with no essential increase in mathematical difficulty. It is believed that this property yields a distinct advantage over the analytical model representation used in previous treatments of viscoelastic wave propagation.

PART II

WAVES IN TWO-DIMENSIONS

Very few viscoelastic analyses exist for wave propagation in two dimensions (20). As in the one-dimensional cases, most of those that treat this type of geometry (21, 22, 23) are limited to simple model viscoelastic representations.

The situation with respect to elastic analysis is of course much more complete. Indeed in recent years, numerous investigators have been interested in the effects that moving blast waves on the surface of the earth exert on its interior and in particular on underground structures. The steady motion of a line load on the surface of an elastic half-space has been treated by Sneddon (24) and more completely by Cole and Huth (25). The transient analysis including "start-up" effects near the point of load initiation has been considered by Ang (26) for the "subsonic" case, i.e., the traveling load moves at a speed less than any characteristic elastic wave speed in the material of the half space; extension to the corresponding supersonic case was treated by Arenz (27). Miles (28) has used an asymptotic approximation technique to study the elastic half-space subjected to a radially symmetric step pressure pulse which decays with time.

Additional difficulties are encountered when the two-dimensional material is viscoelastic, but the basic method outlined in Part I can be extended to this situation provided the analysis is applied in turn to each of the stress contributions entering the problem. In Part II the two following cases relevant to the interest

indicated above are treated: (1) a semi-infinite half-space loaded by a traveling plane step pressure input ("ground shock" loading), and (2) a semi-infinite thin plate loaded on the edge in a similar manner. The former is readily identified as a plane strain problem; the latter is a plane stress situation and anticipates the photo analysis experimental treatment of Part IV.

A. THE VISCOELASTIC HALF-SPACE

Consider the semi-infinite geometry of fig. 6 in a Cartesian system of coordinates $x'y'z'$ such that the half-space is represented by $y' \geq 0$. It is subjected to a step pressure loading which extends without limit in the z'-direction and whose front is moving in the negative x-direction with a uniform velocity c_0; it is considered to exert a constant pressure or normal stress p_0 at all places behind the front.

2.1 Mathematical Formulation

If u, v, w are the components of the vector displacement $\vec{u}(x', y', z', t')$, the displacement equation of motion, in the absence of body forces, may be written as

$$(\lambda + 2\mu)\, \nabla (\nabla \cdot \vec{u}) - \mu\, \nabla \times \nabla \times \vec{u} = \rho \frac{\partial^2 \vec{u}}{\partial t'^2} \tag{2.1}$$

where ρ is the material mass density and λ and μ are the Lamé elasticity constants which must now however be considered as time operators in the general viscoelastic formulation. The viscoelastic treatment will correspond to that for the tensile modulus in Part I.

While both Lamé parameters could incorporate viscoelastic effects, several investigations (29, 30) indicate that the bulk modulus

K varies relatively little in the viscoelastic transition region compared to the very pronounced change occurring in the shear modulus. Hence we neglect time effects in bulk but retain viscoelastic characteristics in shear. Thus, for convenience λ is replaced in terms of K and μ by the usual relation

$$\lambda = K - \frac{2}{3}\mu \tag{2.2}$$

so that 2.1 becomes

$$(K + \frac{4}{3}\mu)\,\nabla(\nabla\cdot\vec{u}) - \mu\,\nabla \times \nabla \times \vec{u} = \rho\,\frac{\partial^2 \vec{u}}{\partial t'^2} \tag{2.3}$$

where now only μ is a viscoelastic operator; K is a constant.

Using the Helmholtz resolution, the displacement vector $\vec{u}$ can be represented by a scalar and a vector potential such that

$$\vec{u} = -\nabla\phi + \nabla \times \vec{\psi} \tag{2.4}$$

under the condition that $\nabla\cdot\vec{\psi} = 0$. Thus a solution of 2.3 can be obtained if

$$\nabla^2\phi = \frac{\rho}{K + \frac{4}{3}\mu}\,\frac{\partial^2\phi}{\partial t'^2} \tag{2.5}$$

$$\nabla^2\vec{\psi} = \frac{\rho}{\mu}\,\frac{\partial^2\vec{\psi}}{\partial t'^2} \tag{2.6}$$

which are the dilatation and shear wave equations, respectively. Note however that due to the viscoelastic nature of μ, the wave speeds will not be constant for the dynamic phenomena under consideration.

For the present geometry of unlimited extent in the z'-direction and for the prescribed loading condition, the transverse displacement, w, is zero and the conditions are those of plane strain; hence the vector $\vec{\psi}$ has only one component, the z'-component, which will henceforth be denoted by ψ. Also the scalar potential is $\phi = \phi(x', y', t')$, so that 2.4 has the components

$$u = -\frac{\partial \phi}{\partial x'} + \frac{\partial \psi}{\partial y'} \tag{2.7}$$

$$v = -\frac{\partial \phi}{\partial y'} - \frac{\partial \psi}{\partial x'} \tag{2.8}$$

For the step function pressure load moving in the negative x'-direction, the boundary conditions are

$$\begin{aligned} \sigma_{y'y'}(x', 0, t') &= -p_0 \, H(x' + c_0 t') \qquad x' > 0 \\ &= 0 \qquad\qquad\qquad\qquad x' < 0 \end{aligned} \tag{2.9}$$

$$\sigma_{x'y'}(x', 0, t') = 0 \qquad \text{All } x' \tag{2.10}$$

where $H(x', t')$ is the Heaviside unit step function. Along with these conditions, the waves are required to be diverging, i.e.,

$$\sigma_{y'y'} = \sigma_{x'x'} = \sigma_{x'y'} = 0 \quad \text{at} \quad x' = \infty \, .$$

The approach previously used by Ang (26) in the transient elastic problem of Fourier integral representation of the transformed stresses cannot be readily applied here since the time dependency of the wave speeds appears to place this case beyond the scope of the Cagniard-De Hoop Laplace inversion technique. Thus the most satisfactory

solution for our purposes can be obtained by assuming that the load has been moving for a long time such that a steady state exists with respect to a coordinate system attached to the moving load. A similar problem has been investigated in reference 21 but for the case of the standard linear solid (three-element) model in shear, and only the wave front expansion and long time behavior are given explicitly. As indicated in Part I, the solution method herein is general, can be applied to realistic viscoelastic materials, and gives complete time histories of the response.

Consider now that (x,y,z) denote a coordinate system attached to the front of the moving load, while as before (x',y',z') denote coordinates fixed in the material of the half-space (fig. 6). They are related by the Galilean transformation

$$\begin{aligned} x &= x' + c_0 t' \\ y &= y' \\ z &= z' \\ t &= t' \end{aligned} \tag{2.11}$$

In the new coordinates there is no variation with time and hence the following conversions in derivatives take place:

$$\frac{\partial}{\partial x'} = \frac{\partial}{\partial x}, \quad \frac{\partial}{\partial y'} = \frac{\partial}{\partial y}, \quad \frac{\partial}{\partial t'} = c_0 \frac{\partial}{\partial x} \tag{2.12}$$

This transformation is readily applied to 2.5 and 2.6 with the caution that μ is to be considered as a viscoelastic differential time operator and hence will become effectively an operator in various orders of

$c_0^n \frac{\partial^n}{\partial x^n}$ in the steady state. The result is

$$(K + \tfrac{4}{3}\mu)\,\nabla^2\phi = \rho\, c_0^2\, \phi_{xx} \tag{2.13}$$

$$\mu\,\nabla^2\psi = \rho\, c_0^2\, \psi_{xx} \tag{2.14}$$

where the subscripted coordinates represent partial differentiation. The boundary conditions 2.9 and 2.10 in the new coordinate system are

$$\begin{aligned} \sigma_{yy}(x,0) &= -p_0\, H(x) && x > 0 \\ &= 0 && x < 0 \end{aligned} \tag{2.15}$$

$$\sigma_{xy}(x,0) = 0 \qquad \text{All } x \tag{2.16}$$

It now becomes necessary to specify the speed regime for the moving load. For the present case of interest, it is assumed to travel supersonically relative to the maximum wave speed in the material.* This case not only introduces simplifications into the analysis but will prove useful as a basis for later comparison to an experimental situation. Since no stress signal can precede the load and thus quiescent conditions exist for $x < 0$, the usual one-sided Laplace transform in the space-variable x can be applied to 2.13 and 2.14, yielding

$$[K + \tfrac{4}{3}\mu\,(c_0 p)]\,[p^2\overline{\phi} + \overline{\phi}_{yy}] = \rho\, c_0^2\, p^2\, \overline{\phi} \tag{2.17}$$

$$\mu(c_0 p)\,[p^2\,\overline{\psi} + \overline{\psi}_{yy}] = \rho\, c_0^2\, p^2\, \overline{\psi} \tag{2.18}$$

---

* The subsonic case appears to be amenable to analysis but requires a matching of two separate solutions along the sonic line $x = 0$.

where p is the Laplace transform parameter and $\mu(c_0 p)$ has the nature of an operational shear modulus. With suitable definitions these reduce to the following ordinary differential equations inasmuch as the parameter p will be treated as a constant until final inversion:

$$\frac{d^2\overline{\phi}}{dy^2} - m_\phi^2 p^2 \overline{\phi} = 0 \tag{2.19}$$

$$\frac{d^2\overline{\psi}}{dy^2} - m_\psi^2 p^2 \overline{\psi} = 0 \tag{2.20}$$

where

$$\begin{aligned} m_\phi &= \sqrt{M_\phi^2 - 1} \equiv \sqrt{(c_0/c_\phi)^2 - 1} \\ m_\psi &= \sqrt{M_\psi^2 - 1} \equiv \sqrt{(c_0/c_\psi)^2 - 1} \\ c_\phi &= \sqrt{\frac{K + \frac{4}{3}\mu(c_0 p)}{\rho}} = \text{"operational" dilatation wave speed} \\ c_\psi &= \sqrt{\frac{\mu(c_0 p)}{\rho}} = \text{"operational" shear wave speed} \end{aligned} \tag{2.21}$$

The transformed boundary conditions become

$$\overline{\sigma}_{yy}(p, 0) = -\frac{1}{p} \tag{2.22}$$

$$\overline{\sigma}_{xy}(p, 0) = 0 \tag{2.23}$$

The usual tensor notation will be employed so that the strain-displacement relation in the moving coordinate system is

$$\epsilon_{ij} = \frac{1}{2}(u_{i,j} + u_{j,i}) \tag{2.24}$$

and the cubical dilatation is

$$\epsilon_{ii} = u_{i,i} = -\phi_{xx} - \phi_{yy} = -\nabla^2\phi \tag{2.25}$$

where the repeated index indicates summation.

2.2 Stress-Strain Relations

The material has been assumed to be elastic in bulk; hence the operator in this case is the constant bulk modulus K. Therefore, using 2.25,

$$\sigma_{ii} = 3K\,\epsilon_{ii} = -3K\nabla^2\phi \ . \tag{2.26}$$

In shear the viscoelastic relation is written in terms of stress and strain deviators; hence in the original x', y', t' coordinates, it is

$$\sigma_{ij} - \frac{1}{3}\,\sigma_{kk}\,\delta_{ij} = 2\mu\left[\epsilon_{ij} - \frac{1}{3}\,\epsilon_{kk}\,\delta_{ij}\right] \tag{2.27}$$

where μ is the differential operator. Applying the steady state transformation along with 2.26 and finally the Laplace transformation in x, we have

$$\overline{\sigma}_{ij}(p,y) = K\,\delta_{ij}\,\overline{\epsilon}_{kk}(p,y) - 2\mu(c_0 p)\left[\frac{\overline{\epsilon}_{kk}(p,y)}{3}\,\delta_{ij} - \overline{\epsilon}_{ij}(p,y)\right] \ . \tag{2.28}$$

The form of the displacement-potential relations 2.7 and 2.8 goes over unchanged into the steady state coordinates. Upon differentiating and Laplace transforming, we have the following set of necessary relations for the two-dimensional situation:

$$\overline{\frac{\partial u}{\partial x}} = -p^2 \bar{\phi} + p \frac{\partial \bar{\psi}}{\partial y} , \qquad \overline{\frac{\partial u}{\partial y}} = -p \frac{\partial \bar{\phi}}{\partial y} + \frac{\partial^2 \bar{\psi}}{\partial y^2} \tag{2.29}$$

$$\overline{\frac{\partial v}{\partial x}} = -p \frac{\partial \bar{\phi}}{\partial y} - p^2 \bar{\psi} , \qquad \overline{\frac{\partial v}{\partial y}} = - \frac{\partial^2 \bar{\phi}}{\partial y^2} - p \frac{\partial \bar{\psi}}{\partial y} . \tag{2.30}$$

Combining these with transformed strain-displacement relations from 2.24 and 2.25 gives the strain components

$$\begin{aligned}
\bar{\epsilon}_{xx} &= -p^2 \bar{\phi} + p \frac{\partial \bar{\psi}}{\partial y} \\
\bar{\epsilon}_{yy} &= - \frac{\partial^2 \bar{\phi}}{\partial y^2} - p \frac{\partial \bar{\psi}}{\partial y} \\
\bar{\epsilon}_{xy} &= \frac{1}{2} \left[-2p \frac{\partial \bar{\phi}}{\partial y} + \frac{\partial^2 \bar{\psi}}{\partial y^2} - p^2 \bar{\psi} \right] \\
\bar{\epsilon}_{kk} &= -p^2 \bar{\phi} - \frac{\partial^2 \bar{\phi}}{\partial y^2} .
\end{aligned} \tag{2.31}$$

Hence the transformed stress components from 2.28 and 2.31 are

$$\begin{aligned}
\bar{\sigma}_{xx}(p,y) &= -(K - \tfrac{2}{3}\mu) \left(p^2 \bar{\phi} + \frac{\partial^2 \bar{\phi}}{\partial y^2}\right) + 2\mu \left(p \frac{\partial \bar{\psi}}{\partial y} - p^2 \bar{\phi}\right) \\
\bar{\sigma}_{yy}(p,y) &= - (K - \tfrac{2}{3}\mu)\left(p^2 \bar{\phi} + \frac{\partial^2 \bar{\phi}}{\partial y^2}\right) - 2\mu \left(\frac{\partial^2 \bar{\phi}}{\partial y^2} + p \frac{\partial \bar{\psi}}{\partial y}\right) \\
\bar{\sigma}_{xy}(p,y) &= \mu \left(\frac{\partial^2 \bar{\psi}}{\partial y^2} - 2p \frac{\partial \bar{\phi}}{\partial y} - p^2 \bar{\psi}\right) .
\end{aligned} \tag{2.32}$$

Incorporating 2.32 with 2.19-2.21 in the boundary conditions 2.22 and 2.23 for y = 0 yields

$$-\bar{\sigma}_{yy}(p,0)=(K-\tfrac{2}{3}\mu)p^2M_\phi^2\bar{\phi}\,(p,0)+2\mu\,[p^2m_\phi^2\bar{\phi}(p,0)+p\,\frac{\partial\bar{\psi}(p,0)}{\partial y}] \qquad (2.33)$$

$$\frac{\bar{\sigma}_{xy}(p,0)}{p\mu} = p\,(m_\psi^2 - 1)\,\bar{\psi}(p,0) - 2\,\frac{\partial\bar{\phi}(p,0)}{\partial y} = 0\,. \qquad (2.34)$$

These boundary conditions will evaluate the arbitrary constants arising from the solutions of 2.19 and 2.20 which are of the form

$$\bar{\phi}(p,y) = A_1(p)\,e^{pm_\phi y} + A_2(p)\,e^{-pm_\phi y} \qquad (2.35)$$

$$\bar{\psi}(p,y) = B_1(p)\,e^{pm_\psi y} + B_2(p)\,e^{-pm_\psi y}\,. \qquad (2.36)$$

The constants A_1 and B_1 are immediately set equal to zero by the requirement that the waves are diverging. Upon inserting 2.35 and 2.36 in 2.33 and 2.34 to obtain the coefficients A_2 and B_2, the final transformed solutions become

$$\bar{\phi}(p,y) = \frac{m_\psi^2 - 1}{\mu p^3[(m_\psi^2-1)+ 4m_\phi m_\psi]}\,e^{-pm_\phi y} \qquad (2.37)$$

$$\bar{\psi}(p,y) = -\frac{2m_\phi}{\mu p^3[(m_\psi^2-1)+ 4m_\phi m_\psi]}\,e^{-pm_\psi y}\,. \qquad (2.38)$$

2.3 Laplace Transform Inversion

In terms of the usual inversion integral, the steady-state solution for ϕ appears as

$$\phi(x,y) = \frac{1}{2\pi i}\int_{\gamma-i\infty}^{\gamma+i\infty}\bar{\phi}\,(p,y)\,e^{px}\,dp\,. \qquad (2.39)$$

However, since μ, m_ϕ, and m_ψ are in general complicated functions of p, the ordinary inversion process is not feasible and the even greater advantages of the collocation procedure described in Part I are imminently apparent, inasmuch as it can be readily applied in turn to all three stress components arising from each wave, shear and dilatation.

The exponential part of 2.39 is

$$e^{-pm_\phi y + px} = e^{p(x - m_\phi y)} \tag{2.40}$$

To modify this for convenience in the inversion process, let

$$\bar{x}_\phi = x - m_{\phi_g} y \tag{2.41}$$

where $\bar{x}_\phi$ is the horizontal distance behind the dilatation glassy wave front in the material and m_{ϕ_g} is the glassy modulus value of m_ϕ. Noting that all the material-dependent factors in 2.37 and 2.38 have been written as functions of $c_0 p$, we redefine the Laplace transform variable as

$$q = c_0 p \ . \tag{2.42}$$

Making all necessary modifications to incorporate 2.41 and 2.42, the representation for the dilatation wave takes the form

$$\phi(\bar{x}_\phi, y) = \frac{1}{2\pi i} \int_{\gamma - i\infty}^{\gamma + i\infty} \frac{c_0^2 (m_\psi^2 - 1) e^{-q \frac{y}{c_0}(m_\phi - m_{\phi_g})}}{\mu q^3 [(m_\psi^2 - 1)^2 + 4 m_\phi m_\psi]} e^{\frac{q\bar{x}_\phi}{c_0}} \, dq \tag{2.43}$$

so that

$$\bar{\phi}(q,y) = \frac{c_0^2 (m_\psi^2 - 1)}{q^3 \mu [(m_\psi^2-1)^2 + 4m_\phi m_\psi]} e^{-\frac{qy}{c_0}(m_\phi - m_{\phi_g})} . \qquad (2.44)$$

A similar definition for the shear wave, which arrives at a given point some time later than the dilatation wave, is

$$\bar{x}_\psi = x - m_{\psi_g} y . \qquad (2.45)$$

This gives the following transformed solution for the shear wave:

$$\bar{\psi}(q,y) = \frac{-2c_0 m_\phi}{q^3 \mu [(m_\psi^2-1)^2 + 4m_\phi m_\psi]} e^{-\frac{qy}{c_0}(m_\psi - m_{\psi_g})} \qquad (2.46)$$

where the inverted solution will be $\psi(\bar{x}_\psi, y)$.

Since dilatation and shear waves do arrive at different times, the stress components σ_{xx}, σ_{yy}, σ_{xy} must be computed separately for the two wave contributions and then combined in the final time solution. For example, from 2.32 and 2.44, the transformed stress $\bar{\sigma}_{yy}$ due to the dilatation wave becomes

$$[\bar{\sigma}_{yy}(q,y)]_\phi = -\frac{1}{q} \frac{(m_\psi^2 - 1)^2}{(m_\psi^2-1)^2 + 4m_\phi m_\psi} e^{-\frac{qy}{c_0}(m_\phi - m_{\phi_g})} . \qquad (2.47)$$

For abbreviation, we define

$$
\begin{aligned}
R(q) &= (m_\psi^2 - 1)^2 + 4\, m_\phi m_\psi \\
T(q) &= m_\psi^2 - 1 \\
U_\phi(q) &= m_\phi - m_{\phi_g} \\
U_\psi(q) &= m_\psi - m_{\psi_g} \\
V(q) &= qy/c_0 \\
W(q) &= m_\psi^2 + 1 - 2m_\phi^2 \ .
\end{aligned}
\tag{2.48}
$$

Hence the q-multiplied transforms of the stresses are

$$
\begin{aligned}
q\,\bar{\sigma}_{yy_\phi} &= -\frac{T^2}{R}\, e^{-VU_\phi} \\
q\,\bar{\sigma}_{yy_\psi} &= -\frac{4m_\phi m_\psi}{R}\, e^{-VU_\psi} \\
q\,\bar{\sigma}_{xx_\phi} &= -\frac{WT}{R}\, e^{-VU_\phi} \\
q\,\bar{\sigma}_{xx_\psi} &= -\,(q\,\bar{\sigma}_{yy_\psi}) \\
q\,\bar{\sigma}_{xy_\phi} &= \frac{2m_\phi T}{R}\, e^{-VU_\phi} \\
q\,\bar{\sigma}_{xy_\psi} &= -\frac{2m_\phi T}{R}\, e^{-VU_\psi} \ .
\end{aligned}
\tag{2.49}
$$

The Laplace transform inversion for each stress component can now be carried out by a collocation procedure essentially similar to that in Part I for the one-dimensional problem. Thus the series coefficients S_ℓ are evaluated from the relations

$$\sum_{\ell=1}^{n} \frac{S_\ell}{1+\frac{\gamma_m}{\gamma_\ell}} = [q\,\bar{\sigma}_{ij}(q)]_{q=\frac{1}{\gamma_m}} - [q\,\bar{\sigma}_{ij}(q)]_{q=0}$$

$$= [q\Delta\bar{\sigma}_{ij}(q)]_{q=\frac{1}{\gamma_m}} \tag{2.50}$$

and the stress component is given by

$$\sigma_{ij}(\bar{x}, y) = S_0 + \sum_{\ell=1}^{n} S_\ell \, e^{-\frac{\tau_{\bar{x}}}{\gamma_\ell}} \tag{2.51}$$

where $\tau_{\bar{x}} = \bar{x}/c_0$ is the physical time after the glassy wave has passed the point in question and the stress far behind the wave front is given by the final value theorem

$$S_0 = \lim_{q\to 0} [q\,\bar{\sigma}(q)] \, . \tag{2.52}$$

As would agree with the static elasticity analysis, the long-time stress state is one of uniform hydrostatic compression in the half-space.

The solution has been programmed for the IBM 7090 computer and carried out using the same viscoelastic properties of the polyurethane material represented by 1.29 in Part I, where the operational shear modulus $\mu(q)$ (or $G(q)$ in engineering nomenclature) is the reciprocal of the operational shear compliance $J(q)$. Based on experimental data (30), the bulk modulus used was $K = 2.07 \times 10^{10}$ dynes/cm^2. The resulting glassy dilatation wave speed was 1.778×10^5 cm/sec,

while the corresponding rubbery value was 1.385×10^5 cm/sec. For the shear wave, the glassy speed was 0.963×10^5 cm/sec and the rubbery speed was 3.68×10^3 cm/sec. Judging from the results obtained in the one-dimensional problem, a 15-term series representation for 2.51 was chosen and proved quite adequate. The collocation process in each case covered five decades of logarithmic response time with quarter-decade spacing in areas of rapid change. The IBM program output incorporated a paper-plot of the series $\Sigma \frac{S_\ell}{1 + \gamma_m/\gamma_\ell}$ compared with the actual values of $q\Delta\bar{\sigma}(q)$ as a function of log q to monitor the accuracy of the series representation and thus insure the validity of each inversion process. The main point of practical concern was the choice of the center of the collocation regime for the various conditions of Mach number of the loading wave and depth in the material. The value of q corresponding to the rubbery wave arrival time again was satisfactory.

The stress histories were obtained for Mach numbers (M_ϕ) of 1.01, 1.10, 1.50, 2.00 and for depths (y) of 0.1, 1, 4, 9, and 15 cm. To illustrate the character of the solution, typical response curves for the various components are shown in fig. 7 for the case where $M_\phi = 1.5$, y = 4 cm. The first notable feature is that both shear stress components, σ_{xy_ϕ} and σ_{xy_ψ}, are of essentially negligible magnitude, as are the other components from the shear wave, $\sigma_{xx_\psi} = -\sigma_{yy_\psi}$. This probably results from the purely compressive nature of the loading which predominantly excites the dilatation wave and normal stresses. The latter, σ_{xx_ϕ} and σ_{yy_ϕ}, differ by less than 2% throughout the response history and are adequately shown by

one curve; hence the stress state resembles one of continually increasing hydrostatic compression. The long time behavior of course reflects this state of equal normal stresses in all directions after the transient effects have ceased. The above considerations indicate that the stress sums from both waves at any place in the material can be approximated by the dilatation wave components.

The actual total stresses are shown in figs. 8a to 8d for the four different Mach numbers. The early dispersive features prior to the sharp stress rise in each case have been suppressed to show more clearly the major portion of the viscoelastic response.* Once again the importance of the rubbery arrival time relative to the stress rise is evident; the obvious engineering approximation to stress wave problems can be made that the viscoelastic response straddles this particular parameter for a step loading.

It is of interest in connection with the ground shock problem mentioned previously to investigate the conditions at the wave front as it passes through the material. We have noted that $\sigma_1 \doteq \sigma_2$; hence the Mohr's circle representation of the two-dimensional stress state is a point and in general there is no shear in the stress field. The only modification to this condition occurs at the time of the first significant stress arrival which is associated with a rapid rise in

* The computed solutions indicate a maximum tensile stress in this dispersive region of the order of 10% of the applied boundary stress. The dispersive amplitude showed no increase beyond a depth of 9 cm in the material for any of the Mach numbers investigated, tending to corroborate the statement in Section 1.4 regarding a limit on the ultimate magnitude of the viscoelastic dispersive oscillations in a rod.

the normal stress. Immediately after the value of x for which σ_{xx} and σ_{yy} start to increase in fig. 8, there appears a short transient shear stress pulse of small magnitude originating at the head of the moving pressure pulse as it passes over the surface of the half-space.

For all supersonic Mach numbers this shear stress has a rapid increase to approximately $\sigma_{xy}/p_0 = 0.05$ in the immediate vicinity of the surface of the half-space ($y \doteq 0.1$ cm). However, it quickly decays to essentially zero magnitude after a distance of 1 cm behind the wave front. With increasing depth, the strength as well as the sharpness of this pulse decreases exponentially; by y = 9 cm, the entire shear signal is negligible.

The resultant normal stress on an arbitrary plane in a two-dimensional stress field is given by

$$\sigma_n = \sigma_x \cos^2\theta + \sigma_y \sin^2\theta \pm \sigma_{xy} \sin 2\theta \qquad (2.53)$$

where θ is the angle that the normal to the plane makes with the x-axis. In the present case, $\sigma_{xx} \doteq \sigma_{yy}$ and $\sigma_{xy} \doteq 0.05\ p_0$; thus if one considers the problem of a structure buried in the viscoelastic material and impacted by the stress pulse caused by a blast wave moving over the surface of the half-space, an estimate for the maximum normal stress from 2.53 is

$$\sigma_{n_{max}} = \sigma_{yy} + 0.05\ p_0 .$$

Since σ_{yy} can reach approximately $1.07\ p_0$ (figs. 8a to 8d), the design values of applied stresses for the situation treated here are

$$\sigma_{n_{max}} \doteq 1.07\ p_0 + 0.05\ p_0 = 1.12\ p_0$$

$$\sigma_{ns_{max}} \doteq 0.05\ p_0 \ . \tag{2.54}$$

The comparable elastic solution for this geometry for the supersonic line load (25) indicates that stress occurs only at the wave fronts. It is an immediate extension of this solution to the moving step load (18) in which the response is a step stress increase at the dilatation and shear wave fronts and the major contribution is found to arise from the dilatation wave. Hence in comparison with the data of figs. 8a to 8d, each stress rise curve in the elastic case would appear as a wave-front step increase to the ultimate response $\sigma_{ij} = p_0$. To indicate the modification to the sharp stress rise which occurs when the material is viscoelastic, it is convenient to consider the distance (and hence time) between the first significant stress arrival (denoted x_{σ_0}) and the point at which it has increased to the applied pressure (denoted $x_{\sigma_{p_0}}$). Representing this distance by

$$\Delta x = x_{\sigma_{p_0}} - x_{\sigma_0} \tag{2.55}$$

the corresponding stress rise time Δt is given by

$$\Delta t = \frac{\Delta x}{c_0} \ . \tag{2.56}$$

Since Δx is related to the depth in the material, the data of figs. 8a to 8d show that Δt is directly proportional to y for the polyurethane material. The variation of $\Delta t/y$ with Mach number is shown in fig. 9.

Thus from an engineering point of view the effect of viscoelasticity on the magnitude and sharpness of application of the stress pulse can be determined. For the moving step pressure loading, the normal stresses are slightly higher than in the elastic situation, but the sharpness of the stress rise at any depth of the material is alleviated, varying from the step at the surface to $\Delta t \doteq 5.2 \times 10^{-5}$ sec at y = 15 cm for $M_\phi = 1.01$. It appears feasible to correlate the rise time with mechanical properties for other viscoelastic materials such that a rise-time function might be constructed in the form

$$\Delta t = \Delta t \text{ (y; viscoelastic parameter)}$$

where the viscoelastic parameter would probably involve the slope of the compliance (or modulus) transition curve at the inflection point and the ratio of glassy to rubbery compliance.

B. SEMI-INFINITE THIN PLATE

The corresponding problem in plane stress, in which it is assumed that a semi-infinite plate represented by $y \geqslant 0$ (fig. 6) is sufficiently thin that the $\sigma_{zz} = 0$ boundary condition applies throughout the thickness of the plate, is in general not a direct analog of the plane strain situation. The geometric surface effects can introduce dispersion of the waves not encountered in the infinite medium.

The problem of the basic mode of longitudinal wave propagation in an infinite elastic plate has been solved by Lamb (31). Mindlin (32), Holden (33) and other investigators have considered the higher modes of transmission as well as the dispersive character

and approximate solutions associated with this geometry. But as in the one-dimensional case, a solution emphasizing the viscoelastic effects will be sought.

The conversion of static elastic problems from plane strain to plane stress by modifying the effective values of the elastic constants is well known (34). Less attention has been given to dynamic situations but Bishop (35) has shown the applicability of the approach to certain cases. One of these involves symmetrical waves in a thin plate. The conditions under which it will be applied to viscoelastic material are essentially the same as indicated in Part I for the uniaxial case. The short wave-length components of a step input are again found to be quickly damped and hence geometric dispersion in the thin plate is neglected so that the viscoelastic behavior clearly appears.

Since there are no normal stress components on planes perpendicular to the wave front in the case of shear waves, the effective shear modulus in plane stress is identical to that for plane strain. Dilatation however involves normal stresses in directions perpendicular to the wave front and hence the presence of boundaries allows for lateral motion of the material. Hence the effective modulus in bulk for plane stress will differ from that for plane strain. Thus in modifying the semi-infinite half space solution to one applicable to the thin plate the material properties must obey the following conversion:

$$\begin{aligned} \mu &\rightarrow \mu \\ K &\rightarrow K\left(\frac{1-4\nu^2}{1-\nu^2}\right) . \end{aligned} \tag{2.57}$$

Since the bulk properties have been considered to be elastic at the rubbery values and μ_R is available from fig. 3, the value of ν to be used in the conversion is available from the elasticity relation

$$K = \frac{2\mu}{3} \left(\frac{1+\nu}{1-2\nu}\right) \quad . \tag{2.58}$$

Indicating the nearly incompressible nature of the polyurethane material in the rubbery state, $\nu_R = 0.4996$. Thus the effective bulk modulus in the plane stress analysis is

$$K_{Eff.} = 0.003905 \times 10^{10} \frac{\text{dynes}}{\text{cm}^2} \quad .$$

The corresponding thin plate wave speeds are 7380 cm/sec for the rubbery state and 111,300 cm/sec for the glassy state. The shear wave speeds are the same as for the plane strain case.

The computer solution has been carried out for the same supersonic Mach numbers relative to the glassy dilatation (thin plate) wave speed and depths in the material as for the plane strain analysis.

Histories of the normal stress components σ_{yy} and σ_{xx} associated with the propagating waves are shown in figs. 10a to 10d. Again the dispersive effect prior to the major stress increase is limited to approximately 7% of the applied boundary stress. It typically appears as shown in fig. 10a, but for increased clarity, this portion is not shown in the other three graphs. The σ_{xy} shear stress, which never exceeds a magnitude of $0.04\ p_0$ and is usually much less, is also omitted; it should be noted however that this condition is in general the result of a mutual cancellation of the dilatation and shear wave contributions, each of which though small

has a finite magnitude.

As expected from the results for the geometries considered previously, the rubbery dilatation arrival position is centrally located with respect to the major portion of the stress rise. Noteworthy is the much greater extension of the viscoelastic response in the x-direction compared with the case of plane strain. The long-time behavior does however approach the static plane stress solution values of $\sigma_{yy} = p_0$ and $\sigma_{xx} = \nu\sigma_{yy} \doteq 0.5\ \sigma_{yy}$ (assuming the material to be incompressible in its rubbery behavior).

The rather definite relationships with depth in the material of the stress levels associated with the dilatation and shear wave rubbery arrival times (x_{ϕ_R} and x_{ψ_R}) are indicated in figs. 10a-d and illustrated for all Mach numbers treated in fig. 11 along with the maximum tensile stresses developed. The tensile σ_{yy} with a maximum value of approximately $0.07\ p_0$ arises from the dispersive nature of the material; the tensile stresses in the x-direction which according to the solution attain a momentary peak of $\sigma_{xx}/p_0 = 0.28$ at $y = 0.1$ cm near the head of the stress pulse are apparently associated in addition with the inertia effects in the neighborhood of the load application point. The magnitude of this transient tensile pulse decays rapidly with depth while the dispersive contribution to σ_{xx} increases to an ultimate amplitude of approximately $0.02\ p_0$.

Corresponding to the location of the above maximum σ_{xx} value, the σ_{yy} stress has risen to $0.95\ p_0$ so that the maximum shear stress experienced by the material near the surface is $\sigma_{ns_{max}} = 0.62\ p_0$. The magnitude of the maximum shear stress

drops off rapidly with x and ultimately approaches the static value of $0.25\ p_0$. Figs. 10a-d reveal that the first significant stress arrival at the start of the major part of the stress rise travels at approximately 1.4×10^4 cm/sec, or an order of magnitude slower than in the case of plane strain. The rise time Δt for σ_{yy} to attain the applied stress p_0 is correspondingly much longer; since σ_{yy} asymptotically approaches p_0, the rise time is approximated as

$$\frac{\Delta t}{y} = \frac{(x)_{\sigma=0.9\,p_0} - (x)_{\sigma=0}}{0.9\,y\,c_0} \doteq 1.3 \times 10^{-4} \quad \text{sec/cm}$$

which remarkably is roughly independent of Mach number for all the cases considered.

These two facts point to an important extension of the solution. For since the first significant energy arrival travels at 1.4×10^4 cm/sec, much slower than the characteristic glassy wave speeds in the material, the results should give an indication of the wave propagation characteristics if the moving pressure pulse is traveling as slow as this, or

$$M_\phi = \frac{c_{\sigma=0}}{c_{\phi_G}} = \frac{1.4 \times 10^4 \text{ cm/sec}}{1.113 \times 10^5 \text{ cm/sec}} = 0.126,$$

i.e., in the subsonic regime relative to c_{ϕ_G}. Thus the significant bonus to the foregoing supersonic solution is evident if we crossplot the previous results as a function of Mach number in the form typically illustrated in fig. 12 for y = 9. The linearity of the stress variation is evident and the drastic extension into the subsonic

regime is possible because of the predominance of the shear modulus relative to the bulk modulus (as modified for plane stress) in determining the plate wave speed, a condition which gives a wide spread between rubbery and glassy plate wave speeds*.

While in the nature of an extrapolation since the method of solution is limited to the supersonic case, it is nevertheless valid since the effect of the step loading is independent of its speed relative to the characteristic material wave speeds. Thus the need to construct a subsonic solution for the broad-band viscoelastic materials is largely eliminated, or conversely it appears a posteriori that the present type of solution can be adapted to lower values of c_0.

The importance of this extension in the present analysis lies in the fact that comparison of photoelastic results in Part IV requires the stress solution in the thin plate for a passing surface wave traveling at a subsonic Mach number, $M_\phi = 0.605$. With the difference in principal stress obtained by straightforward calculations from the data of figs. 10a-d plotted in the manner illustrated in fig. 12 and correlated as a function of time, the necessary viscoelastic optical characterization is applied in Part III to predict the fringe pattern in the semi-infinite plate geometry.

Hence the two-dimensional plane stress solution not only illustrates the viscoelastic wave propagation behavior expected in a thin plate but also provides the information necessary to complete one phase of the analysis of dynamic photoviscoelasticity to be considered in the remainder of the thesis.

---

* The plane strain solution can also be extended to the subsonic case, but here the advantage is slight as the approach is valid only to $M_\phi \doteq 0.85$.

PART III

DYNAMIC BIREFRINGENCE IN VISCOELASTIC MATERIAL

The investigation of dynamic phenomena using photoelastic techniques has shown great progress over the past quarter century with the development of high speed cameras and associated apparatus to record wave propagation. In recent years increasing attention has been given to the use of birefringent polymeric materials for this purpose. Photoviscoelastic analysis however requires techniques not normally encountered when using elastic materials because the optical properties as well as the mechanical behavior of viscoelastic media are time and temperature dependent.

Among the earliest to apply low modulus viscoelastic materials to wave propagation studies was Durelli (36), who for the most part employed relatively low loading rates which did not activate the full spectrum of time-dependent behavior. Other tests (37) have used explosive and other high rate loading devices. Nevertheless, no comprehensive attempt by experimentalists to take the time-dependent behavior into account, especially in dynamic investigations, has been evident until very recently (current investigators include Theocaris (38, 39), Williams et al. (40), Dill (41)). Indeed, the present research was stimulated by an exploratory photoelastic test program (42) simulating the dynamic stresses due to ground shock loading (Part IV).

A. GENERAL PHOTOVISCOELASTIC CONSIDERATIONS

The problem of handling photoviscoelastic data in the most general case involves not only the time variation of optical and

mechanical parameters but also the consequent possibility of non-alignment of the axes of polarization, principal stress, and principal strain. Mindlin (43) laid the groundwork with a basic mathematical treatment, even though much of his analysis was directed toward establishing the conditions under which a viscoelastic model would represent the stresses in an elastic prototype. The special conditions of incompressible material (both elastic and viscoelastic) and proportional loading (no time variation in the distribution pattern of the load, but only a magnitude change with time) were sufficient to guarantee this effect as well as alignment of polarizing and principal axes. When considering solely the viscoelastic stresses, however, these conditions prove to be too restrictive. Read (44) has generalized the viscoelastic analysis to include compressible media and has demonstrated that, as in photoelasticity, the optical measurements give the directions and difference in magnitude of the principal stresses in the plane of the optical wave front, provided the stress-optical relations can be expressed in the same form as we have used earlier for the stress-strain relations. Read points out that his formulation places no restriction on the boundary conditions.

No attempt will be made here to treat the general question of photoviscoelastic relations* since the main objective of Part III is to indicate the treatment necessary to include appropriate optical characterization of viscoelastic materials for photoelastic work.

---

* Reference 40 includes some current efforts in this direction.

It should be noted, however, that dynamic situations frequently involve moving loads so that the formulation proposed by Read is advantageous. Even though in the general dynamic case principal stress axes are not necessarily aligned with the polarizing axes, Read handles the problem by referring all quantities to some arbitrary fixed set of x-y axes and showing that the birefringence can be related to the stress difference $\sigma_x - \sigma_y$. In the type of situation depicted in the theoretical studies of Parts I and II, in which the entire response spectrum is activated, the glassy and rubbery states correspond to elastic conditions, so that optical and mechanical principal axes are known to be aligned at the start and finish of the wave propagation process. Hence axis non-alignment will occur only during the photoviscoelastic transition period which can well be a relatively brief part of the time of observation. An additional engineering aspect relative to this question is that most high polymers are essentially incompressible except in the glassy region; as noted in Part I, the corresponding high frequency components are quickly attenuated for step function inputs, thus making much of the incompressible treatment of Mindlin applicable for a large portion of the time history in many cases.

Consequently, a reasonable engineering approximation might be made that the optical and mechanical axes are aligned, subject to later experimental verification. As to the other prime photoviscoelastic consideration, there is ample theoretical and experimental evidence (38, 43, 44, 45) to guarantee that the linear differential operator relation of birefringence to stress (or strain) is valid for polymers; this will be further verified in the subsequent work of Part III.

From the viewpoint of test procedure, it may be noted that a calibration of viscoelastic material properties can be made by quasi-static means for use in dynamic problems provided the appropriate range of the time parameter is suitably accounted for.

B. CHARACTERIZATION OF PHOTOVISCOELASTIC MATERIALS

To utilize viscoelastic materials in dynamic photoelastic stress analysis, the time dependencies of both the optical response characteristics and the recorded fringe order must be taken into account. Especially in wave propagation situations, extremely short time behavior is of importance. Hence special attention must be given to the evaluation of material response properties over the complete time spectrum including this short time region in order to apply the photoelastic technique.

The present research is directed toward providing a sound quantitative basis for using linear viscoelastic materials in dynamic photoelastic testing. For the complete analysis of a two-dimensional stress field, the question discussed above regarding time-dependent optical axis orientation and the determination of the necessary third piece of information (such as thickness change) must be considered; however, the crucial initial concern is to establish a quantitatively valid method to account for the time-dependent mechanical and birefringent properties characterizing viscoelastic materials. It can be pointed out immediately that for material calibration, the problem is drastically simplified since a uniaxial test specimen can be used; in this case all axes are known to be aligned providing the

specimen was initially unstressed. Thus the treatment proposed here is precisely applicable.

The verification of such a procedure will consist in comparing theoretically predicted time-dependent fringe patterns with experimental results for comparable geometry and loading. The analytical portion of the study involves three basic phases: (1) theoretical solution for stresses due to wave propagation (available from Parts I and II); (2) characterization of the appropriate time-dependent optical properties of the viscoelastic material used (to follow immediately); (3) prediction of fringes by means of superposition integrals involving the results of the first two phases (in Section C below).

3.1 Test Apparatus and Procedure

The material chosen for the test program was Hysol 8705*, a low modulus polyurethane material which has been used with some success in previous tests involving low loading rates. A single tensile specimen (fig. 13), machined from a sheet of 1/2 inch thick material, was used for all the calibration tests. While repeated loading effects in some types of viscoelastic tests (e.g., vibration) can be serious, the calibration procedure employed here proved to be satisfactory because of the long-time elastic behavior of Hysol 8705 and the allowance of adequate time for the substantially complete relaxation of the specimen between runs.

* Available from the Hysol Corporation, Olean, New York.

Tensile tests in creep or relaxation (39) could be carried out to obtain the desired optical and mechanical properties, but a method found extremely convenient was the use of an Instron Model TT-C constant-strain-rate test machine. It incorporated a Missimers temperature control chamber and a G.E. AH-4 mercury vapor light source in conjunction with a green (5460Å) filter, polaroid sheets and quarter-wave plates to create a circular polariscope within the test machine as suggested originally by Keedy, et al. (46). The experimental arrangement is shown schematically in fig. 14, where it may be noted that the polarizing units are placed within the thermal chamber in order to eliminate any effect upon the birefringence due to thermal stress in the window glass. Isothermal tests were performed for a range of temperatures from -40°C to +18°C and extension rates of 0.02 in/min to 2 in/min. The ease of control and short running time for each test by this method are distinct advantages.

Observation of the change of fringe order with load and elongation (which were recorded on a time base on the Instron chart) was made by eye in this calibration study which was designed as somewhat of a pilot run prior to more exhaustive investigation using a photocell (cf. reference 40). Nevertheless, it proved possible to obtain nearly the complete time-temperature response spectrum, thus enabling the well-known time-temperature shift factor technique to be applied. A typical time history showing the raw mechanical and optical data is shown in fig. 15 where the passing fringes are recorded as pips on the otherwise continuous load vs. elongation

curve.

Owing to the enlarged sections at each end of the test specimen (fig. 13) designed to relieve stress concentrations around the Instron grips, it was found necessary to apply a factor of 0.96 to the total elongation recorded on the Instron chart when computing strain based on the uniform test section length of 3.5 in. Subsequent reduction to coefficient form will utilize true stress incorporating the reduction of cross-sectional area due to Poisson's ratio effect; also the logarithmic strain accounting for the change in test specimen length with increasing strain will be employed. Owing to the small order of magnitude of strain involved (usually less than 8%), these corrections are significant only in the high temperature and low strain rate tests.

Since the Instron machine operates at constant extension rate rather than precisely at a constant strain rate, a correction as a function of specimen length could be made. But as will be pointed out in the next section, the reduced data appear as ratios involving the strain rate in both numerator and denominator; hence the ratio remains constant and no correction need be applied to the magnitudes of the coefficients. But a related error does occur in the determination of the appropriate time in converting test data to an equivalent relaxation process; in this case the strain rate is approximated as constant. Again the effect is measurable only in the rubbery region where however the time dependency of mechanical and optical coefficients is very weak so that no significant error is introduced.

3.2 Determination of Stress Relaxation Modulus

Constant strain rate data for linearly viscoelastic media are most readily reduced to stress relaxation coefficients (19). In the case of mechanical behavior, the stress relaxation modulus, defined as the stress-strain ratio for a step input in strain, ϵ_0, is

$$E_{rel}(t) \equiv \frac{\sigma_{rel}(t)}{\epsilon_0} \tag{3.1}$$

where σ_{rel} is the stress measured as a function of time, t, from the beginning of the relaxation process. Therefore the general transform expression, or transfer function, relating the stress and strain for arbitrary strain input, namely,

$$E(p) = \frac{\bar{\sigma}(p)}{\bar{\epsilon}(p)} \tag{3.2}$$

can be determined conveniently by the relaxation measurement. For this case, because $\epsilon_{rel}(t) = \epsilon_0$,

$$E(p) = \frac{\bar{\sigma}_{rel}(p)}{\bar{\epsilon}_{rel}(p)} = \frac{\bar{\sigma}_{rel}(p)}{\epsilon_0/p} \tag{3.2a}$$

where p is the Laplace transform parameter.

On the other hand one could just as well characterize E(p) by a constant strain rate test, in which $\epsilon_{tens}(t) = Rt$, where R is the uniform strain rate and $\epsilon_{tens}(t)$ is the corresponding tensile strain at time, t. The transfer function in this case would then be

$$E(p) = \frac{\bar{\sigma}_{tens}(p)}{\bar{\epsilon}_{tens}(p)} = \frac{\bar{\sigma}_{tens}(p)}{R/p^2} \tag{3.2b}$$

where σ_{tens} is the tensile stress during the constant strain rate process.

Because the operational modulus E(p) is an invariant of the material, the relaxation and constant strain rate tests must be related. Equating 3.2a and 3.2b gives

$$\bar{\sigma}_{rel}(p) = \epsilon_0 \frac{p\bar{\sigma}_{tens}(p)}{R} \quad . \tag{3.2c}$$

Inversion of 3.2c for quiescent initial conditions gives

$$E_{rel}(t) = \frac{\sigma_{rel}(t)}{\epsilon_0} = \frac{d\sigma_{tens}(t)}{d(Rt)} = \left(\frac{d\sigma_{tens}}{d\epsilon}\right)_{\epsilon = Rt} \tag{3.3}$$

where $\epsilon = Rt$ is the tensile strain during the constant strain rate test.

The statistical theory of rubberlike elasticity indicates that the internal elastic retractive forces in polymeric chains are directly proportional to the absolute (constant) temperature (47). Hence, the test results can be normalized to an arbitrary reference temperature, T_0, if the stress in 3.3 is adjusted by the ratio T_0/T, giving

$$\frac{T_0}{T} E_{rel}(t) = \left\{\frac{d(\sigma T_0/T)}{d\epsilon}\right\}_{\epsilon = Rt} \quad . \tag{3.3a}$$

By introducing R in both numerator and denominator and using logarithmic derivatives, (3.3a) can be written in the equivalent form

$$\frac{T_0}{T} E_{rel}(t) = \left\{ \frac{\sigma T_0/RT}{\epsilon/R} \frac{d[\log(\sigma T_0/RT)]}{d[\log(\epsilon/R)]} \right\}_{t=\epsilon/R} . \quad (3.3b)$$

A value of $T_0 = 291°K$ has been used in order to correlate the various test data reported herein.

Finally, the experimentally-discovered (48, 49) time-temperature shift factor, a_{T_0}, can be included to account for the well-known qualitative similarity of low temperature-low strain rate and high temperature-high strain rate behavior. It results in the following equation in terms of reduced time, defined as $t' = \epsilon/Ra_{T_0}$,* and reduced strain rate Ra_{T_0}:

$$\frac{T_0}{T} E_{rel}(t') = \left\{ \frac{\sigma T_0/Ra_{T_0}T}{\epsilon/Ra_{T_0}} \frac{d[\log(\sigma T_0/Ra_{T_0}T)]}{d[\log(\epsilon/Ra_{T_0})]} \right\}_{t'=\epsilon/Ra_{T_0}} . \quad (3.4)$$

A log $(\sigma T_0/Ra_{T_0}T)$ vs. log t' master plot of the stress-strain test data reduced to $T_0 = 291°K$ is shown in fig. 16 which indicates the rubbery to glassy transition region as the non-linear portion of the curve. While consistent and reproducible, the data shown at the glassy end of the time spectrum are obtained very close to the start-up point of some of the low temperature tests where careful handling of the experimental curves is necessary. Indeed, as the elongations under these conditions are quite small (of the

---

* If the situation is non-isothermal, the reduced time, t', is related to the physical time, t, through the equation

$$t' = \int_0^t \frac{d\tau}{a_T[T(\tau)]} .$$

order of 0.001 in.) when the precision of the Instron recording device (a follower pen on a time-base chart) is considered, the accuracy is less than that obtained in the remainder of the calibration; hence this possible approximation in the glassy response must be borne in mind. It is highly desirable to have an improved coverage of this glassy region; additional data will be forthcoming in the more exhaustive program noted above (40).

Since both $\sigma T_0/RT$ and ϵ/R in 3.3b involve units of time, application of the time-temperature superposition principle (49) requires equal shifts in both coordinates of the preliminary log $(\sigma T_0/RT)$ vs. log (ϵ/R) plots at the different temperatures to provide the continuous fairing of the log-log curve in fig. 16. The amount of shifting required along each axis for the respective test temperatures establishes the relation of log a_T to temperature, fig. 17. Also shown on this plot is the WLF shift factor equation (50)

$$\log a_{T_{WLF}} = \frac{-8.86\ (T-T_s)}{101.8 + (T-T_s)} \qquad (3.5)$$

where the temperature T is in degrees Centigrade and T_s, the reference temperature, was found to be +3°C for the best fit to the experimental data. The test data are reasonably well represented by the WLF equation in the transition region where it is expected to be valid. Since T_s is usually found to be approximately 50°C above the glass transition temperature, we deduce that the value of the latter is

$$T_G = T_s - 50 = -47°C\ . \qquad (3.6)$$

Independent tests (17) of the mechanically similar polyurethane material used in the analysis of Parts I and II gave -40°C as the glassy temperature; thus the foregoing value is seen to be in reasonably good agreement with the expected range of the glassy temperature for Hysol 8705. Note that in 3.5, $\log a_{T_{WLF}}$, which is essentially related to the glassy temperature, is shifted from $\log a_T$ plotted in fig. 17 since the latter corresponds to the arbitrarily selected reference temperature, $T_0 = 291°K$. Fig. 17 also contains data points from the optical calibration to be described in the next section.

The variation with reduced time of E_{rel} as calculated from fig. 17 using 3.4 is shown in fig. 18. Again the broad-band relaxation spectrum for this polyurethane material is evident, along with the fact that a rubbery modulus exists due to the cross-linked nature of the polymer preventing unlimited flow. As it should, the rubbery modulus agrees with static test results on this material (18). Moreover the mechanical response of Hysol 8705 exhibits approximately the same behavior as the polyurethane material tested by Landel (17) and used in the foregoing theoretical wave propagation studies. Comparison of figs. 3 and 18 discloses that the equilibrium and glassy moduli are roughly equal and the logarithmic time (or frequency) transition curves are quite well matched also. This will prove to be an advantage in the comparison of theory to experiment in Part IV.

3.3 Determination of Relaxation Birefringence-Strain Coefficient

As noted in the foregoing, the question of optical calibration needs careful consideration for photoviscoelastic materials. The historical controversy as to whether birefringence is basically a stress or strain activated phenomenon is somewhat academic for essentially elastic media, but for rate-sensitive materials the relationships must be established.

It is appropriate here to reiterate the salient features pertaining to optical characterization of viscoelastic materials. The possibility of lag in the mechanical or optical response to a given loading can in general give rise to a non-alignment of the principal strain axes with the principal stress axes as well as of the optical axis with both of these (43). This does not occur in elastic material since the appropriate coefficients relating stress and strain or either of these with birefringence are not time dependent. However, in the case of isotropic, homogeneous viscoelastic media, in which the coefficients become time operators, special conditions must apply before the alignment of all pertinent axes is assured. Nevertheless, for viscoelastic materials which allow the stress- and strain-optical relations to be expressed by the type of linear operators discussed previously for mechanical properties, the directions of principal stress axes and difference in principal stresses can be determined (44). It requires the measurement of both isochromatics (fringes) and isoclinics (indicating the locus of points having a constant angle of inclination of polarizing axis to

fixed x and y axes) as functions of time. Maximization of the resulting $\sigma_x - \sigma_y$ values with respect to the orientation of the arbitrary x- and y-axes gives the difference in principal stresses and the corresponding directions.

Thus for photoviscoelasticity in general, the time-varying isoclinics become a necessary part of the experimental data to be acquired along with the isochromatics. The practicality or possibility of doing so in dynamic situations will depend on the individual test circumstances. Nevertheless the reduction of data from such a test requires the basic knowledge of the operator relationship between strain and/or stress and birefringence. This is the one item needed to characterize the material, all other pieces of data being dependent on the individual experiment being performed.

To establish this characterization, it is expedient to use a simple test situation eliminating some of the variables. Such a situation we have seen to exist in the case of a uniaxial tensile test starting from rest which guarantees the alignment of optical and mechanical axes; thus the birefringence relationships are simplified and can be formulated directly as functions of the difference in principal strains or stresses.

The theoretical approach to viscoelastic birefringence calibration suggested by Williams (51) and already implied in the work of Mindlin (43) has received preliminary experimental verification (52). As presented herein, it follows the development of Arenz (53).

Photoelastic theory usually takes the form of postulating birefringence-stress and birefringence-strain coefficients relating

fringe order with principal stress and strain difference, respectively; specifically, for the strain dependency, we write

$$n = C_\epsilon (\epsilon_1 - \epsilon_2) \tag{3.7}$$

where

C_ϵ = model birefringence-strain coefficient, fringes/in/in

n = fringe order number.

From the definition given it is apparent that C_ϵ is related to the usual photoelastic material strain-optic coefficient f_ϵ based on maximum shear strain in the following manner:

$$C_\epsilon = \frac{h}{2 f_\epsilon} \tag{3.8}$$

where h = model thickness.

For viscoelastic materials, the association between fringe order and strain is time dependent. In a relaxation test for example, the corresponding birefringence-strain coefficient can be defined as

$$C_{\epsilon_{rel}}(t) = \frac{n_{rel}(t)}{(\epsilon_1 - \epsilon_2)_0} \quad . \tag{3.9}$$

Referring again to a constant-strain-rate uniaxial test for characterization of the material, a derivation essentially similar to that for 3.4 gives the following relation for the relaxation birefringence-strain coefficient:

$$C_{\epsilon_{rel}}(t) = \frac{2}{3}\left(\frac{1}{R}\frac{dn_{tens}}{dt}\right)$$

or

$$C_{\epsilon_{rel}}(t') = \frac{2}{3}\left\{\frac{n/Ra_{T_0}}{\epsilon/Ra_{T_0}}\frac{d[\log(n/Ra_{T_0})]}{d[\log(\epsilon/Ra_{T_0})]}\right\}_{t'=\epsilon/Ra_{T_0}} . \qquad (3.10)$$

In this expression, the material is assumed incompressible ($\nu = 0.5$), and the test is uniaxial so that if $\epsilon \equiv \epsilon_1$ is the axial strain, and ϵ_2 the transverse, then

$$\epsilon_1 - \epsilon_2 = \epsilon_1 - (-\nu\epsilon_1) = \frac{3}{2}\epsilon_1 \qquad (3.11)$$

thus accounting for the factor 2/3 in 3.10. Deviation from the value $\nu = 0.5$ which occurs in the glassy response regime of viscoelastic materials would introduce only minor changes in the magnitude of this factor.

Reduction of test data is similar to the procedure used to determine mechanical property characterization of Section 3.2. The decrease of specimen thickness with elongation was accounted for by multiplying the experimental fringe order by the factor

$$\frac{1}{1-\nu\epsilon} \doteq 1 + \nu\epsilon$$

to obtain n. Again, $\nu = 0.5$ was assumed since the factor is significant only in the higher temperature and lower strain rate regime where the material behaves in a rubbery manner. Thus, the birefringence coefficient is corrected for the effects of thickness change and the initial thickness can be used at any reduced time when

performing additional operations on the characteristic curve.

Values of log(n/R) vs. log (ϵ/R) for each isothermal run were plotted and then shifted according to standard procedure (49) along a 45° reference line, to form the smooth master curve of $\log(n/Ra_{T_0})$ vs. log t', fig. 19. The time-temperature shift factor a_{T_0} thus obtained is plotted on fig. 17. Furthermore, from a comparison of the shift factor for the mechanical data, it is seen that the birefringence shift factor is essentially the same; it is also in good agreement with the WLF equation. The logarithmic master curve of $C_{\epsilon_{rel}}$ vs. t', fig. 20, is obtained from 3.10 using fig. 19. The long time value compares favorably with static determinations of C_ϵ for Hysol 8705 material (36).

3.4 Conversion to Creep Birefringence-Stress Coefficient

An elastic birefringence-stress coefficient is defined in a manner analogous to 3.7 for strain, i.e.,

$$n = C_\sigma (\sigma_1 - \sigma_2) \tag{3.12}$$

where C_σ = model birefringence-stress coefficient, fringes/psi, and C_σ is related to the usual material stress-optic coefficient f_σ by

$$C_\sigma = \frac{h}{2f_\sigma} \quad . \tag{3.13}$$

The viscoelastic creep birefringence-stress coefficient $C_{\sigma_{crp}}(t)$, which is determined during a constant stress test, is not directly obtainable from a constant-strain-rate test. However, it can be obtained from $C_{\epsilon_{rel}}(t)$ for linear viscoelastic materials since interrelationships among the time-dependent functions in 3.7 and

3.12 can be derived.

Suppose the time-dependent shear response is characterized by

$$P(\sigma_1 - \sigma_2) = Q(\epsilon_1 - \epsilon_2) \tag{3.14}$$

where P and Q are linear differential operators as described in Part I. If reduced time is used in 3.14, then the Laplace transforms of 3.7 and 3.12 are related (52). Specifically, from 3.12, one has

$$\begin{aligned} \bar{n}(p) &= C_\sigma(p)\,[\bar{\sigma}_1(p) - \bar{\sigma}_2(p)] \\ &= C_\sigma(p)\,\frac{Q(p)}{P(p)}\,[\bar{\epsilon}_1(p) - \bar{\epsilon}_2(p)] \end{aligned} \tag{3.15}$$

assuming that principal axes are aligned. Similarly, from 3.7 it follows that

$$\bar{n}(p) = C_\epsilon(p)\,[\bar{\epsilon}_1(p) - \bar{\epsilon}_2(p)]\ . \tag{3.16}$$

Hence, upon defining the operational shear modulus (in servomechanism notation, a transfer function) with due regard to the relation of maximum shear stress and strain to principal stress and strain differences, we have

$$2\,G(p) = \frac{Q(p)}{P(p)} \tag{3.17}$$

from which one has immediately that

$$C_\epsilon(p) = 2\,G(p)\,C_\sigma(p)\ . \tag{3.18}$$

Thus the birefringence-stress and -strain coefficients are not independent, but for the case of aligned axes are uniquely related in the

above manner through the time-temperature dependent shear modulus of the linear viscoelastic material.

Application of the Laplace transform to 3.7, 3.12, and 3.14 for conditions of unit step mechanical inputs and introduction of the definition 3.17 lead to the following useful relationships between operational parameters and the transforms of the material properties for the specific processes of stress relaxation and strain creep:

$$G(p) = p\,\overline{G}_{rel}(p) \tag{3.19}$$

$$J(p) = p\,\overline{J}_{crp}(p) \tag{3.20}$$

$$C_{\epsilon}(p) = p\,\overline{C}_{\epsilon_{rel}}(p) \tag{3.21}$$

$$C_{\sigma}(p) = p\,\overline{C}_{\sigma_{crp}}(p) \tag{3.22}$$

where the compliance J is by definition the reciprocal of G.

We are now in a position to solve for $C_{\sigma_{crp}}$. For if 3.19, 3.21, and 3.22 are applied to 3.18, we have

$$\overline{C}_{\epsilon_{rel}}(p) = 2\,p\,\overline{G}_{rel}(p)\,\overline{C}_{\sigma_{crp}}(p)\,. \tag{3.23}$$

Substituting 3.19 and 3.20 in 3.23 gives

$$\overline{C}_{\sigma_{crp}}(p) = \frac{1}{2}\,\overline{C}_{\epsilon_{rel}}(p)\,p\,\overline{J}_{crp}(p)\,. \tag{3.24}$$

Applying the convolution inversion integral to 3.24, we choose the following solution form most convenient for our purpose:

$$C_{\sigma_{crp}}(t) = \frac{1}{2}\left\{J_{crp}(0)\, C_{\epsilon_{rel}}(t) + \int_0^t C_{\epsilon_{rel}}(t-\tau)\, \frac{dJ_{crp}(\tau)}{d\tau}\, d\tau\right\}. \tag{3.25}$$

To utilize this equation, the behavior of $J_{crp}(t)$ is required, and two or three suitable methods to obtain it from $E_{rel}(t)$ are available. The first is a collocation method (54), similar to that used in the theoretical solution for wave propagation in a viscoelastic rod (Part I), in which E_m is the relaxation modulus for a finite-element Weichert model (10) represented analytically by the series

$$E_m(t) = E_R + \sum_{i=1}^{n} E_i\, e^{-t/\tau_i} \tag{3.26}$$

where E_R is the rubbery equilibrium modulus and the τ_i are chosen to span the complete time history of the response; $E_{rel}(t)$ and $E_m(t)$ are then collocated to evaluate the coefficients E_i. This series can be Laplace transformed and the values of $E(p)$ and hence $\overline{D}_{crp}(p) = D(p)/p = 1/pE(p)$ determined. Assuming a similar type of series representation for $D_{crp}(t)$, $\overline{D}_{crp}(p)$ can be inverted by the collocation inversion procedure (14) used in the wave propagation solution to give $D_{crp}(t)$. If again incompressibility is assumed, $J_{crp}(t) = 3D_{crp}(t)$. Thus all the necessary ingredients are available to evaluate 3.25.

A more rapid but slightly less accurate method involves a modified power law representation (19) of $E_{rel}(t)$, which is then converted to an analogous expression for $D_{crp}(t)$ (or $J_{crp}(t)$), with the

fit being accomplished at the inflection point in the curve plotted to a logarithmic scale. Indications are that this latter approach is sufficiently accurate for our purposes. The relaxation data are hence represented by

$$E_{rel}(t) = E_R + \frac{E_G - E_R}{[1 + c \frac{t}{a_{T_0}}]^n} \tag{3.27}$$

where E_G is the glassy (short-time) modulus and c and n are material constants. From fig. 18, c and n are determined from the modulus and its derivative at the inflection point to be $6.64 \times 10^{9.8}$ and 0.513, respectively. A similar approximation to the creep compliance behavior is

$$D_{crp}(t) = D_G + \frac{D_R - D_G}{[1 + \frac{c'}{t/a_{T_0}}]^{n'}} \quad . \tag{3.28}$$

Using the common inflection point and reciprocal slopes at this point for the two functions with D_G and D_R being the reciprocals of E_G and E_R respectively, we obtain the values $c' = 1.11 \times 10^{-5}$ and $n' = 0.513$. Finally, $J_{crp} = 3D_{crp}$ and is given as a function of reduced time in fig. 21 with the normalizing ratio T/T_0 incorporated. Thus its time derivative can be obtained with the result shown in fig. 22, and the integral in 3.25 evaluated to give $(T/T_0)C_{\sigma_{crp}}$ as shown in fig. 23; both operations were carried out numerically. The general accuracy to be expected by the numerical method is indicated by the rubbery value of $C_{\sigma_{crp}}$ which deviated 2% from the directly computed value using long-time elasticity relations between C_σ and C_ϵ. As a limit check, the rubbery magnitude of C_σ agreed closely with the results from static tests of

Hysol 8705 (18, 36).

A third and most simple conversion for $J_{crp}(t)$ is from the approximation

$$D_{crp}(t) \doteq \frac{1}{E_{rel}(t)} \quad . \tag{3.29}$$

Some recent data (39, 55) indicate that for most of the transition region, this is quite well justified experimentally, although it appears that at the "knees" in the relaxation and creep curves, which are fairly critical areas, the error can be appreciable. The strongest argument for the use of 3.29 lies in its providing a method for rapid estimates.

C. DYNAMIC FRINGE PREDICTIONS FOR STRESS WAVE PHENOMENA

The final step before comparing the theoretical analysis with experiment involves the fringe order prediction* based on the Duhamel superposition integral

$$n(t) = \frac{h_{model}}{h_{test}} \left\{ \sigma(0)\, C_{\sigma_{crp}}(t) + \int_0^t C_{\sigma_{crp}}(t-\tau)\, \frac{d\sigma(\tau)}{d\tau}\, d\tau \right\} \tag{3.30}$$

where h_{model} is the thickness of the photoelastic model used in the wave propagation study and h_{test} is the thickness of the material calibration test specimen. If the material is initially undisturbed with no stress applied at a given point in the model until the first

* For purposes of experimental stress analysis, the inverse birefringence operators are required; the determination of these is discussed in Section D below.

finite stress wave arrivals begin to appear, $\sigma(0)$ is zero and only the integral contributes to the fringe pattern.

Since wave propagation in two geometries has been studied analytically (Parts I and II), predicted fringe patterns were determined for both the one-dimensional rod and the two-dimensional thin plate under step input loadings in order to provide a comparison with the experimental findings to be described in Part IV.

The theoretical stress wave solution of fig. 4 incorporated with the optical calibration of Hysol 8705 in equation 3.30 for two positions along the uniaxial rod gave the variation of fringe order with time shown in fig. 24. The appropriate integrations have been carried out numerically in the present analysis, but this operation can readily be performed by computer and assimilated into an overall program with previous steps in the calculations. Also shown in fig. 24 is the experimental fringe pattern from a test on a bar 0.365 in. thick by 0.875 in. wide loaded on the end by a shock wave pressure front. Since comparison of the theoretically predicted and experimental fringe patterns involves an analysis of the test conditions, it is deferred until Part IV which treats the experimental wave propagation aspect of the program.

For the present, we concentrate on a comparison of the predicted dynamic fringe pattern with that given by using the static or long-time equilibrium value of C_σ. In the latter case, the integral disappears from 3.30 and the fringe order is proportional to the stress value, giving the static calibration curve in fig. 24. Apparent first of all is the relatively small difference in the values

of n between the two methods. Examination of the time scale discloses the reason; $C_{\sigma_{crp}}$ is already approaching its rubbery value for times greater than 10^{-5} sec (fig. 23). On the other hand, only a small part of the stress rise in the rod at x = 1.67 cm takes place (at ambient temperature) in the interval from 4.5×10^{-5} to 5.5×10^{-5} sec (fig. 24). Furthermore, farther down the rod (x = 3.81 cm) the difference in n is even less. Hence we conclude that for the step input loading the characteristic optical response time is so short that relatively little delayed photoviscoelasticity occurs over most of the specimen. If however the loading situation produced a much shorter stress rise time, the delayed birefringence would play a significantly larger role during the transient phenomenon.

Several conclusions thus emerge from this theoretical photoviscoelastic treatment alone. For Hysol 8705, the optical response to stress is very rapid compared to many stress rise phenomena, making it a desirable material for wave propagation situations. But the more rapid the stress rise (e.g., very close to the step input), the more influential is the photoviscoelastic behavior during that time period. Moreover, some other viscoelastic materials suggested for photoelastic use (39) have significantly longer relaxation times at room temperature, making the photoviscoelastic analysis even more essential when they are applied to dynamic problems. Finally, a material calibration and analysis of the sort proposed here is useful to evaluate the relative importance of viscoelastic effects in any given situation and hence determine when the calibration is essential and where it might be dispensed

with for engineering applications. For example, for a pulse loading approximating the Dirac δ-function with equal amplitudes for all frequency components, a greater deviation from the rubbery birefringence characteristics is expected since the high frequency components will be stronger than in the case of a step loading.

In the case of the semi-infinite thin plate, the experimental situation again needs discussion since the practical aspects of model size dictate a thickness such that a plane stress situation is not fully realized; these considerations are discussed in Part IV. Hence in this case the comparison with experiment is limited to the shape of the curve depicting variation of fringe order with depth in the material.

Since the plane-stress solution of Part II indicates an approximately constant orientation of principal stress axes (inasmuch as the σ_{xy} shear stresses are practically always ngligible with respect to the normal stresses), we take advantage of this characteristic of "proportional loading" to apply the fringe superposition integral 3.30 directly. The resulting prediction indicates that n_{max}, the maximum number of fringes (occurring at the surface), is approximately equal numerically to 0.4 of the applied overpressure in psi. For comparison purposes, however, the parameter plotted in fig. 25 is n/n_{max} for two values of x, the distance behind the head of the moving step load. The stress rise times are of the order of those pertaining to the one-dimensional case; hence the use of the static birefringence coefficient in calculating fringe

order would produce the same comparison as described just above for the case of wave propagation in a rod.

D. APPLICATION TO DYNAMIC STRESS ANALYSIS

For application to a dynamic stress analysis problem*, the inverses of the coefficients and procedure outlined above are required. In general, a superposition integral must be formulated to incorporate a stress-optic (or strain-optic) coefficient and the variation of fringe order with time. If the engineering approximation of colinear optical and principal mechanical axes cannot be made, the treatment will follow the lines suggested by Read (44) and referred to earlier in which all measurements and components are taken with respect to a fixed x-y coordinate system.

Again, however, the coefficients themselves are uniquely defined. Analogous to 3.12, the constitutive equation defining the time-dependent model stress-birefringence operator K_σ is

$$\sigma_1 - \sigma_2 = K_\sigma n \, . \tag{3.31}$$

Laplace transformation of 3.31 yields

$$\overline{\sigma}_1(p) - \overline{\sigma}_2(p) = K_\sigma(p)\, \overline{n}(p) \tag{3.32}$$

where $K_\sigma(p)$ may be termed the operational stress-birefringence coefficient in analogy to an operational modulus. Comparison of 3.32 with 3.15 reveals that

---

* For a recent comprehensive summary of viscoelastic stress analysis procedures, consult Williams (56).

$$K_\sigma(p) = \frac{1}{C_\sigma(p)} \quad . \tag{3.33}$$

Considering for analytical purposes only a relaxation type of test in which a step input in fringes is made and maintained by suitably varying the stress, a relation similar to 3.22 is readily derived:

$$K_\sigma(p) = p\,\overline{K}_{\sigma_{rel}}(p) \quad . \tag{3.34}$$

This defines a relaxation stress-birefringence coefficient where it should be noted that the relaxation in stress results from a constant fringe condition rather than constant strain. The relation is unique however inasmuch as stress and strain are uniquely related for any given process in time. Combining 3.34 with 3.33 and 3.22 gives

$$\overline{K}_{\sigma_{rel}}(p) = \frac{1}{p^2 \overline{C}_{\sigma_{crp}}(p)} \quad . \tag{3.35}$$

Thus, by one of the methods proposed in Section 3.4 for converting mechanical relaxation modulus and creep compliance, the time dependent function $K_{\sigma_{rel}}(t)$ can be obtained from 3.35.

A parallel derivation for the strain variation for a step fringe input gives a K_ϵ relation similar to 3.21 and finally leads to

$$\overline{K}_{\epsilon_{crp}}(p) = \frac{1}{p^2 \overline{C}_{\epsilon_{rel}}(p)} \tag{3.36}$$

which can also be converted to a time function suitable for use in a superposition integral to obtain the variation of strain with a

time-dependent fringe history.*

* Specific interconversions for these coefficients are presented in reference 40 but are not included here inasmuch as the fringe order prediction follows from the analytically determined stresses; thus 3.25 is the required characterization.

PART IV

PHOTOVISCOELASTIC OBSERVATION OF WAVE PHENOMENA

Analysis of stress wave phenomena by means of experimental photoclasticity involves a significant increase in complexity over the static and quasi-static situations. Primary attention must be paid to the photographic recording of a rapidly changing stress field which implies a short exposure time to stop the motion. Intense monochromatic light sources along with fine-grain high speed films are a necessity.

Although important information can frequently be deduced solely from isochromatic patterns especially at free or normally loaded boundaries or along lines of symmetry, the quantitative specification of a two-dimensional stress state at an internal point requires in general three independent pieces of information. These are usually the isochromatics, isoclinics and isopachics. The last of these can often be replaced in a static problem by a plane stress elasticity relation. In the dynamic situation it appears impractical to observe all three quantities simultaneously, and therefore the same test must be repeated a number of times. This implies rather precise, and perhaps impossible, repeatability of loading and material response.

Since most wave propagation phenomena in solids occur very rapidly, the depiction of the stress time history requires the evaluation of a large number of fringe patterns. The efficient handling of such a data reduction problem looks eventually toward some form of automated treatment.

Finally, as has been treated extensively in Part III, the use of viscoelastic media imposes the additional considerations of mechanical and optical response variation with rate of loading.

As reported by Goldsmith (57) in a recent comprehensive survey, great strides have been made in developing satisfactory equipment and methods to meet these requirements. Long since developed to a high degree for making static observations, photoelasticity was initially applied in a significant manner to a dynamic elastic situation in the mid-1930's. Tuzi and Nisida (58) in 1936 employed a streak camera to obtain a high equivalent framing rate. In 1939 Findley (59) utilized a rotating drum camera and spark illumination to obtain full image photographs. Subsequently Senior and Wells (60) used an ordinary camera and a flash type light source to produce single photographs of fringe patterns. Records of stress wave propagation in glass and perspex were obtained by Christie (61) who employed a high speed multiple spark and lens camera. Attempts to increase the framing rates of cameras led to the work of Sutton (62), Feder et al. (63), and Williams et al. (64). The last of these papers describes the development of a 200,000 frames-per-second drum-type camera based on the Ellis principle (65) which has been utilized in the two-dimensional testing discussed in Section B below.

The first effort in the use of materials of low moduli of elasticity was due to Perkins (66) who in 1953 obtained photographs of stress wave propagation in photoelastic rubber and gelatin using a 16 mm Fastax camera. Such relatively soft materials have

stress wave speeds an order of magnitude lower than materials used previously, with an attendant easing of the high speed photography problem. Durelli and co-workers (36, 37, 67) have developed this technique to a high state using Hysol 8705 material.

These low modulus materials, however, are for the most part high polymers and depending on the temperature respond viscoelastically. None of the foregoing experimentalists have attempted to include an analysis of the viscoelastic influence on their results. As pointed out recently by Kolsky and Lee (68), the difficulties associated with viscoelastic materials for this application remain to be treated. While a sketchy calibration at low strain rates has been given (36) and may be adequate for some mechanical loading situations, the complete spectrum coverage of birefringence characteristics for Hysol 8705 has been lacking until now.* The results of Part III are intended to remedy this situation.

The continued use of Hysol type materials in photo analysis has been reinforced by interest in the effects on various solid bodies of traveling pressure waves generated by high yield explosive devices. This so-called ground shock problem is formulated as the two-dimensional experiment presented in Section B. Indeed, when the technique was originally reported (42), it stimulated a more exhaustive investigation (69) incorporating strain measurements as well as fringe patterns. Yet this latter study still did

* However, as noted in Part III, some other epoxy materials of higher modulus have been characterized (39) concurrently with the present investigation.

not adequately consider viscoelastic effects. Hence, as suggested by Flynn, et al. (70), the calibrations and comparisons presented here are most appropriate to establish a firm basis for the photo-viscoelastic method.

Before taking up the two-dimensional thin plate under the sudden pressure loading of an aerodynamic shock wave, we consider first the results of photoviscoelastic tests of uniaxial wave propagation in a rectangular bar.

A. VISCOELASTIC BAR WITH STEP PRESSURE LOADING

As part of the verification of the proposed photoviscoelastic theory, a comparison has been made between the predicted fringe patterns and those obtained experimentally. The one-dimensional test data from a separate GALCIT research program referred to previously (40) are correlated with the results from Parts I and III.

The experimental equipment and procedure are described only briefly here; the reader is referred to reference 40 for details. The model consisted of a $0.365 \times 0.875 \times 3.5$ inch prismatic bar of Hysol 8705 material mounted at the exhaust end of a small rectangular aerodynamic shock tube (described more fully in Section B below). The end of the specimen fitted the shock tube opening (except for a small gap around the periphery) and extended about 1/4 inch into the tube. The tube and bar were mounted vertically to reduce bending of the model to a minimum and produce essentially axial loading by the shock wave as it traveled down the tube and impinged on the leading end of the bar. The shock wave loading represents a step

pressure input, corresponding to the boundary condition specified for the rod in Part I. A Kistler 605B quartz piezoelectric pressure transducer was used to determine the magnitude of the step pressure input. For the tests described here, it was 59 psi to an accuracy of better than 10%; this value agreed well with the reflected pressure calculated by elementary shock tube theory.

A polariscope was provided to record time dependent fringes, the camera being an Eastman Kodak 16 mm camera capable of taking pictures at the rate of 3300 frames per second. While a higher framing rate would have been preferable, this camera provided three frames during the event so that a time history could be estimated. Fig. 26 taken from reference 40 shows enlargements of three frames from a typical test of the series. The resulting diagram of position along the bar and arrival time for the various fringe order numbers is given in fig. 27. From this curve the experimental variation (fig. 24) of n vs. t for x = 1.67 cm and x = 3.81 cm was derived.

The most prominent difference to be noted is the more gradual rise in experimental fringe order early in the response period compared to that predicted by theory using calibrated material properties. Near the end of the wave arrival however the test values are approximately 5% higher than predicted, but this is still within the possible variation already noted in the measurement of the applied pressure.

Probably the major reason for the discrepancy can be sought in the effect of lateral inertia and the higher modes of transmission. In a compressional wave, the accompanying tendency for the material at the wave front to expand outward is resisted by its inertia; hence

this acts as an equivalent compressive stress so that the difference in principal stresses is less than if inertia forces are neglected. Thus until the wave has essentially passed, the number of fringes would be fewer than predicted by the simple one-dimensional theory. Associated with this stress-free boundary effect are the higher modes of wave propagation. While phase velocities in these modes can become quite large, the group velocity of energy transmission is always less than that of the rod velocity. Furthermore the rectangular bar geometry introduces a wave propagation modification from that of the thin bar or rod. Elastic analysis by Gazis and Mindlin (71) shows that the coupling of width and thickness modes decreases the velocity of low-frequency components below the corresponding plane stress values. The speed of propagation seems definitely to be involved, for in order to compare fringe pattern shapes from theory and experiment, the origin of the predicted pattern for x = 3.81 cm in fig. 24 had to be increased by 0.75×10^{-4} sec. to make it coincide with the experimental fringe order curve. Thus the actual stress wave velocity was less than that predicted by the simple theory. For x = 1.67, near the front end of the model, no measurable shift was necessary.

Jones (72), besides noting this effect for wide rectangular bars, has investigated by approximate plane-stress elasticity equations the warping of plane sections during wave propagation and qualitatively predicts curved photoelastic fringe patterns of the type shown in fig. 26. The deviation from the plane cross-section characteristic

assumed in the stress analysis of Part I would introduce modifications to the fringe pattern which represents integrated optical effects throughout the thickness of the bar.

An additional factor of possible significant influence was the high pressure gases that spilled out around the side of the model at the mouth of the shock tube. Such pressure exerted on the faces of the model would also reduce the fringe order at short times; however at greater distances from the leading end of the model (e.g., at 3.81 cm), its effect should appear considerably diminished, which is not the case in fig. 24. Hence it is not believed to be an important contributing factor.

Finally, there is some preliminary indication (40) that a more precise calibration of $C_{\sigma_{crp}}$ using a photocell would place its transition region (fig. 23) at a slightly later time. This too would be in a direction to cause the predicted and experimental curves to coincide.

Despite the discrepancies just noted, there is sufficient evidence to draw some definite even though qualitative conclusions. The difference between the results from a constant (static) birefringence coefficient and a photoviscoelastically-calibrated function indicates the necessity of suitably characterizing any viscoelastic material that is to be used in photoclastic stress analysis. The modification of the resulting birefringence time response shown in fig. 24 is qualitatively correct. For the case of Hysol 8705, the birefringence relaxation processes are quite rapid and imply for dynamic phenomena with

stress rise times of the order of slightly greater than 10^{-4} sec that the modification to effective fringe value is no larger than 20% during the transient period.

Thus, tentatively it appears that Hysol 8705 has some very desirable features from a viscoelastic standpoint for dynamic photoelastic investigation. On the other hand, the associated rapid attenuation of high frequency components would be a disadvantage in certain applications. In more rapid events in Hysol 8705, and especially in other photoviscoelastic materials, the variation in the operative birefringence value can be considerably larger. In either case, the method of calibration and application of viscoelastic birefringence operators proposed here places the technique of photoviscoelasticity on a firmer theoretical and practical foundation.

B. THIN PLATE UNDER SHOCK WAVE LOADING

A second aspect of the verification of the photoviscoelastic theory involves the study of a two-dimensional thin plate geometry approximating that analyzed in Part II. Chronologically, this experimental program preceded the rest of the material reported herein and served as the stimulus to the previous photoviscoelastic calibration investigation inasmuch as it was discovered that no adequate method existed for handling the viscoelastic aspects of high polymer birefringent materials.

The original test series (42) examined the effect of an aerodynamic shock wave passing over the upper edge of a slab of photoelastic material, with the resulting stress-wave photoelastic pattern

being photographed by a high speed camera. In addition, various geometries including the simulated semi-infinite plate, covered and uncovered cutouts at the surface of the material, and layered media were examined (18). Of basic interest in the present study, however, is the comparison with predicted fringe patterns for the semi-infinite plate from Parts II and III.

4.1 Experimental Apparatus

The basic specimen, a 12 inch square plate of 1/2 inch thick Hysol 8705, was mounted at the end of the aerodynamic shock tube as shown in fig. 28. The 1/2 inch by 1 inch rectangular tube utilized nitrogen gas as a driving fluid in the high pressure chamber and exhausted into an enclosed rectangular area at atmospheric pressure over the model. Upon rupture of the diaphragm material (one or more layers of mylar placed between the pair of flanges at the right of fig. 28), a shock wave formed, traveled down the tube, and passed over the top edge of the two-dimensional model. The pressure jump across the shock front induced a propagating stress wave in the model.

Two Microdot high frequency electrical leads attached to the shock tube sent the signal of the passing shock wave from two resistance thermometer pick-ups (located ten inches apart in small inserts near the exhaust end of the tube) to an amplifier and Berkeley 7360 microsecond counter. A thin narrow platinum film sputtered onto the glass pick-up body acted as an electrical conductor of small thermal inertia whose resistance varied with temperature.* The amplifier

* The manufacture and operation of these pick-ups have been described by Rabinowitz, et al. (73).

boosted the signal generated by the temperature jump existing across a passing shock wave. The two pulses activated the counter to give the velocity of the shock wave and, after suitable time delays, also initiated the photographic cycle by firing the light source and tripping the camera shuttering action.

Some of the optical elements of the polariscope are shown in fig. 28 behind the model at the end of the tube. A close-up of the model in its holder is shown in fig. 29. As shown, the specimen is enclosed on the vertical faces and on the top by plexiglass (essentially not birefringent) plates. Hence in effect the shock tube is extended unchanged in shape to the end of the model holder with the upper edge of the model forming the lower boundary of this part of the tube. The face plates in the region enclosing the model are slightly recessed to leave a small clearance between them and the model material itself. Thus the configuration is a relatively thin slice of material with free surfaces and approaches a two-dimensional plane stress situation.

4.2 Camera Design

The high-speed Ellis-type framing camera developed during the past few years at the Guggenheim Aeronautical Laboratory was used in these photoelastic experiments. Its design has been extensively described (64) and hence only a brief review of the camera and auxiliary equipment is necessary.

The schematic layout of the camera assembly and photoelastic bench is shown in fig. 30. The camera itself consists of a circular drum whose axis coincides with the optical axis of the photoelastic bench. A bevelled mirror is mounted on a shaft at the center of the

drum and driven by an air turbine. The mirror reflects the image through 90° and flashes it onto the stationary film track around the complete periphery of the drum. Space is provided in the drum for 128 frames of 35 mm film.

The photoelastic bench is a conventional straight-through type employing 10-inch diameter lenses. With such a large optical field, a diffused light source consisting of a 5-kilovolt Xenon flash tube in a parabolic reflector and a frosted glass proved to give the best results. The polarizer and quarter wave plate produce circularly polarized light to illuminate the specimen (denoted S in the figure). The final quarter plate and analyzer complete the basic elements of the polariscope.

The lone remaining item listed in the schematic layout, the pulse circuit, is shown in the block diagram, fig. 31. Here are indicated the camera assembly and photoelastic bench, and between them the Kerr cell, which is essentially an electrical shuttering device to provide the extremely rapid framing rate and short exposure times. The principle of operation depends on the fact that nitrobenzine in an electrically charged field becomes optically birefringent until the charge is removed. Thus when a pulsed voltage of the proper magnitude is applied to the plates in the cell, it acts as a half wave plate which, in conjunction with a pair of crossed polaroids, produces a shutter of extremely rapid response time. The appropriate voltage, depending on the size and spacing of the electrodes, is 20 kilovolts in this case. The pulses are synchronized with the mirror rotation by a magnetic pick-up on the rotating shaft.

The other major components indicated on the block diagram are the control chassis, the power amplifier for the Kerr cell pulses, the initiator circuit, and the input power control unit. The camera operates at framing rates in excess of 100,000 frames per second and a fixed exposure time of 0.1 microsecond.

The large photoelastic field, the extremely short exposure time, and the fact that Hysol 8705 is not completely transparent imposed some serious limitations on the photographic film density that could be obtained. The 35 mm film selected as both fast enough and sufficiently fine-grained was Agfa Isopan Record film with a nominal ASA rating of 640.

4.3 Semi-Infinite Plate Geometry

The principal two-dimensional investigation involved the semi-infinite plate geometry loaded on the upper edge by the passing shock wave. Experimentally the semi-infinite character is simulated by the fairly large model size so that all the wave propagation events of interest are photographed before any reflections from the boundaries occur. The high-speed motion pictures shown in fig. 32 are from such a test on Hysol 8705. The framing rate was 72,000 frames per second with an exposure time of 0.1 μsec. The nitrogen pressure in the reservoir at rupture of the shock tube diaphragm was 750 psi at a temperature of 75°F. As it passed through the test section over the specimen, the shock wave was traveling at 2210 feet per second. Shock tube theory predicts a sustained pressure situation for a distance of at least six inches

behind the shock front. The pressure differential across the shock for this test was approximately 70 psi (74). The time represented by the 16 frames shown in fig. 32 is approximately 230 microseconds beginning shortly after the shock wave started to move across the surface of the model.

The passage of the shock wave is evident from the stress fringe pattern spreading down at an angle across the model. After a short portion at a steepened angle near the surface, the leading heavy fringe is essentially linear for most of its length, but does exhibit some curvature near the left hand edge of the model. Before these facts are discussed in detail, the quasi-circular pattern proceeding ahead of the main stress fringes in fig. 32 should be noted. At first thought to be part of the stress wave propagation phenomenon, it was further investigated with a simplified model holder that permitted the high pressure gas behind the shock wave to escape from the model faces about one-quarter inch below the top surface of the model. No such pattern appeared with this modified set-up, indicating that the effect is due to high pressure gas acting in the slight clearance between the specimen and its enclosing plexiglass face plate to compress the model material. That is, the photoelastic effect displayed in the model, a partial order fringe, is in reality due to an air-propagated pressure wave rather than a solid-propagated stress wave. The pattern does not appear with polaroids removed, which confirms its photoelastic nature. While it consequently does not immediately concern the study of stress wave propagation in

solids, it is of some interest as a possible method of experimentally creating a stress field.

The shock wave speeds for several runs of the type shown in fig. 32 have varied between (aerodynamic) Mach numbers of 1.7 and 2.1. These are clearly faster than any of the photoelastically discernible stress effects propagated in the Hysol 8705 material as evidenced by the fringe patterns. This conclusion correlates with the analytical results of Part II; thus these tests while "supersonic" relative to the first significant stress arrivals would actually be in the subsonic regime relative to glassy dilatation wave speeds in the material. In the notation of Part II, $M_{\phi} = 0.605$ for the illustrated test. Additionally, these tests have established the essential linearity of the photoelastic fringe front, but they also showed a curved characteristic in the vicinity of the vertical boundary adjacent to the shock tube exit. Fig. 33, which is an enlarged view of one of the frames from the film strip of fig. 32, illustrates these features in greater detail. Correlating with the transient elastic analysis of Ang (26) for a moving line load, the curvature of the wave front near the left boundary of fig. 33 is believed to represent the start-up transient effects near the point at which the shock wave first comes in contact with the model. The linear portion of the fringe pattern corresponds to the steady-state region of the model.

As may be observed, the angle between the leading half-order stress fringe and the surface along which the shock wave travels is approximately 11°. This angle corresponds approximately

to the leading significant components of the dilatation wave. It is interesting to note that its propagation speed is readily obtained by a calculation exactly analogous to that for the geometry of Mach waves in aerodynamics, except that here the moving disturbance is the shock wave and the Mach wave becomes the dilatation front in the material. Using the shock wave speed of 2210 feet per second, the stress wave propagation speed by this calculation is 425 feet per second. On the basis of the viscoelastic theory of Part III, it is somewhat hazardous* to attempt to predict the effective material modulus from the propagation speed of the leading photoelastic fringe by use of the longitudinal plate wave velocity equation

$$c_p = \left\{\frac{E}{\rho(1-\nu^2)}\right\}^{\frac{1}{2}} . \qquad (4\text{-}1)$$

Rather, this relation precisely applies to each stress component as it arrives, and the fringes, as pointed out heretofore, are the result of integrated energy propagation contributions which are necessarily spread out by dispersion for a viscoelastic material.

Similarly to the one-dimensional case, a comparison has been made of the predicted and observed fringe order numbers for two positions in the model (fig. 25). The photoelastic data for x = 3.12 in were taken from the frame shown in fig. 33. As pointed out in the analysis leading to the prediction of fringes in

* A recent report (18) discussed some of the problems associated with analysis of dynamic photoelastic results.

Part III, the plane stress results do not precisely apply to the half-inch thick plate and the comparison is consequently made on the basis of the normalized coordinate n/n_{max}. Indeed the plane strain solution of Part II indicated nearly a hydrostatic stress state which would result in approximately a nul fringe pattern. The actual recorded fringe values did fall between this and the predicted plane stress pattern, indicating qualitative verification of the theoretical approach for two-dimensional photoviscoelastic application. The general agreement of the shape of the fringe patterns for x = 3.12 in and x = 10.3 in shown in fig. 25 further substantiates this conclusion.

The nature of the discrepancy between predicted and experimental fringe values is similar to that found in the case of uniaxial wave propagation (fig. 24). The source of the differences can be discussed on the basis of all the factors mentioned in the parallel analysis of the one-dimensional geometry (Section A), e.g., higher modes, lateral inertia, and non-plane wave fronts. Thus, future work in two-dimensional viscoelasticity can profitably include these effects to provide further quantitative verification of the proposed photoviscoelastic method for analyzing dynamic stress states. Another variable not accounted for was the slight rotation of principal stress axes with time which might produce some non-alignment of these with respect to the optical polarization axes. But as pointed out in Part II, this probably is a negligible factor in the present tests.

Hence, the two-dimensional results strengthen the conclusions derived earlier from the uniaxial analysis and tests. The qualitative

agreement obtained for the plate geometry indicates that extension of the photoviscoelastic techniques to two-dimensional situations is justified using the same basic viscoelastic optical calibration of the material.

CONCLUSIONS

Since the distinguishing characteristic of viscoelastic material is its strong sensitivity to rate and temperature effects, they must be adequately accounted for in dynamic situations. An improved method of incorporating the time or rate dependency in the analysis of certain wave propagation problems has been developed. The Dirichlet series not only represents the broad-band properties of many actual viscoelastic materials much more closely than the widely-used simple spring and dashpot models of two to four elements, but in conjunction with the collocation inversion procedure also circumvents the computational difficulties inherent in the usual Laplace transform type of solution.

The method can be made as accurate as desired for any application with no essential increase in mathematical difficulty simply by taking more terms in the series. It is believed that this property represents a distinct advantage over the analytical model representation used in previous treatments of viscoelastic wave propagation. For most situations, ten to fifteen terms in the series prove to be adequate; the resulting matrices are nearly triangular and can sometimes be inverted by hand, but the computational part is more readily accomplished by relatively simple and rapid computer programs.

The solution technique has been applied to one- and two-dimensional problems characterized by step input mechanical loading. The one-dimensional rod analysis indicates several of the features associated with waves traveling in realistic viscoelastic materials.

The high frequency components of the response to a step input are rapidly attenuated with distance and the major portion of the rise in stress or displacement occurs near the rubbery arrival time. In addition, just prior to the main stress arrival, there appears an oscillation in stress (due to material dispersion) that has not been evident heretofore in the solutions using less adequate simple model representations.

The results for an infinite half-space loaded by a supersonically moving step pressure pulse indicate that the viscoelastic normal stresses can be about 12% higher than in the corresponding elastic case. The stress rise time Δt is directly proportional to depth in the half-space; moreover, it appears feasible to formulate an expression for Δt in terms of a specific viscoelastic parameter of the material involved. The semi-infinite thin plate has also been treated, indicating the range of application of the combined Dirichlet series and collocation inversion approach.

The application of photoviscoelastic materials to model the responses due to dynamic loading has been placed on a firmer theoretical and practical foundation as a result of an investigation of the methods of optical calibration and the use of birefringence operators analogous to the mechanical operational moduli. The theoretical relationships between stress optic and strain optic coefficients for linearly viscoelastic materials have been derived. It is emphasized that this operator relationship is the one item needed to characterize the material for photoviscoelastic application; all other pieces of data, such as variation of fringe order number with time and the

possible lag between optical and mechanical responses as indicated by the time-dependent isoclinics, are dependent on the individual experiment being performed. A convenient method of calibration in a constant strain rate test has been illustrated for a typical low modulus polymer material.

A comparison of theoretically predicted fringe patterns with experimental results for the cases of the rod and semi-infinite plate geometries under quasi-step pressure inputs has demonstrated the general necessity of including the time dependency in treatment of photoviscoelastic material properties. The agreement has also indicated the feasibility of quantitative photoviscoelasticity for dynamic stress analysis.

REFERENCES

1. Kolsky, H.: Stress Waves in Solids. Clarendon Press, Oxford, 1953.

2. Rayleigh, Lord: Theory of Sound. Dover Publications, New York, 1945.

3. Pochhammer, L.: Über die fortphlanzungsgeschwindigkeiten schwingungen in einem unbegrenzten isotropen Kreiszylinder. J. reine angew. Math., vol. 81, 1876, pp. 324-336.

4. Chree, C.: The Equations of an Isotropic Elastic Solid in Polar and Cylindrical Coordinates, Their Solutions and Applications. Trans. Camb. Phil. Soc., vol. 14, 1889, pp. 250-369.

5. Davies, R. M.: A Critical Study of the Hopkinson Pressure Bar. Phil. Trans. Roy. Soc. Lond. (A), vol. 240, 1948, pp. 375-457.

6. Lee, E. H., Morrison, J. A.: A Comparison of the Propagation of Longitudinal Waves in Rods of Viscoelastic Materials. J. Pol. Sci., vol. 19, 1956, pp. 93-110.

7. Arenz, R. J.: Uniaxial Wave Propagation in Realistic Viscoelastic Materials. GALCIT SM 63-12, California Institute of Technology, Pasadena, California, March 1963 (to be published in J. Appl. Mech.).

8. Bland, D. R.: The Theory of Linear Viscoelasticity. Pergamon Press, New York, 1960.

9. Kolsky, H.: Experimental Wave Propagation in Solids. Proceedings of the First Symposium on Naval Structural Mechanics. Pergamon Press, New York, 1960, pp. 233-260.

10. Gross, B.: Mathematical Structure of the Theories of Viscoelasticity. Hermann and Cie., Paris, 1953.

11. Berry, D. S., Hunter, S. C.: The Propagation of Dynamic Stresses in Viscoelastic Rods. J. of Mech. and Phys. of Solids, vol. 4, 1956, pp. 72-95.

12. Lee, E. H.: Stress Analysis in Viscoelastic Bodies. Q. Appl. Math., vol. 13, 1955, pp. 183-190.

13. Morrison, J. A.: Wave Propagation in Rods of Voigt Material and Viscoelastic Materials with Three-Parameter Models. Q. Appl. Math., vol. 14, 1956, pp. 153-169.

14. Schapery, R. A.: Approximate Methods of Transform Inversion for Viscoelastic Stress Analysis. Proceedings of the Fourth U.S. National Congress of Applied Mechanics. Published by The American Society of Mechanical Engineers, 1962, pp. 1075-1085.

15. Schapery, R. A.: Irreversible Thermodynamics and Variational Principles with Applications to Viscoelasticity. Ph.D. Thesis, California Institute of Technology, Pasadena, California, 1962.

16. Erdelyi, A.: Note on an Inversion Formula for the Laplace Transform. J. Lond. Math. Soc., vol. 18, 1943, pp. 72-77.

17. Landel, R. F.: Mechanical Properties of a Polyurethane Elastomer in the Rubber-to-Glass Transition Zone. J. Coll. Sci., vol. 12, 1957, pp. 308-320.

18. Arenz, R. J., Fourney, M. E.: On the Photoelastic Study of Stress Wave Propagation. GALCIT SM 61-12, California Institute of Technology, Pasadena, California, June 1961.

19. Williams, M. L., Blatz, P. J., Schapery, R. A.: Fundamental Studies Relating to Systems Analysis of Solid Propellants. GALCIT SM 61-5, California Institute of Technology, Pasadena, California, February 1961 (ASTIA Report No. AD 256-905).

20. Hunter, S. C.: Viscoelastic Waves. Progress in Solid Mechanics. Interscience Press, New York, 1960, pp. 1-57.

21. Lubliner, J.: Surface Waves in a Viscoelastic Half-Space. ONR Contr. 266(08) T.R. No. 24, Columbia University, New York, April 1960.

22. Sackman, J. L.: Stresses in a Viscoelastic Half-Space Due to a Progressing Surface Pressure. Proceedings of the Fourth U.S. National Congress of Applied Mechanics. Published by The American Society of Mechanical Engineers, 1962, pp. 1067-1074.

23. Chu, B. T.: Stress Waves in Isotropic Linear Viscoelastic Materials. J. de Mec., vol. 1, 1962, pp. 439-462.

24. Sneddon, I. N.: Stress Produced by a Pulse of Pressure Moving along a Surface of a Semi-infinite Solid. Rend. Circ. Mat. di Palermo, vol. 2, 1952, pp. 57-62.

25. Cole, J., Huth, J.: Stresses Produced in a Half Plane by Moving Loads. J. Appl. Mech., vol. 25, 1958, pp. 433-436.

26. Ang, D. D.: Transient Motion of a Line Load on the Surface of an Elastic Half-Space. Q. Appl. Math., vol. 18, 1960, pp. 251-256.

27. Arenz, R. J.: Transient Motion of a Line Load Moving at Supersonic Speed on the Surface of an Elastic Half-Space. GALCIT SM 60-7, California Institute of Technology, Pasadena, California, May 1960.

28. Miles, J. W.: On the Response of an Elastic Half-Space to a Moving Blast Wave. J. Appl. Mech., vol. 27, 1960, pp. 710-716.

29. Ferry, J. D.: Viscoelastic Properties of Polymers. John Wiley and Sons, New York, 1961.

30. Surland, C. C.: Strain Measurements on Hydrostatically Stressed Materials Using Differential Transformer Transducers. Aerojet-General Corporation Report, Azusa, California, 1961.

31. Lamb, H.: On Waves in an Elastic Plate. Proc. Roy. Soc. Lond. (A), vol. 93, 1917, pp. 114-128.

32. Mindlin, R. D.: Waves and Vibrations in Isotropic, Elastic Plates. Proceedings of the First Symposium on Naval Structural Mechanics. Pergamon Press, New York, 1960, pp. 199-232.

33. Holden, A. N.: Longitudinal Modes of Elastic Waves in Isotropic Cylinders and Slabs. Bell Syst. Tech. J., vol. 30, 1951, pp. 956-969.

34. Sokolnikoff, I. S.: Mathematical Theory of Elasticity. McGraw-Hill Book Company, New York, 1956.

35. Bishop, R.E.D.: On Dynamical Problems of Plane Stress and Plane Strain. Q. J. of Mech. and Appl. Math., vol. 6, 1953, pp. 250-254.

36. Dally, J. W., Riley, W. F., Durelli, A. J.: A Photoelastic Approach to Transient Stress Problems Employing Low Modulus Materials. J. Appl. Mech., vol. 26, 1959, pp. 613-620.

37. Dally, J. W., Riley, W. F., Durelli, A. J.: Photoelastic Study of Stress Wave Propagation in Large Plates. Proc. of Soc. Exp. Stress Anal., vol. 17, 1960, pp. 33-50.

38. Theocaris, P. A., Mylonas, C.: Viscoelastic Effects in Birefringent Coatings. J. Appl. Mech., vol. 28, 1961, pp. 601-607.

39. Theocaris, P. S.: Viscoelastic Properties of Epoxy Resins Derived from Creep and Relaxation Tests at Different Temperatures. Rheologica Acta, vol. 2, 1962, pp. 92-96.

40. Williams, M. L. et al.: The Dynamic Characterization of Photoviscoelastic Materials. GALCIT SM 63-31, California Institute of Technology, Pasadena, California, September 1963.

41. Bollard, R.J.H., Dill, E. H.: Thermal Grain Structural Analysis, Appendix A: Photothermoviscoelasticity. LPC Report 578-P-11, Lockheed Propulsion Company, Redlands, California, October 1962.

42. Arenz, R. J., Williams, M. L.: A Photoelastic Technique for Ground Shock Investigation. Ballistic Missile and Space Technology. Academic Press, New York, 1960, vol. 4, pp. 137-152.

43. Mindlin, R. D.: A Mathematical Theory of Photo-Viscoelasticity. J. Appl. Phys., vol. 20, 1949, pp. 206-216.

44. Read, W. T.: Stress Analysis for Compressible Viscoelastic Materials. J. Appl. Phys., vol. 21, 1950, pp. 671-674.

45. Theocaris, P. S., Mylonas, C.: Discussion of the Paper on Viscoelastic Effects in Birefringent Coatings. J. Appl. Mech., vol. 29, 1962, pp. 598-603.

46. Keedy, D. A., Volungis, R. J., Kawai, H.: The Use of an Instron Testing Machine for the Determination of Stress and Strain-Optical Coefficients. ONR Contr. 2151(00), T.R. No. 24, University of Massachusetts, Amherst, Massachusetts, August 1960.

47. Trehoar, L.R.G.: The Physics of Rubber Elasticity. Clarendon Press, Oxford, 1958.

48. Tobolsky, A. V.: Stress Relaxation Studies of the Viscoelastic Properties of Polymers. J. Appl. Phys., vol. 27, 1956, pp. 673-685.

49. Landel, R. F., Smith, T. L.: Viscoelastic Properties of Rubberlike Composite Propellants and Filled Elastomers. Am. Rocket Soc. J., vol. 31, 1961, pp. 599-608.

50. Williams, M. L., Landel, R. F., Ferry, J. D.: The Temperature Dependence of Relaxation Mechanisms in Amorphous Polymers and Other Glass-Forming Liquids. J. Am. Chem. Soc., vol. 77, 1955, pp. 3701-3707.

51. Williams, M. L.: On the Stress and Strain Relation with Dynamic Birefringence. GALCIT SM 62-25, California Institute of Technology, Pasadena, California, April 1962.

52. Williams, M. L., Arenz, R. J.: Dynamic Analysis in Viscoelastic Media. Proceedings of Symposium on Structural Dynamics under High Impulse Loading. Report No. ASD-TDR-63-140, Aeronautical Systems Division, Wright-Patterson Air Force Base, Ohio, May 1963, pp. 79-113.

53. Arenz, R. J.: A Method of Dynamic Fringe Prediction in Birefringent Viscoelastic Materials. GALCIT SM 63-25, California Institute of Technology, Pasadena, California, March 1963.

54. Schapery, R. A.: A Simple Collocation Method for Fitting Viscoelastic Models to Experimental Data. GALCIT SM 61-23A, California Institute of Technology, Pasadena, California, November 1961.

55. Knauss, W. G.: On the Mechanical Properties of an HC Rubber. GALCIT SM 63-1, California Institute of Technology, Pasadena, California, January 1963.

56. Williams, M. L.: The Structural Analysis of Viscoelastic Materials. Am. Inst. of Aero. and Astro. Paper No. 63-284, June 1963.

57. Goldsmith, W.: Dynamic Photoelasticity. NAVWEPS Report 8037, U. S. Naval Ordnance Test Station, China Lake, California, November 1962.

58. Tuzi, Z., Nisida, M.: Photoelastic Study of Stresses Due to Impact. Phil. Mag., ser. 7, vol. 21, 1936, pp. 448-473.

59. Findley, W. N.: The Fundamentals of Photoelastic Stress Analysis Applied to Dynamic Stresses. Proceedings of the Ninth Semi-Annual Photoelasticity Conference, 1939, pp. 1-11.

60. Senior, D. A., Wells, A. A.: A Photoelastic Study of Stress Waves. Phil. Mag., ser. 7, vol. 37, 1946, pp. 463-469.

61. Christie, D. G.: An Investigation of Cracks and Stress Waves in Glass and Plastics by High Speed Photography. Trans. Soc. Glass Tech., vol. 36, 1952, pp. 74-89.

62. Sutton, G. W.: A Photoelastic Study of Strain Waves Caused by Cavitation. J. Appl. Mech., vol. 24, 1957, pp. 340-348.

63. Feder, J. C., Gibbons, R. A., Gilbert, J. T., Offenbacher, E. L.: The Study of the Propagation of Stress Waves by Photoelasticity. Proc. Soc. Exp. Stress Anal., vol. 14, 1956, pp. 109-122.

64. Williams, M. L., Jessey, M. E., Parmerter, R. R.: Some Exploratory Photoelastic Studies in Stress Wave Propagation. Proc. Soc. Exp. Stress Anal., vol. 17, 1960, pp. 121-134.

65. Ellis, A. T.: Techniques for Pressure Pulse Measurements and High-Speed Photography in Ultrasonic Cavitation. Cavitation in Hydrodynamics, Philosophical Library, Inc. New York, 1957.

66. Perkins, H. C.: Movies of Stress Waves in Photoelastic Rubber. J. Appl. Mech., vol. 20, 1953, pp. 140-141.

67. Durelli, A. J., Riley, W. F.: Experiments on Transient Two-Dimensional Stress and Strain Distributions. J. Appl. Mech., vol. 24, 1957, pp. 69-76.

68. Kolsky, H., Lee, S. S.: The Propagation and Reflection of Stress Pulses in Linear Viscoelastic Media. ONR Contr. 562(30) T.R. No. 5, Brown University, Providence, Rhode Island, May 1962.

69. Riley, W. F., Daniel, I. M., Carey, J. J.: A Study of Stress Wave Interaction with Buried Structures. AFSWC-TDR-62-47, Armour Research Foundation, Illinois Institute of Technology, Chicago, Illinois, May 1962.

70. Flynn, P. D., Feder, J. C., Gilbert, J. T., Roll, A. A.: Stress Waves Due to Explosive and Mechanical Loading of Low Modulus Materials. Pitman-Dunn Laboratories Report, Frankford Arsenal, Philadelphia, Pennsylvania, June 1962.

71. Gazis, D. C., Mindlin, R. D.: Influence of Width on Velocities of Long Waves in Plates. J. Appl. Mech., vol. 24, 1957, pp. 541-546.

72. Jones, O. E., Ellis, A. T.: Longitudinal Strain Pulse Propagation in Wide Rectangular Bars: Part I--Theoretical Considerations. J. Appl. Mech. , vol. 30, 1963, pp. 51-60.

73. Rabinowicz, J., Jessey, M. E., Bartsch, C. A.: Resistance Thermometer for Heat Transfer Measurement in a Shock Tube. GALCIT Hypersonic Research Project Memorandum No. 33, California Institute of Technology, Pasadena, California, July 1956.

74. Yoler, Y.: The Hypersonic Shock Tube. Ph.D. Thesis, California Institute of Technology, Pasadena, California, 1954.

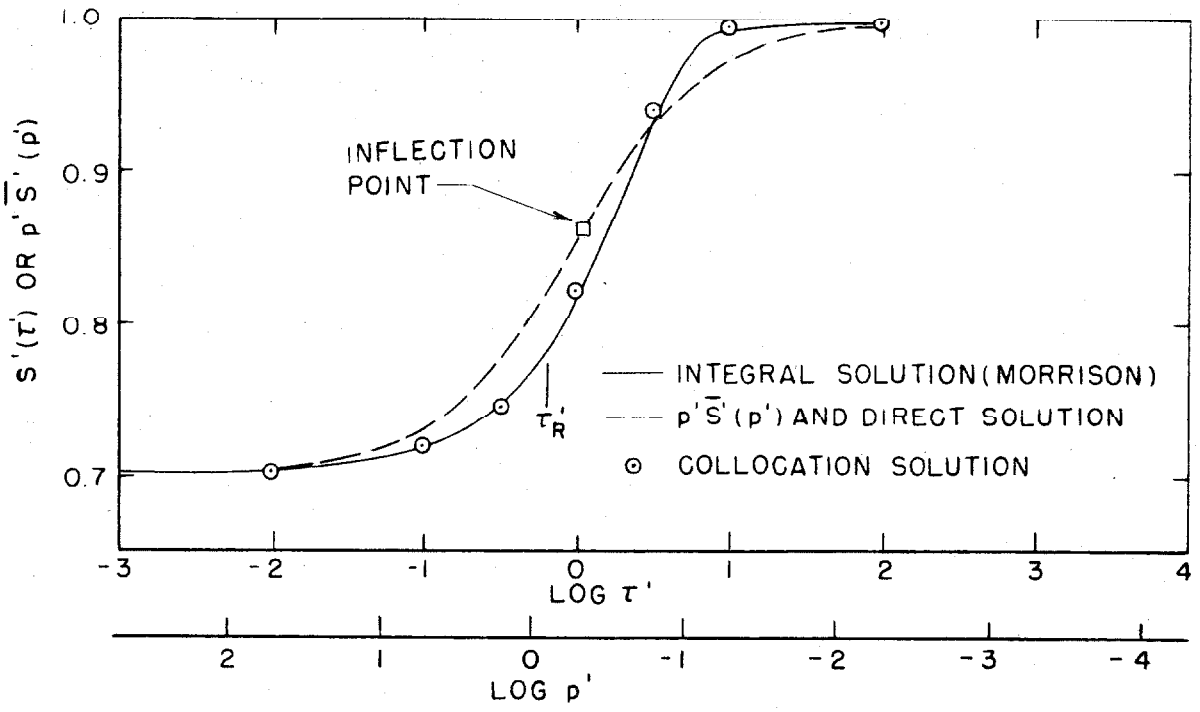

FIG. 1 RESPONSE TO STEP STRESS INPUT OF STANDARD LINEAR SOLID ROD FOR CASE $E = E'$, $\xi = 2.0$

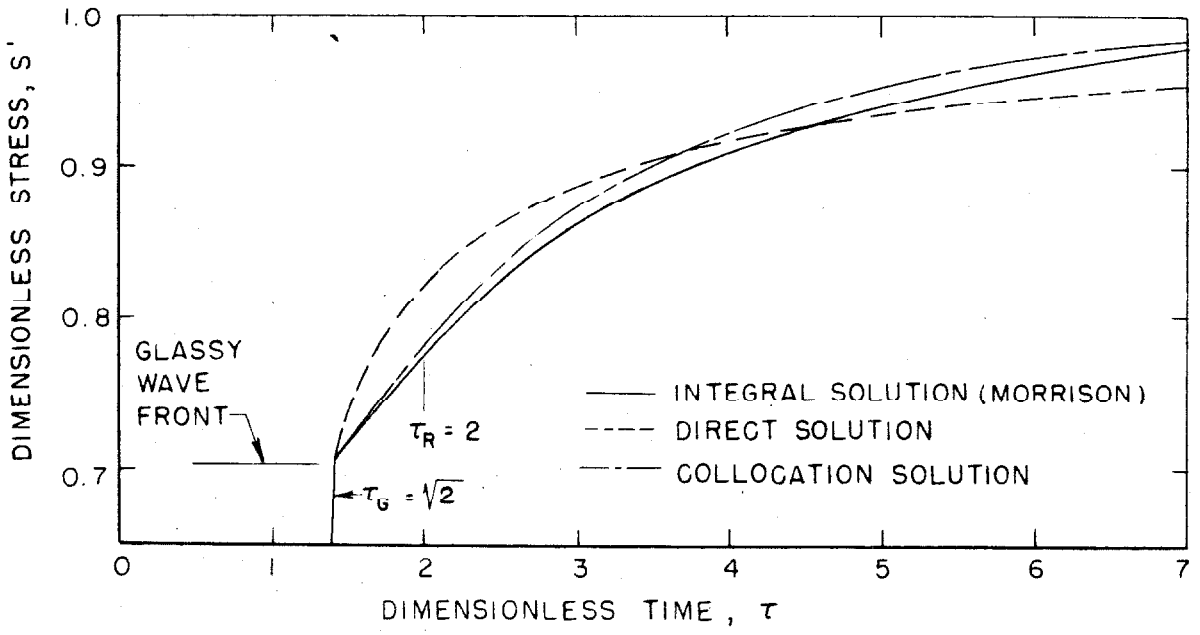

FIG. 2 COMPARISON OF SOLUTIONS FOR STANDARD LINEAR SOLID ROD WITH STEP STRESS INPUT; $E = E'$, $\xi = 2.0$

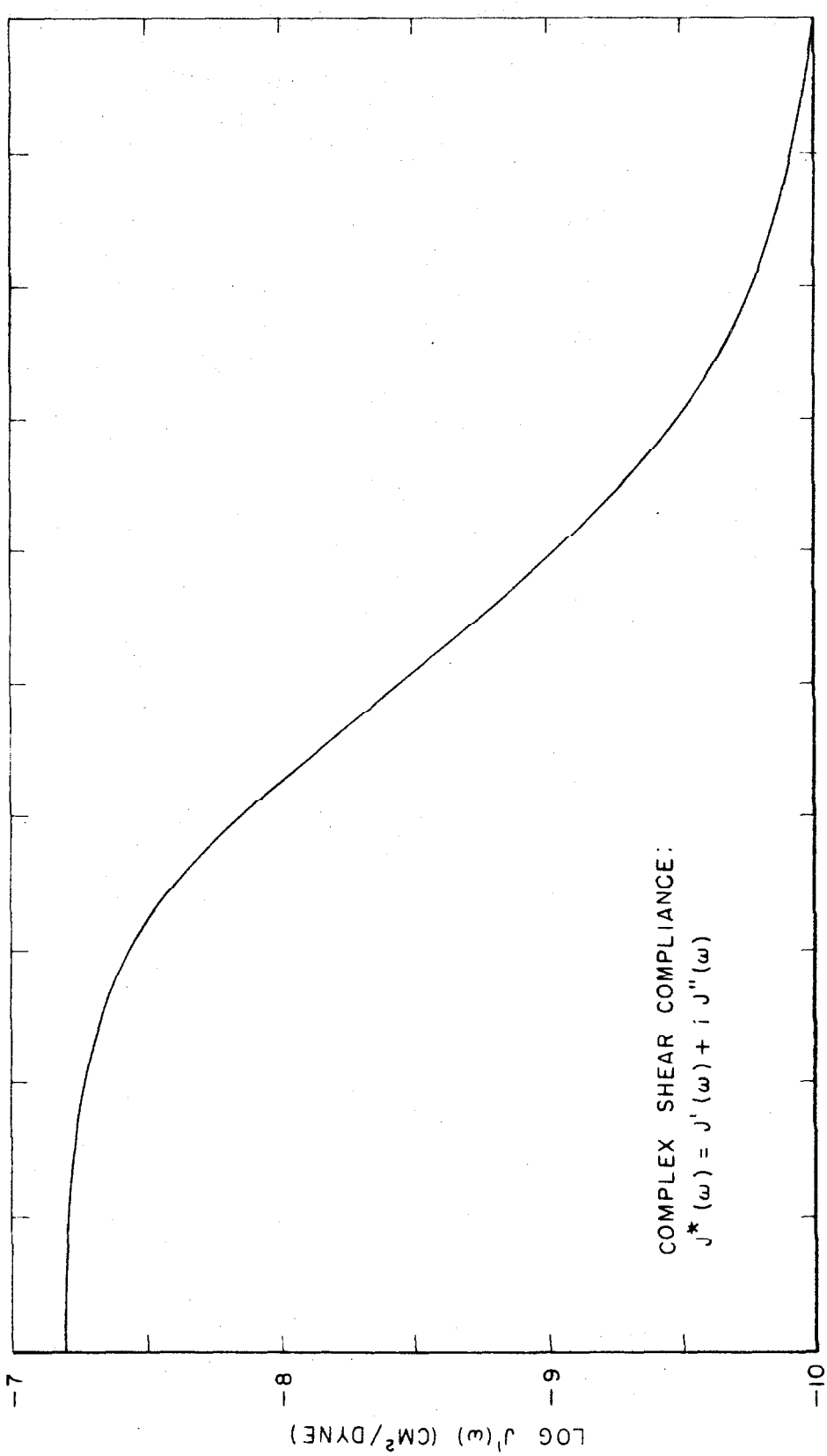

FIG. 3 REAL PART OF THE COMPLEX SHEAR COMPLIANCE FOR POLYURETHANE MATERIAL; TEMPERATURE=14°C

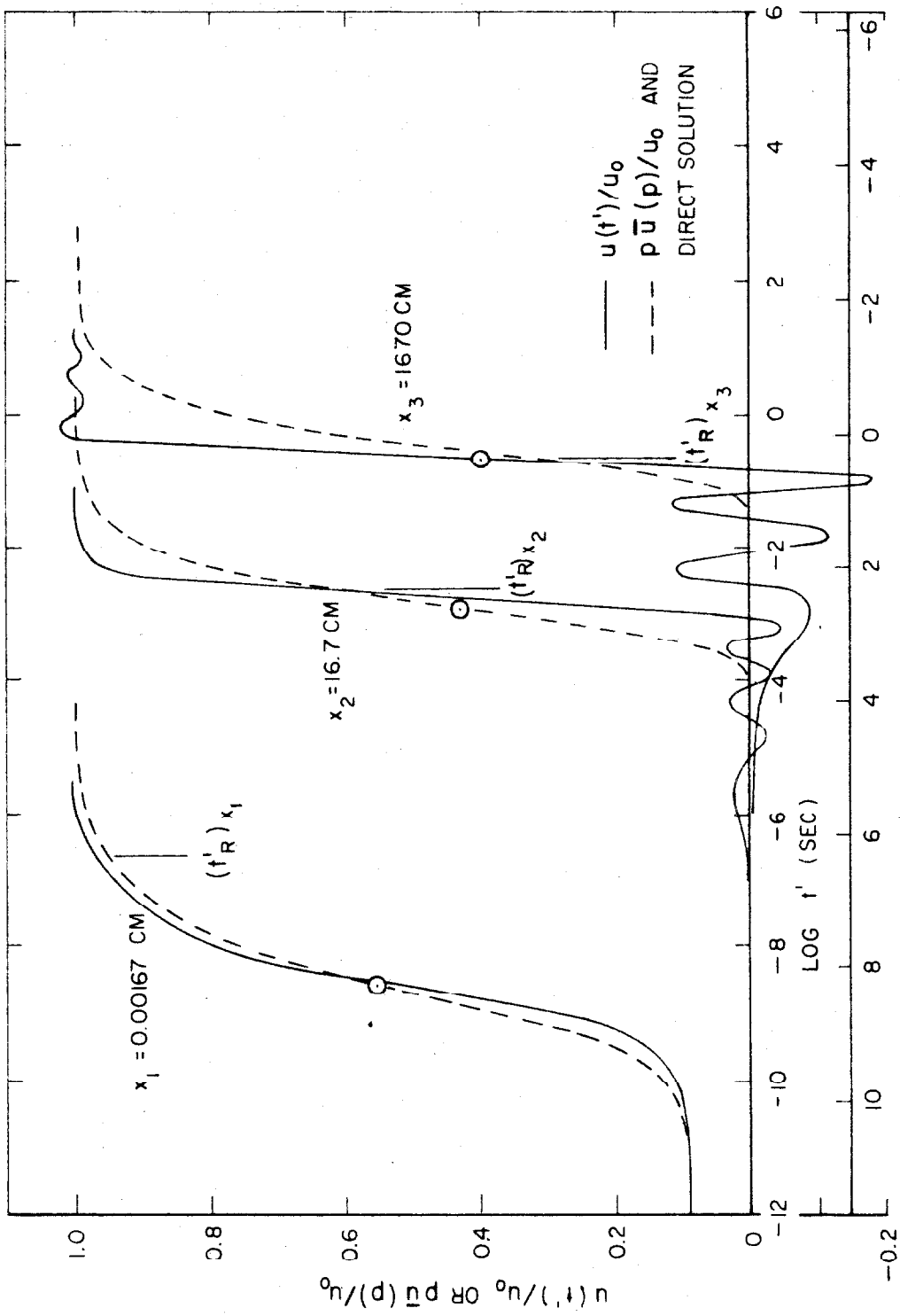

FIG. 4 RESPONSE OF POLYURETHANE ROD TO STEP DISPLACEMENT INPUT ; TEMPERATURE = 14°C; ⊙ DENOTES INFLECTION POINT

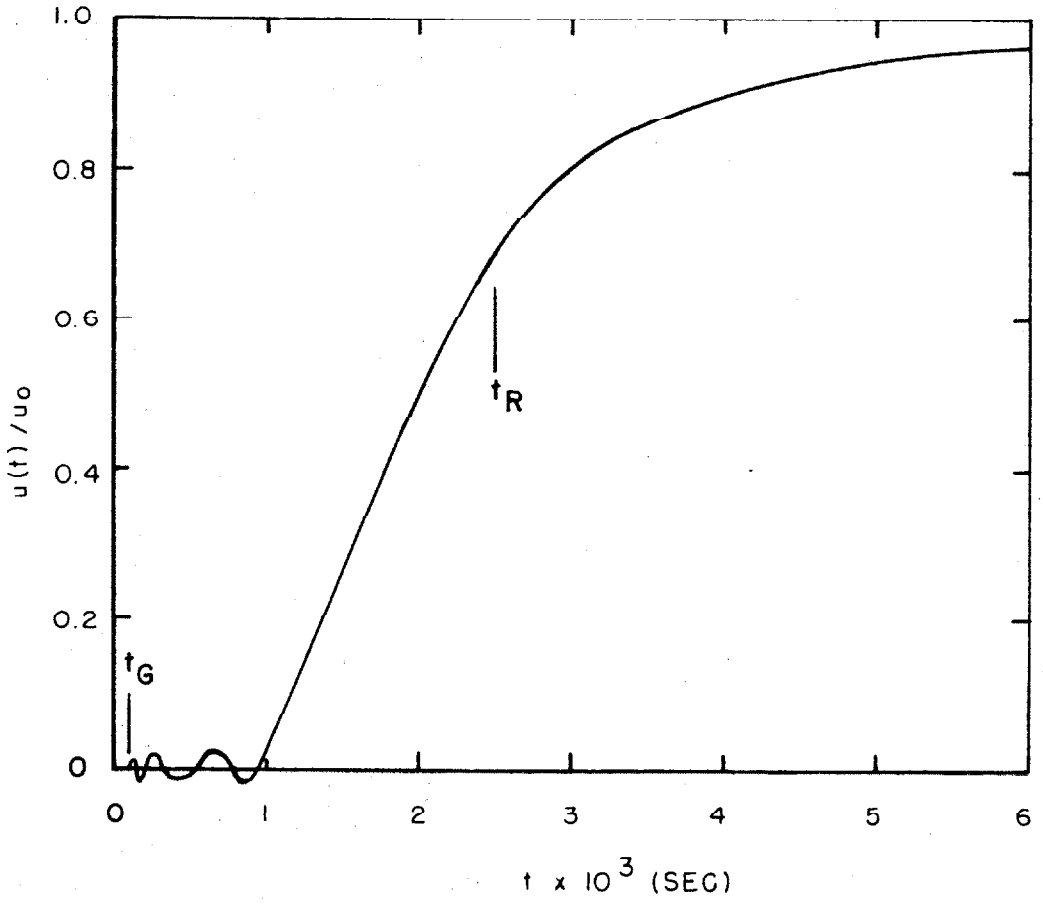

FIG. 5 TIME RESPONSE OF POLYURETHANE ROD TO STEP DISPLACEMENT INPUT AT x_2 = 16.7 CM; TEMP. = 14°C

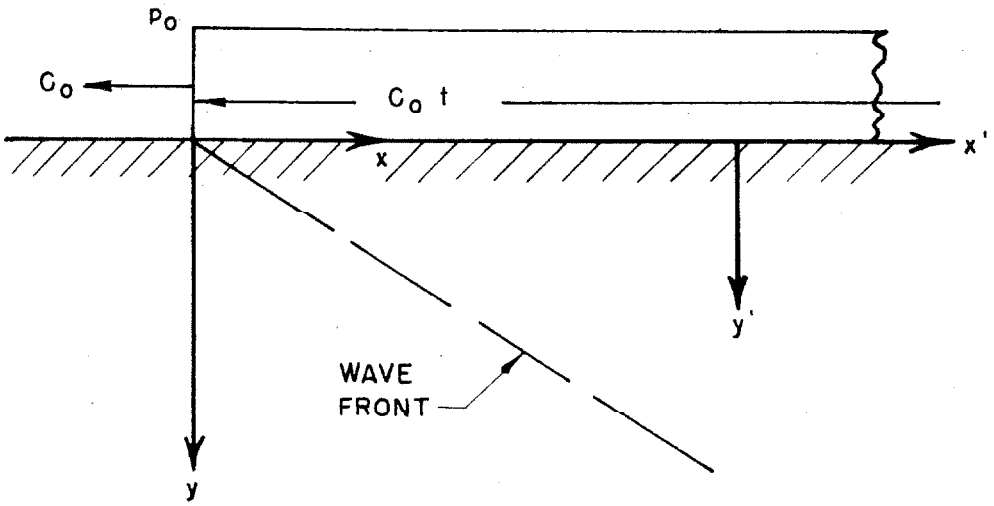

FIG.6 TWO - DIMENSIONAL SEMI - INFINITE GEOMETRY SUBJECTED TO STEADILY MOVING STEP PRESSURE LOAD ON THE BOUNDARY

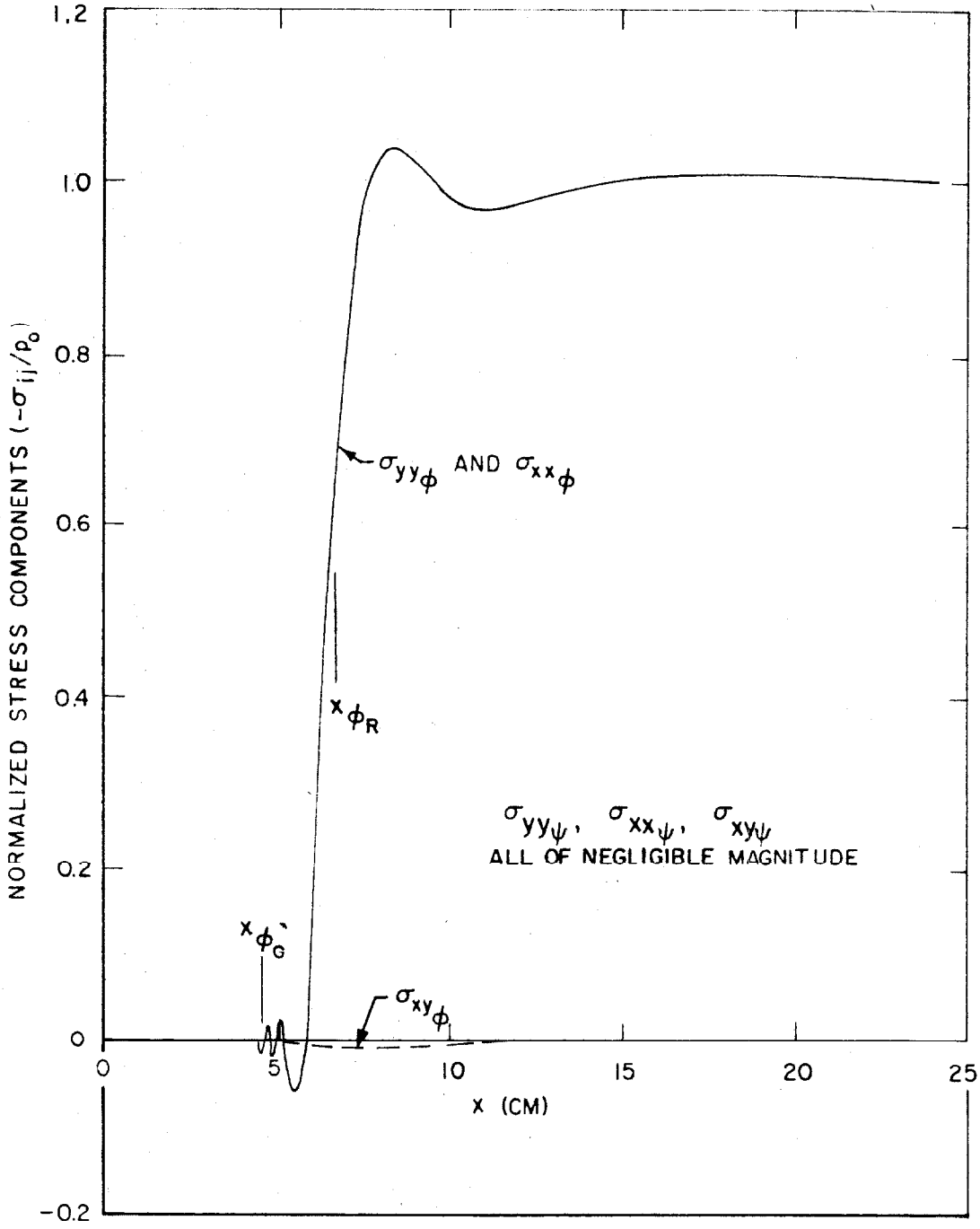

FIG. 7 TYPICAL STRESS COMPONENTS FOR POLYURETHANE HALF-SPACE UNDER MOVING STEP PRESSURE LOADING (p_o); $M_\phi = 1.5$, $y = 4$ CM

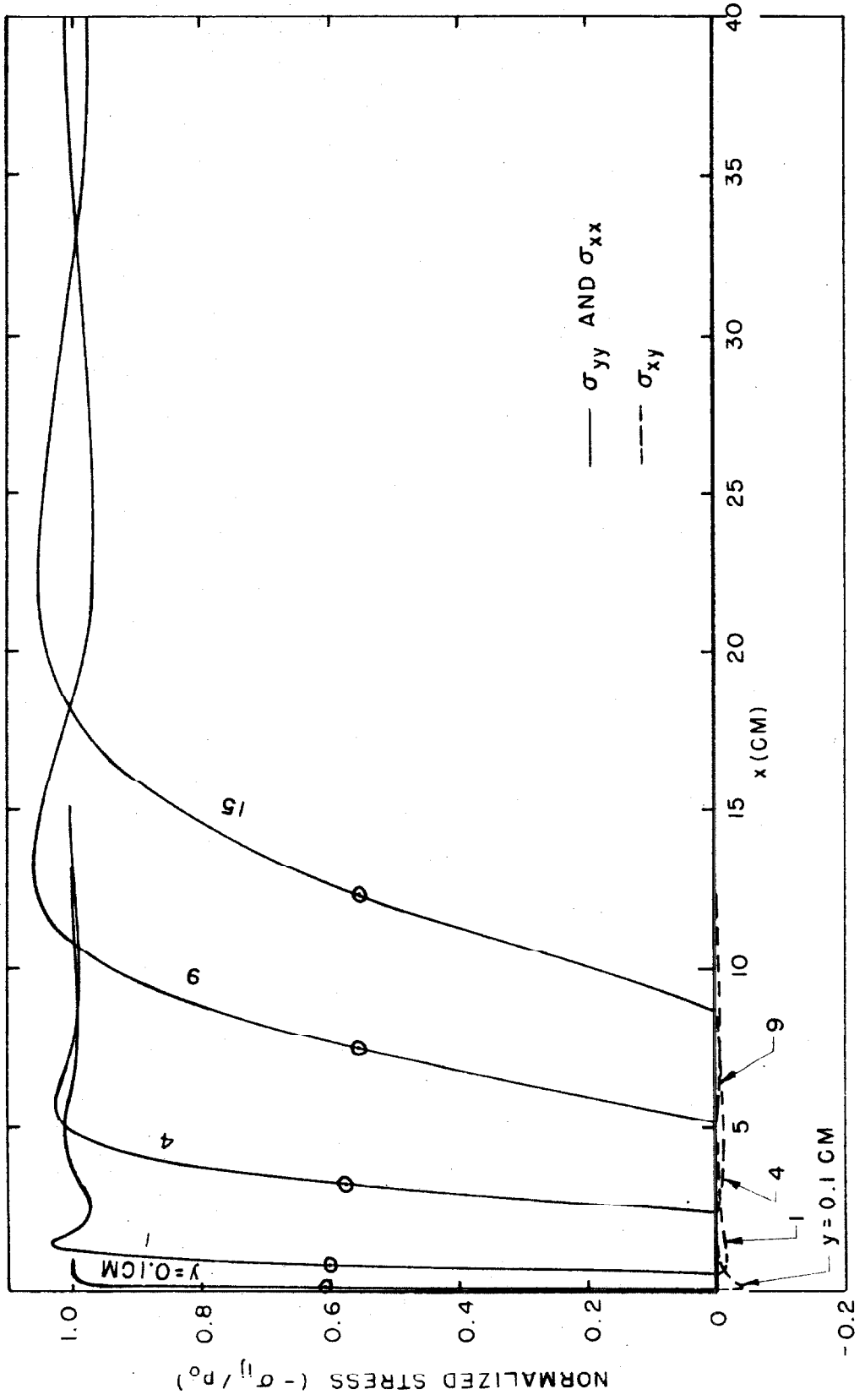

FIG.8 STRESS RESPONSE OF POLYURETHANE HALF-SPACE UNDER MOVING STEP PRESSURE LOADING (p_o); ⊙ DENOTES $x\phi_R$; (4) $M\phi = 1.01$

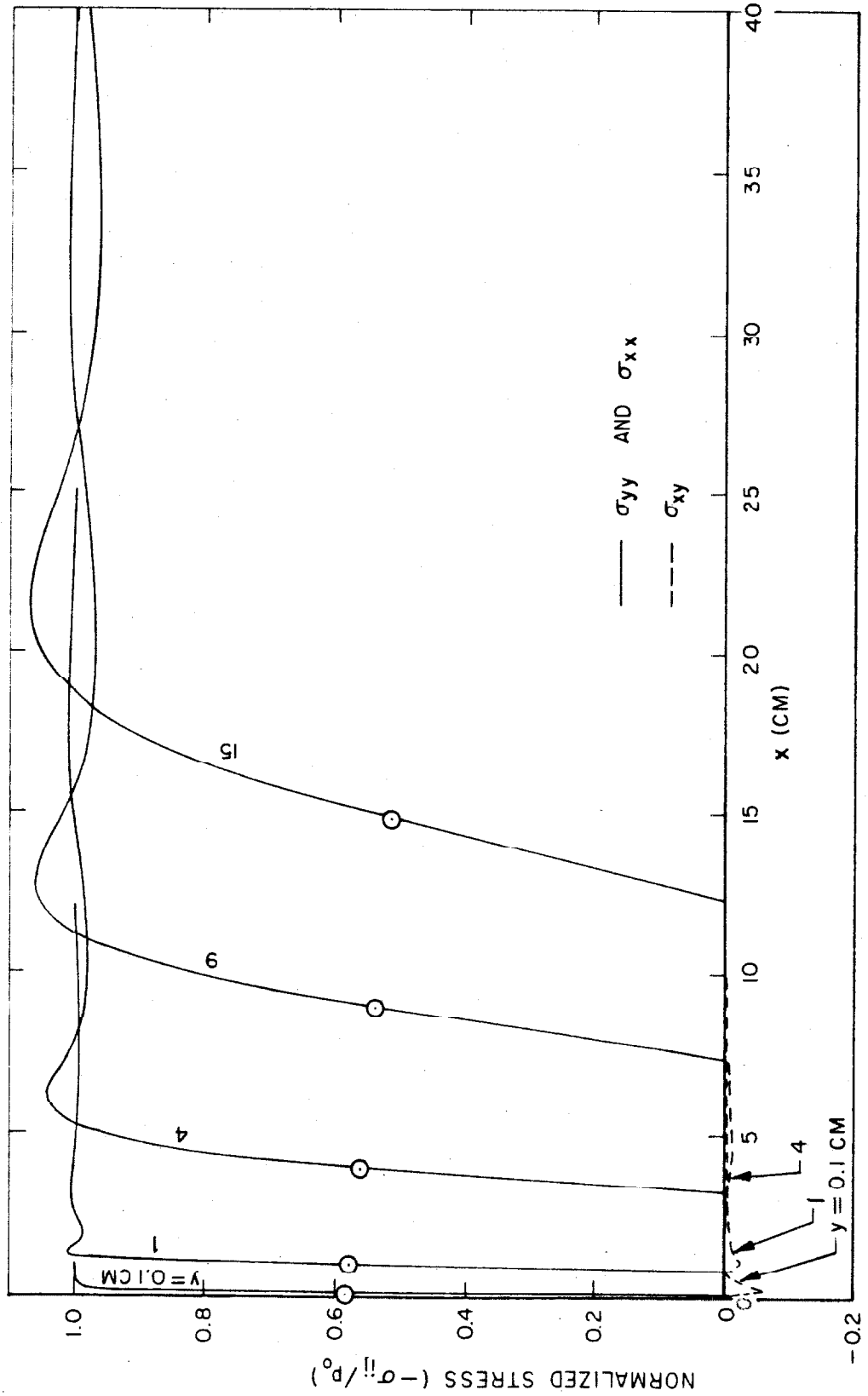

FIG. 8 (b) $M_\phi = 1.1$

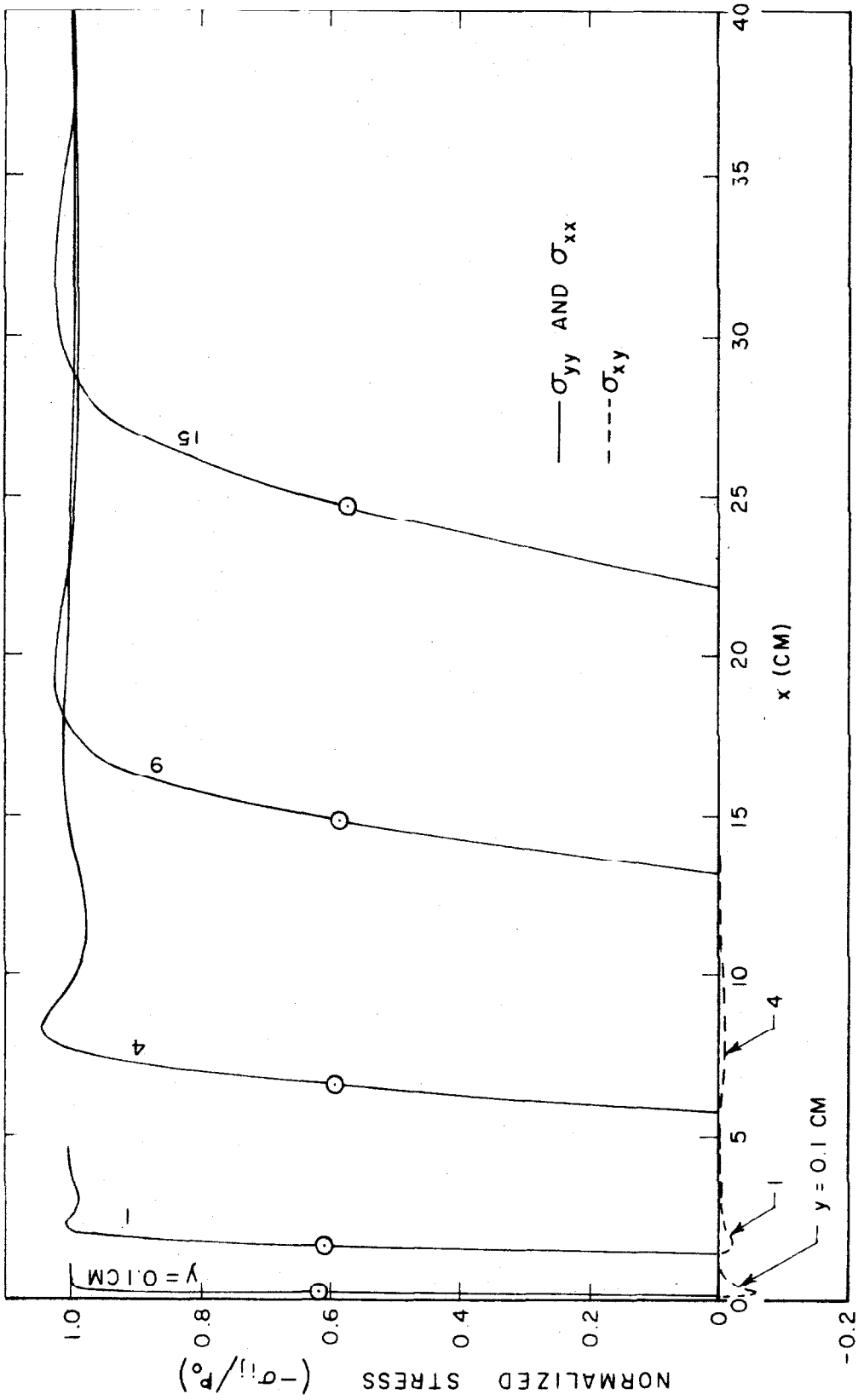

FIG. 8(c) $M_\phi = 1.5$

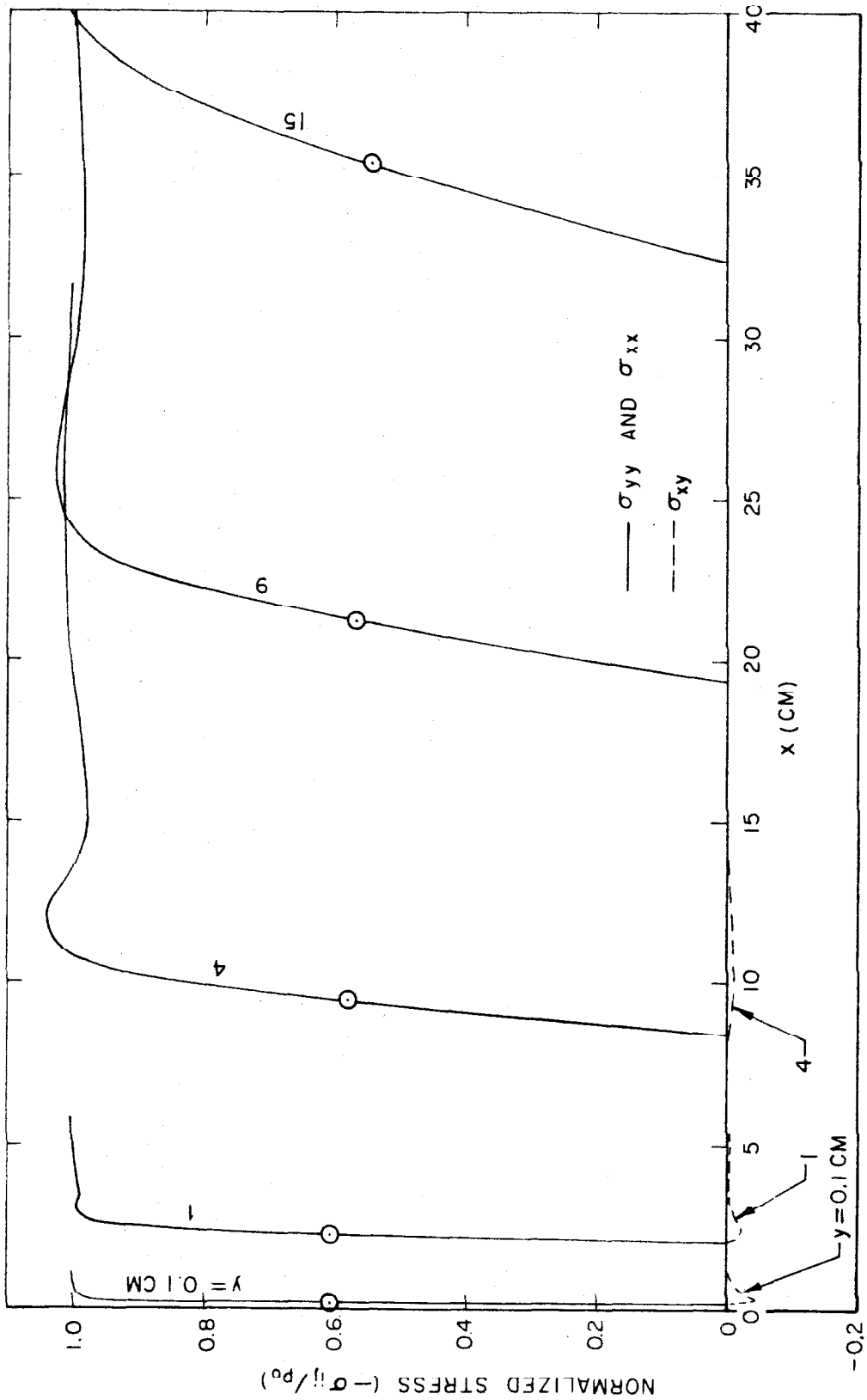

FIG. 8(d) $M_\phi = 2.0$

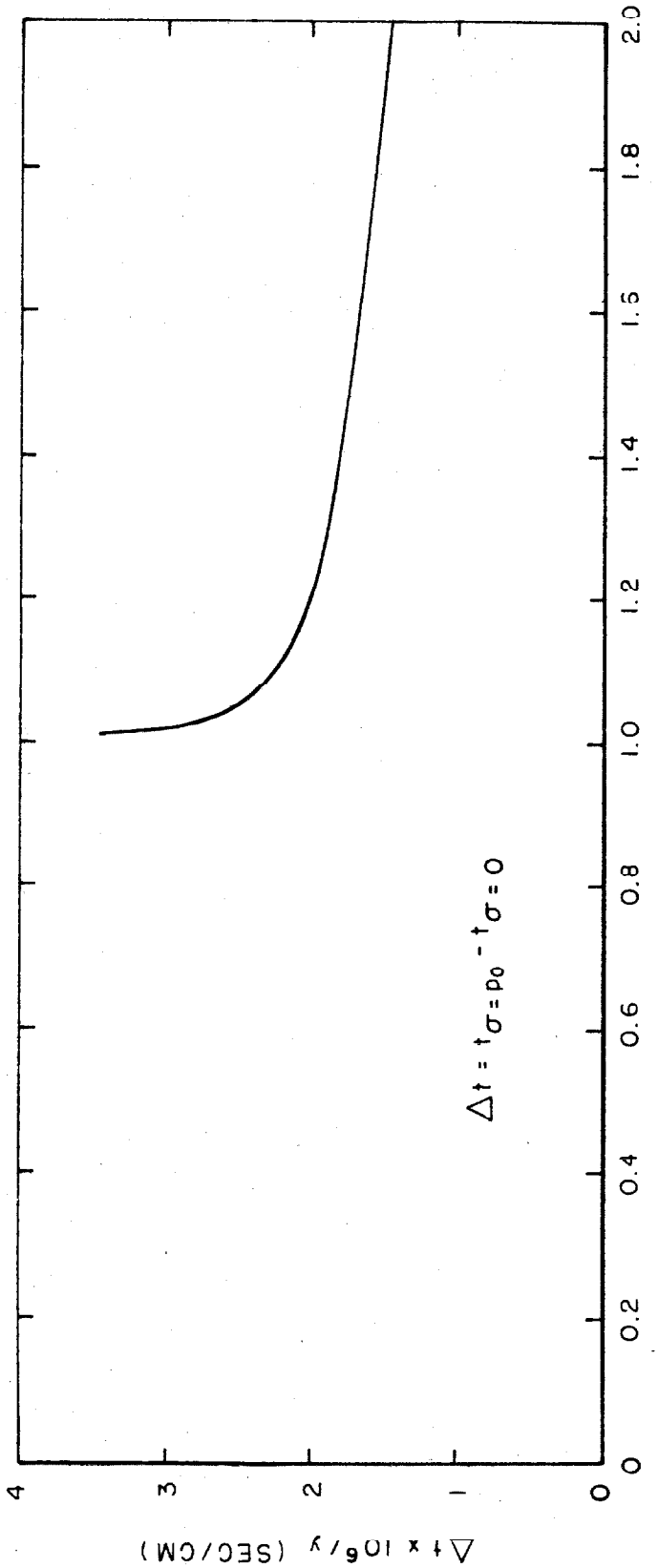

FIG.9 VARIATION OF STRESS RISE TIME FOR POLYURETHANE HALF-SPACE UNDER MOVING STEP PRESSURE LOADING (p_0)

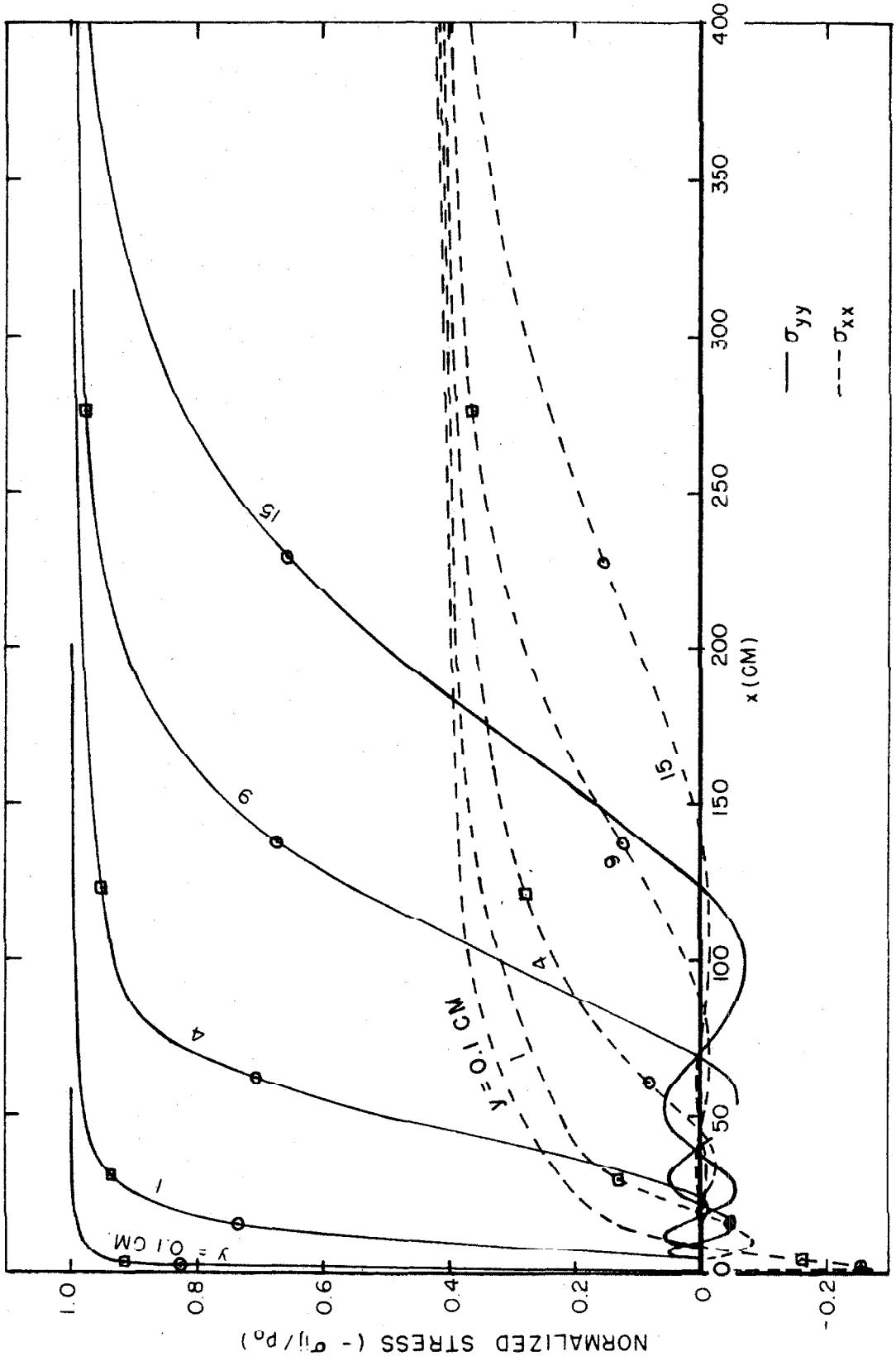

FIG. 10 STRESS RESPONSE OF THIN POLYURETHANE PLATE UNDER MOVING STEP PRESSURE LOADING (p_o); ○ DENOTES $\times\phi_R$, ⊡ DENOTES $\times\psi_R$, (a) $M\phi = 1.01$

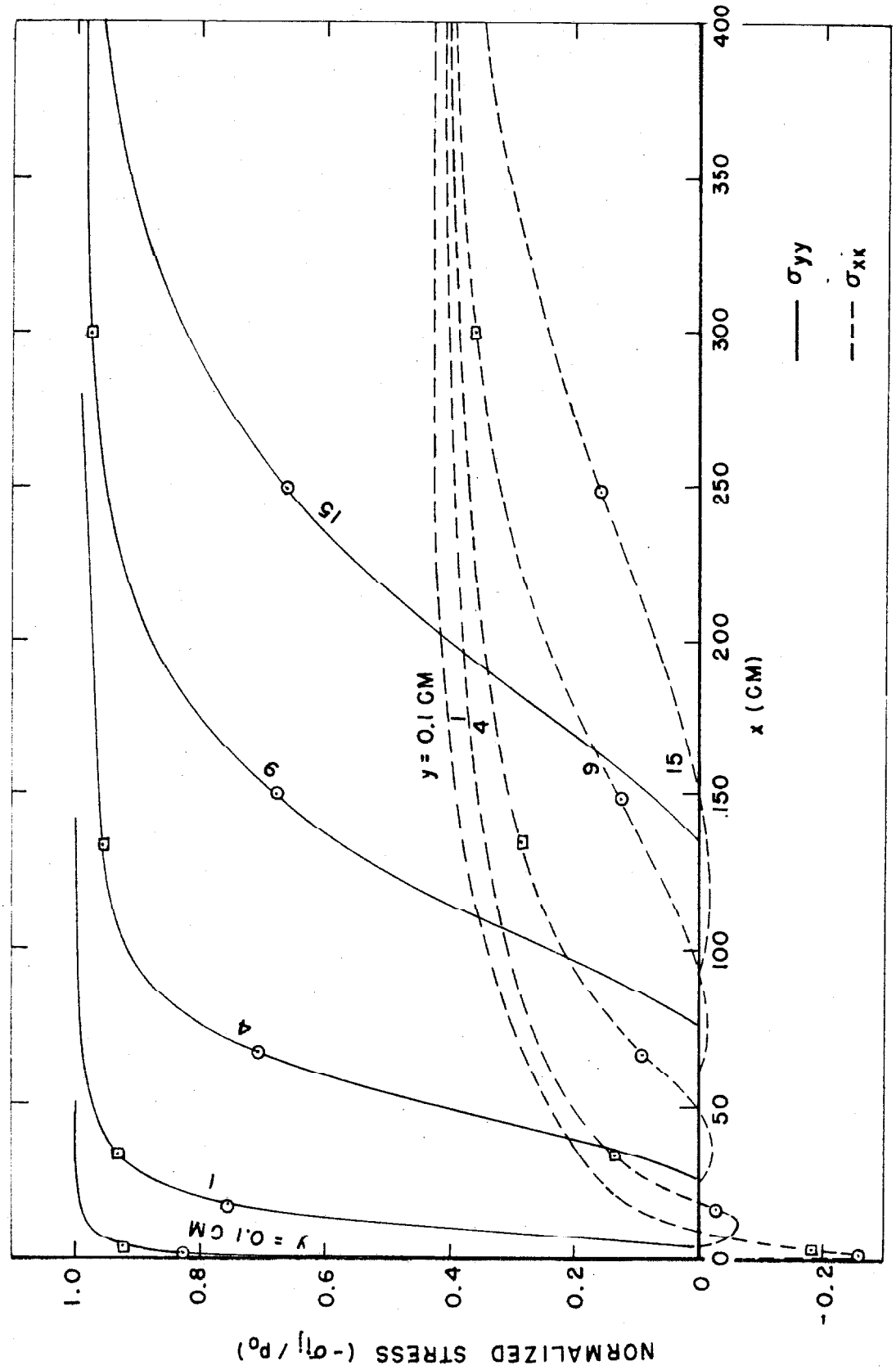

FIG. 10(b) $M_\phi = 1.1$

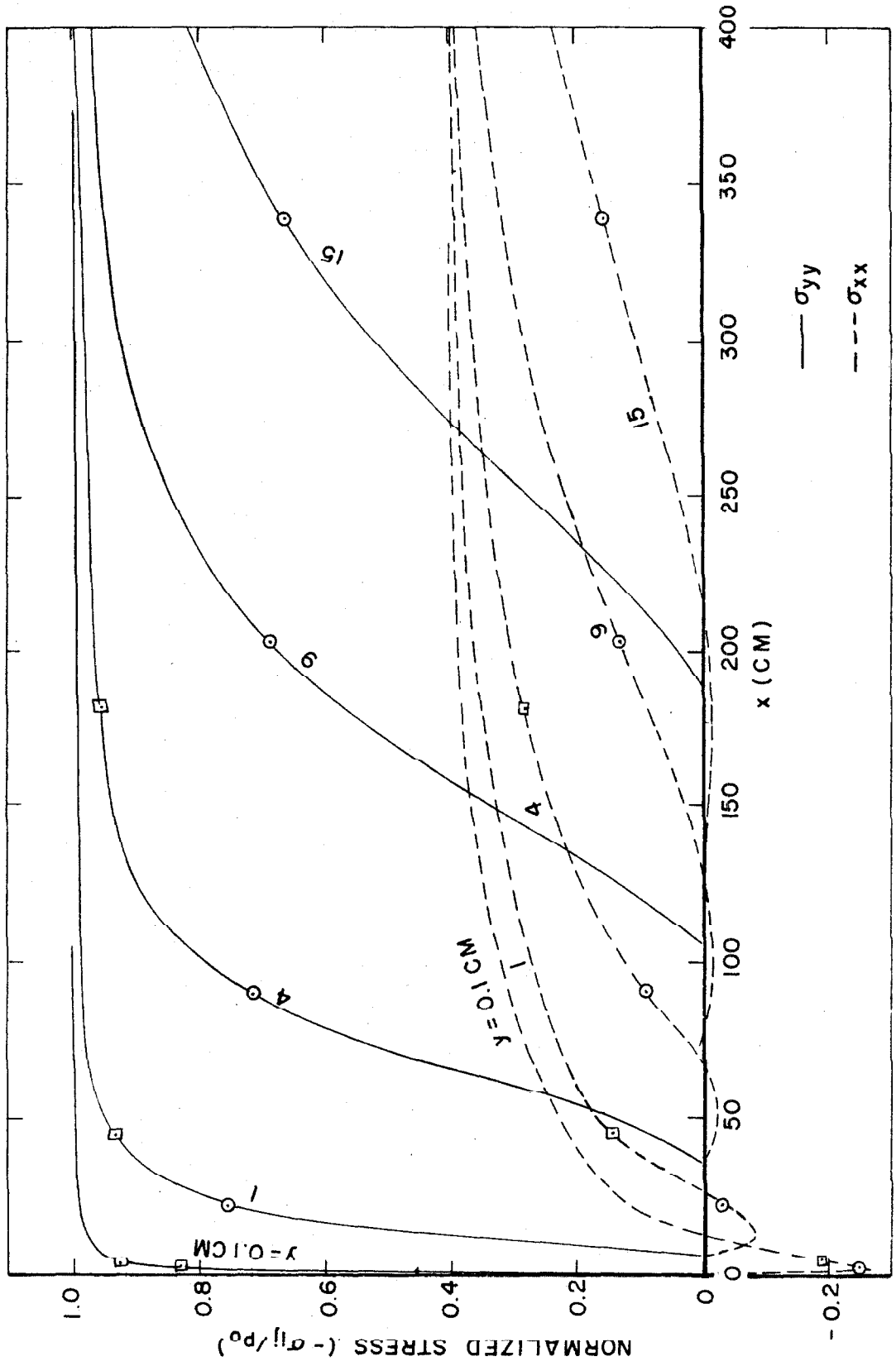
NORMALIZED STRESS (- σij/po)
x (CM)
σyy
σxx
y=0.1 CM
1
4
9
15
0
50
100
150
200
250
300
350
400
0.2
0.4
0.6
0.8
1.0
-0.2

FIG.10(c) Mϕ = 1.5

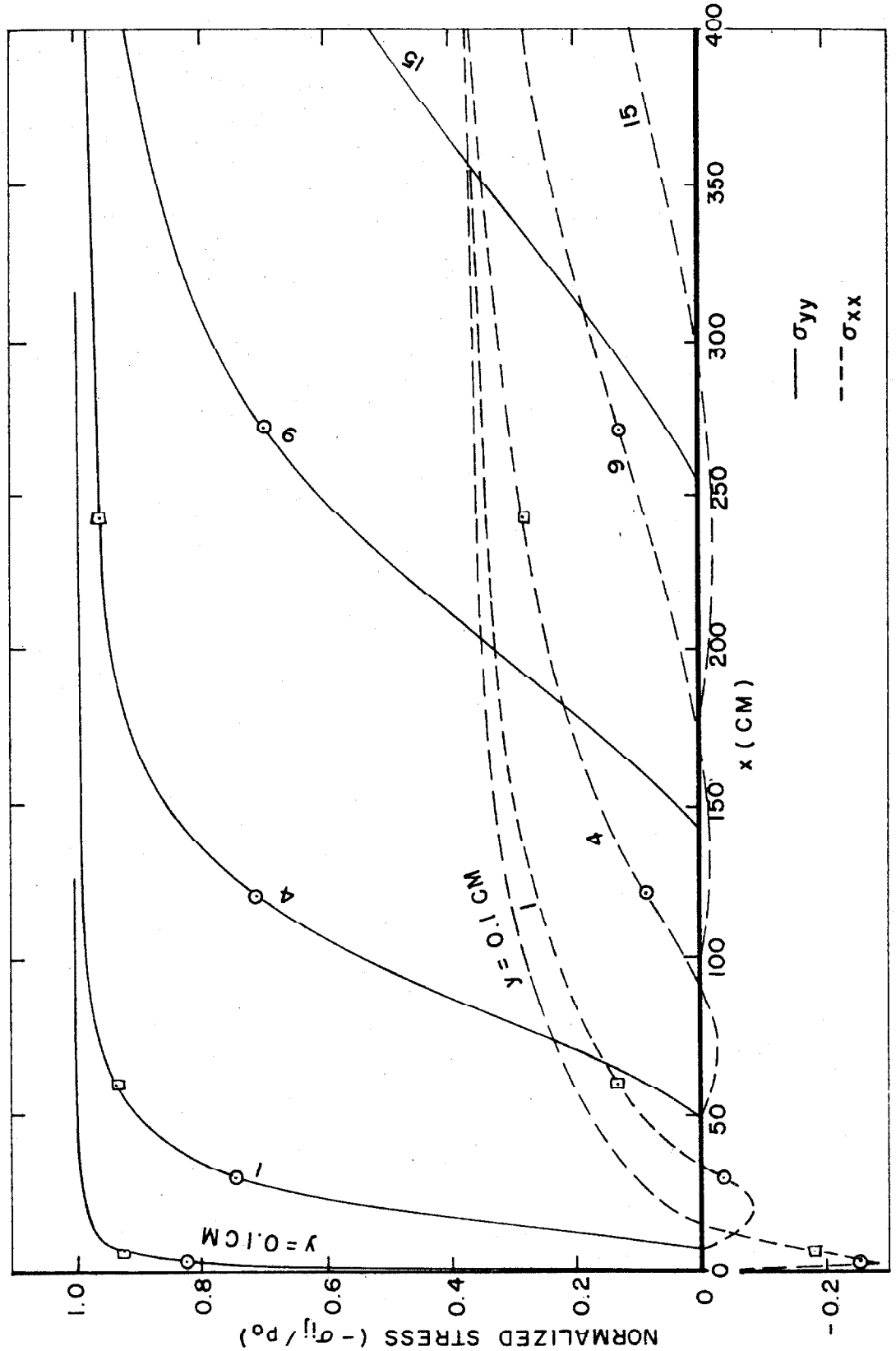

FIG.10 (d) $M_\phi = 2.0$

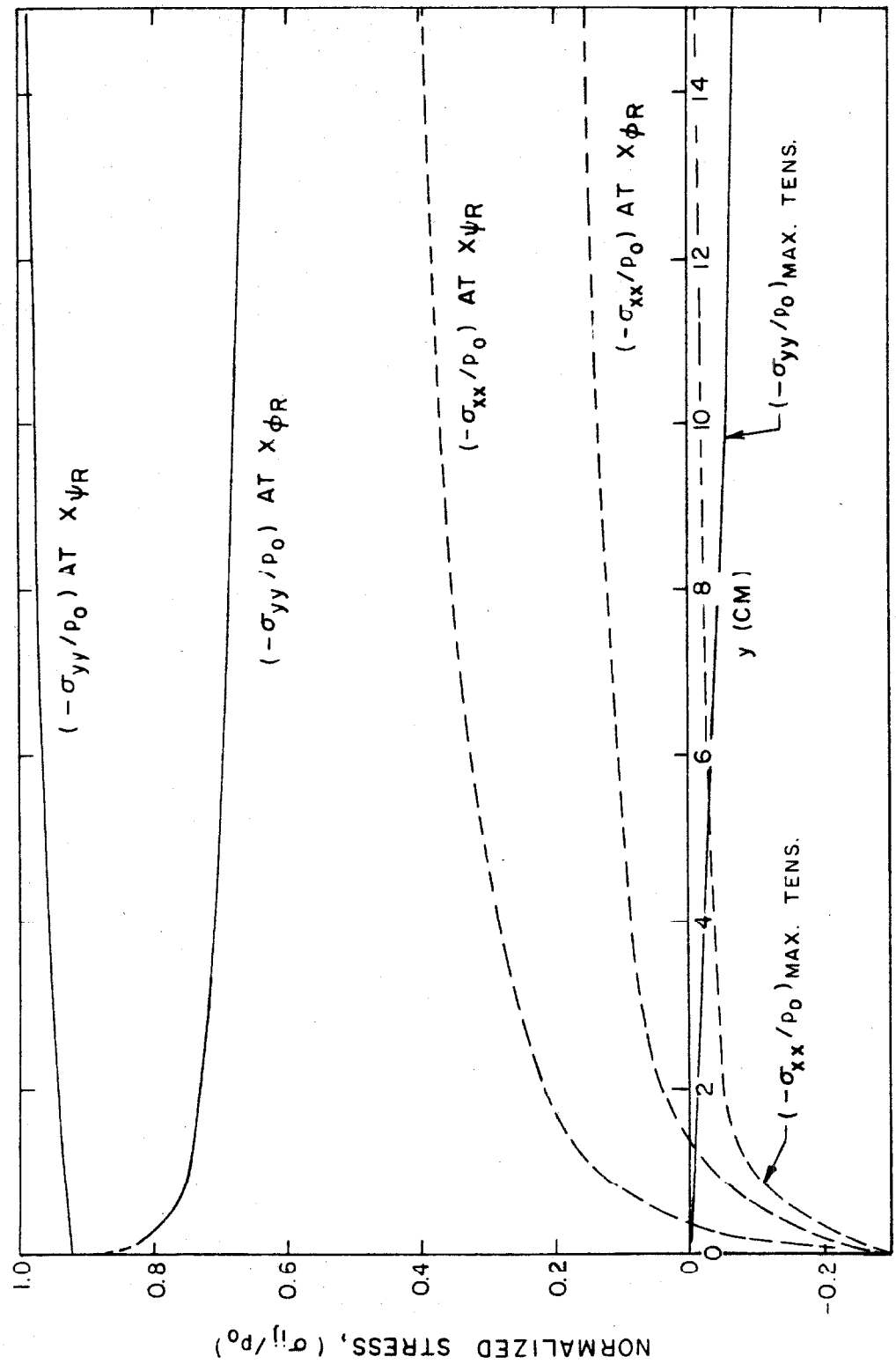

FIG. 11 STRESSES AT RUBBERY ARRIVAL POSITIONS AND MAXIMUM TENSILE STRESS AS A FUNCTION OF DEPTH IN THIN POLYURETHANE PLATE UNDER SUPERSONICALLY MOVING STEP PRESSURE LOADING (p_o)

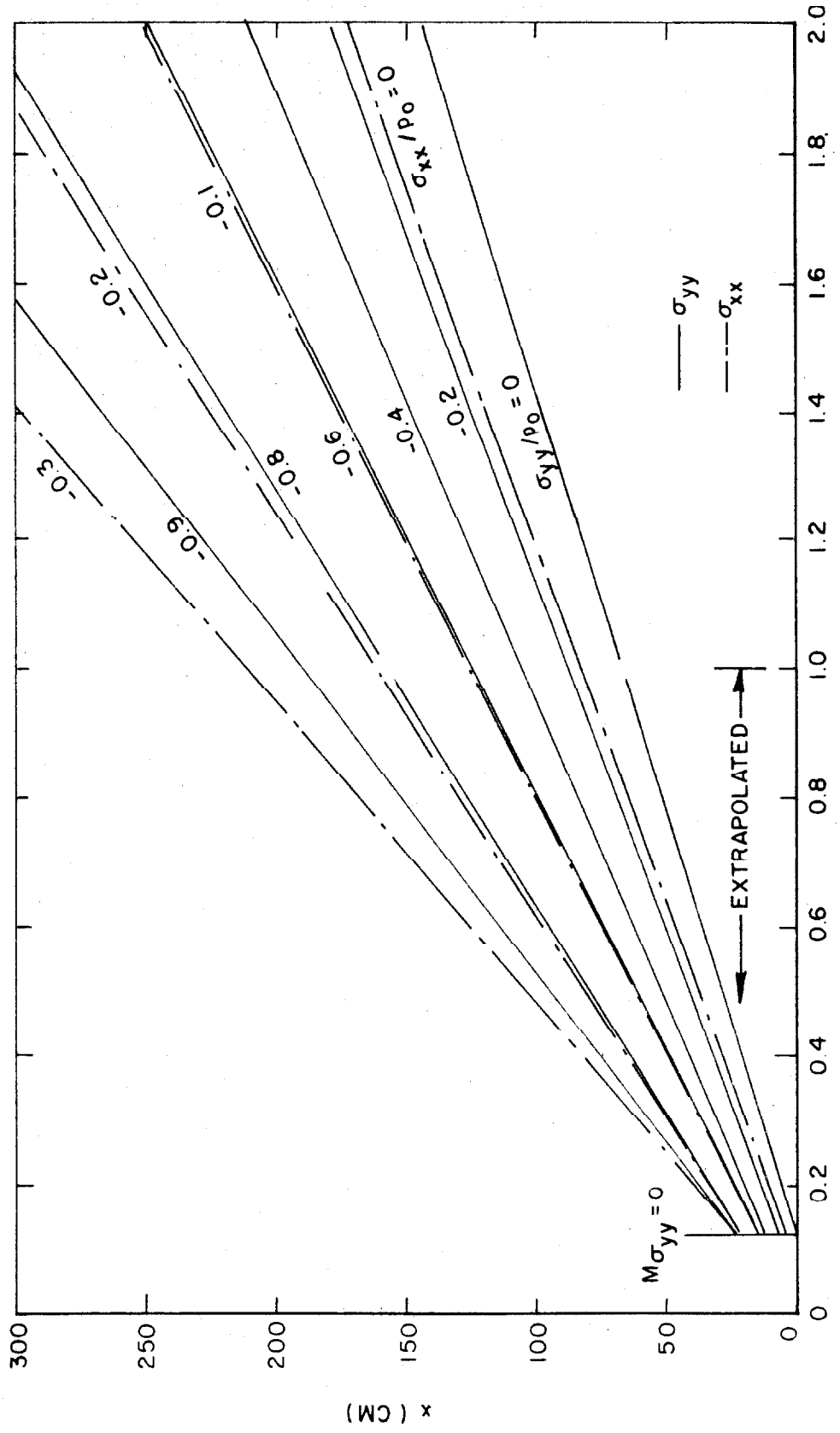

FIG.12 SPATIAL VARIATION OF STRESS AS A FUNCTION OF M_ϕ IN A THIN POLYURETHANE PLATE UNDER MOVING STEP PRESSURE LOADING (p_o) ; y = 9 CM

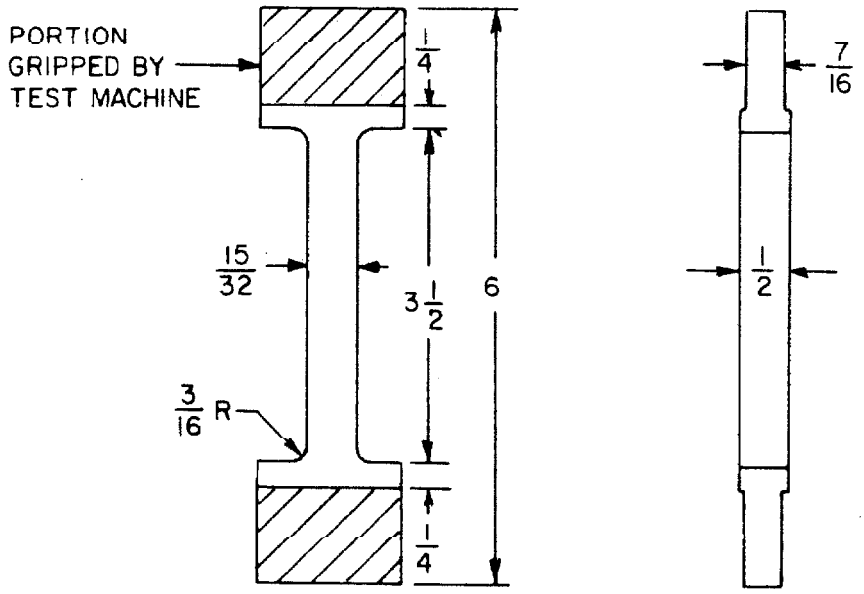

FIG. 13 TENSILE SPECIMEN OF HYSOL 8705 MATERIAL FOR INSTRON TESTING

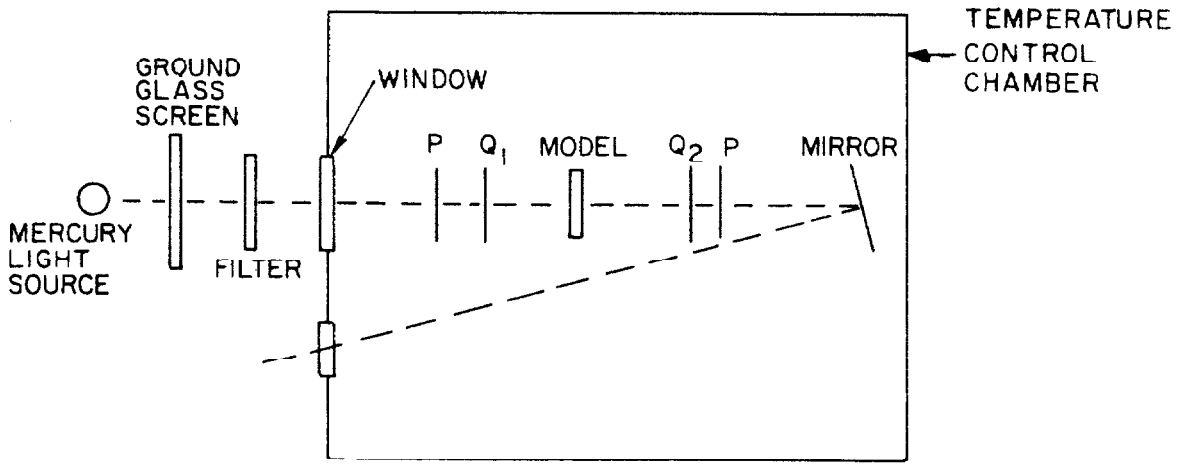

FIG. 14 SCHEMATIC DIAGRAM OF INSTRON TEST MACHINE AND PHOTOELASTIC CALIBRATION APPARATUS

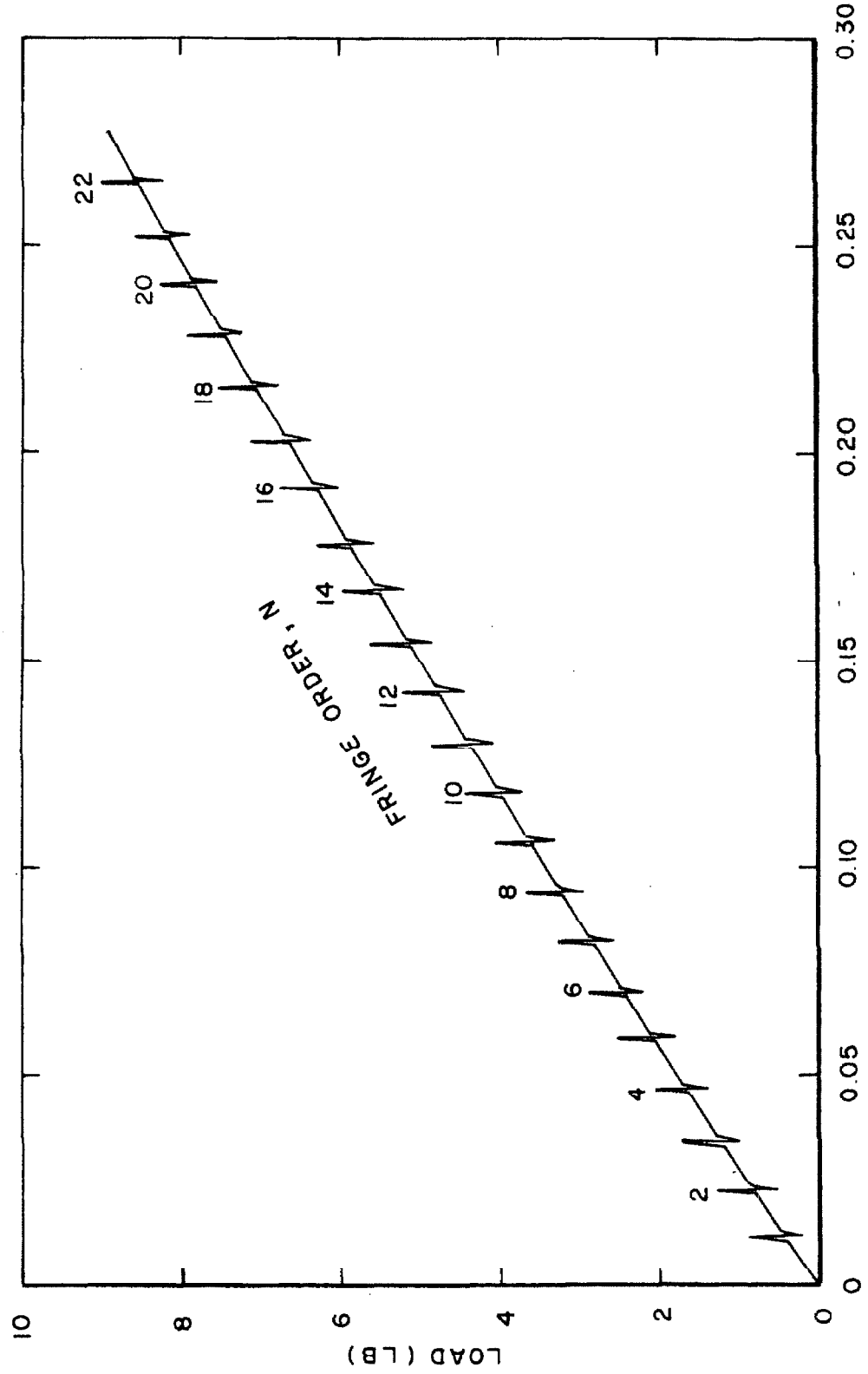

FIG.15 TYPICAL LOAD-ELONGATION-FRINGE ORDER RECORD FROM INSTRON TEST OF HYSOL 8705 ; T = 263° K, ELONGATION RATE = 0.2 IN/MIN

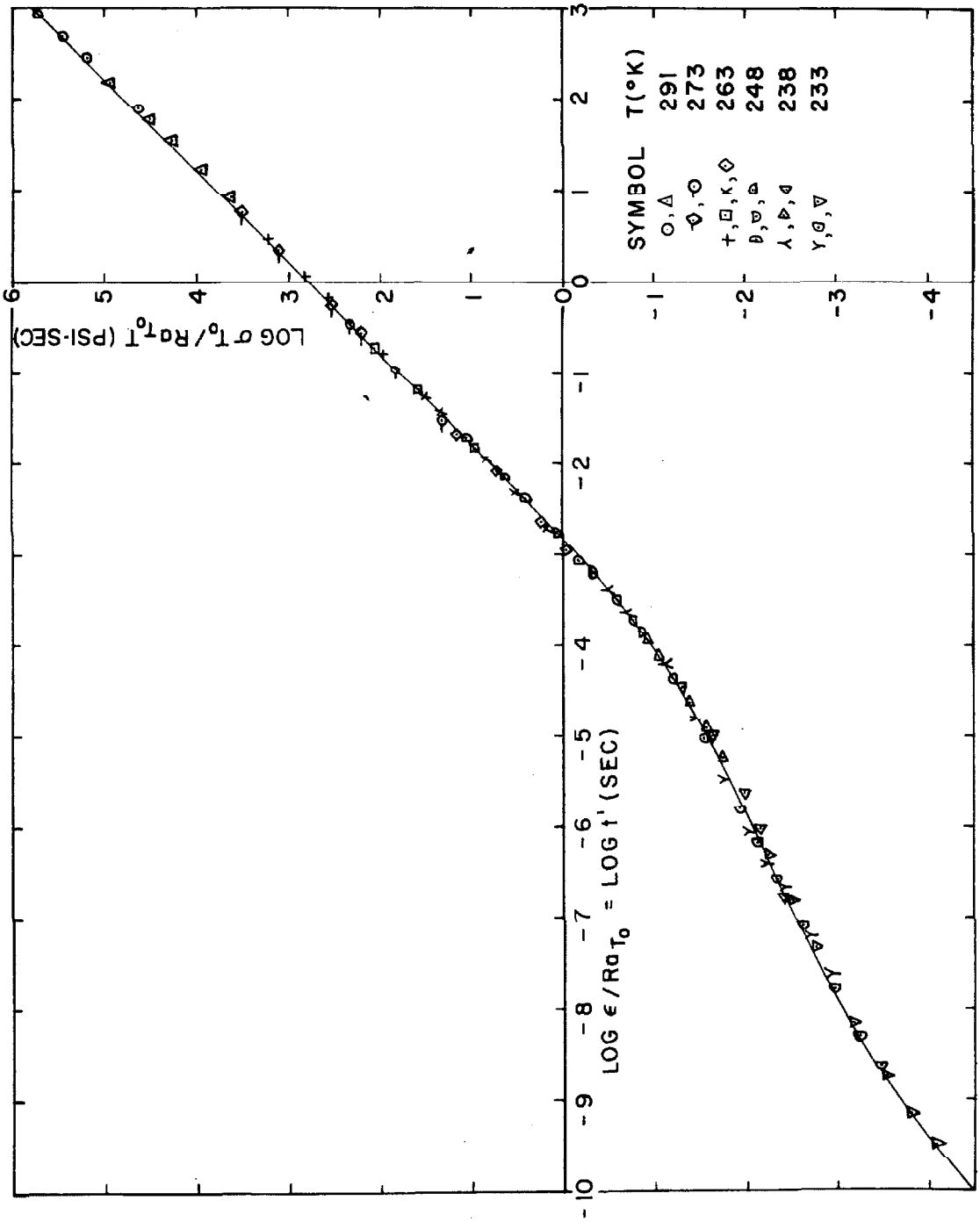

FIG.16 MASTER CURVE OF REDUCED STRESS AND STRAIN FOR CONSTANT STRAIN RATE TEST OF HYSOL 8705 MATERIAL; $T_0 = 291°K$

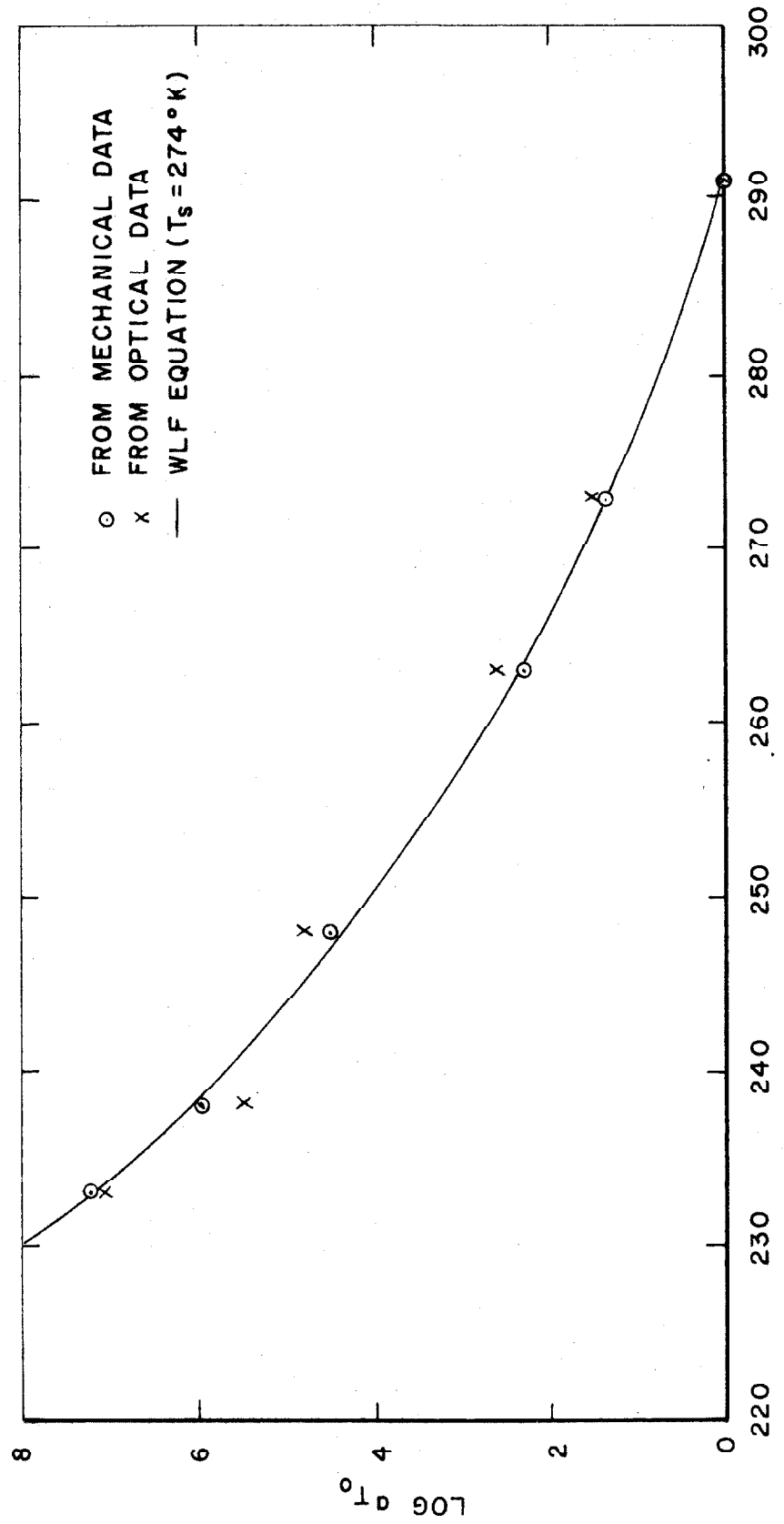

FIG. 17 TIME-TEMPERATURE SHIFT FACTOR FOR HYSOL 8705 MATERIAL FROM CONSTANT STRAIN RATE TEST; $T_o = 291°K$

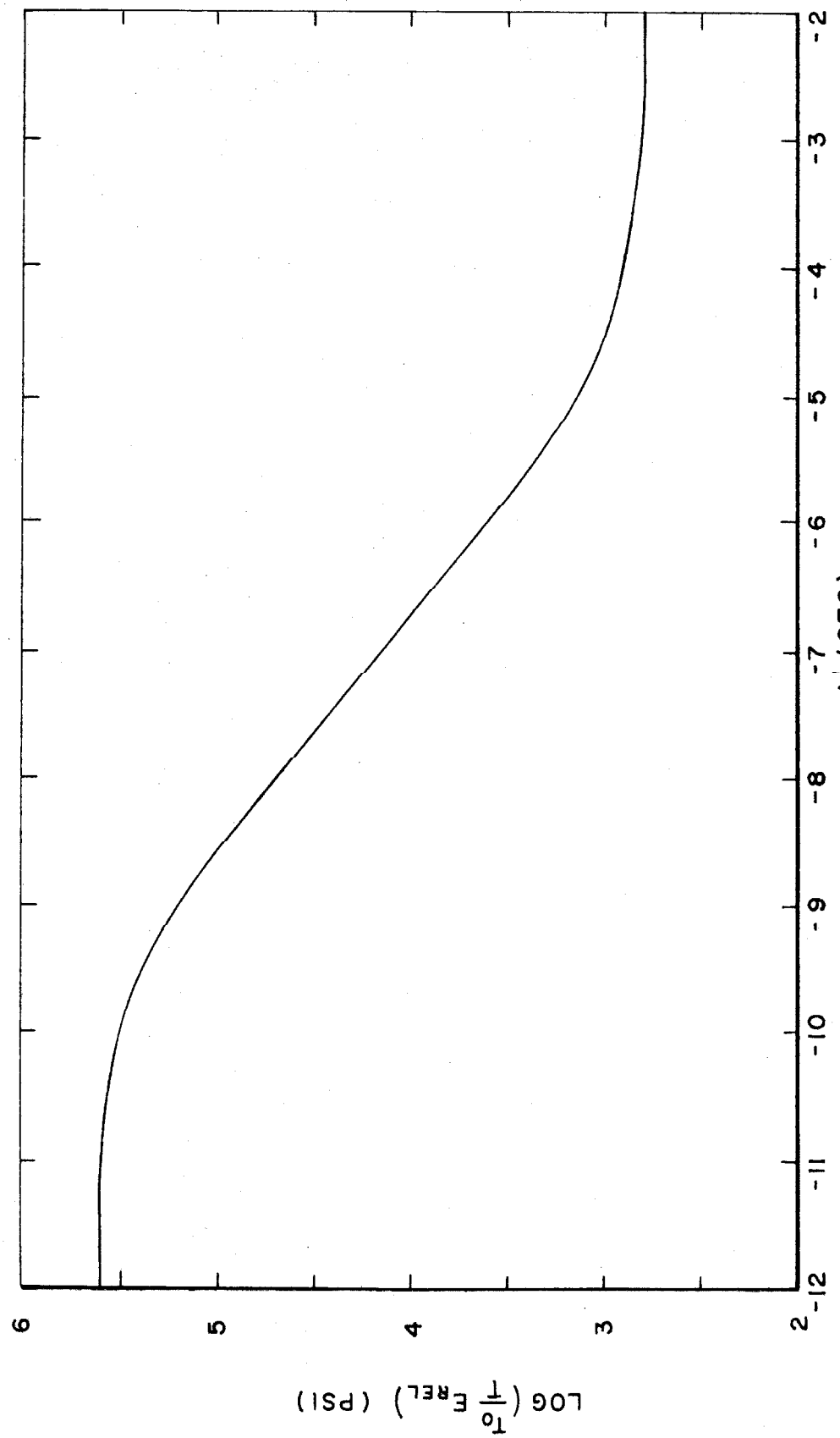

FIG.18 TENSILE RELAXATION MODULUS AS A FUNCTION OF REDUCED TIME FOR HYSOL 8705 MATERIAL; $T_o = 291°K$

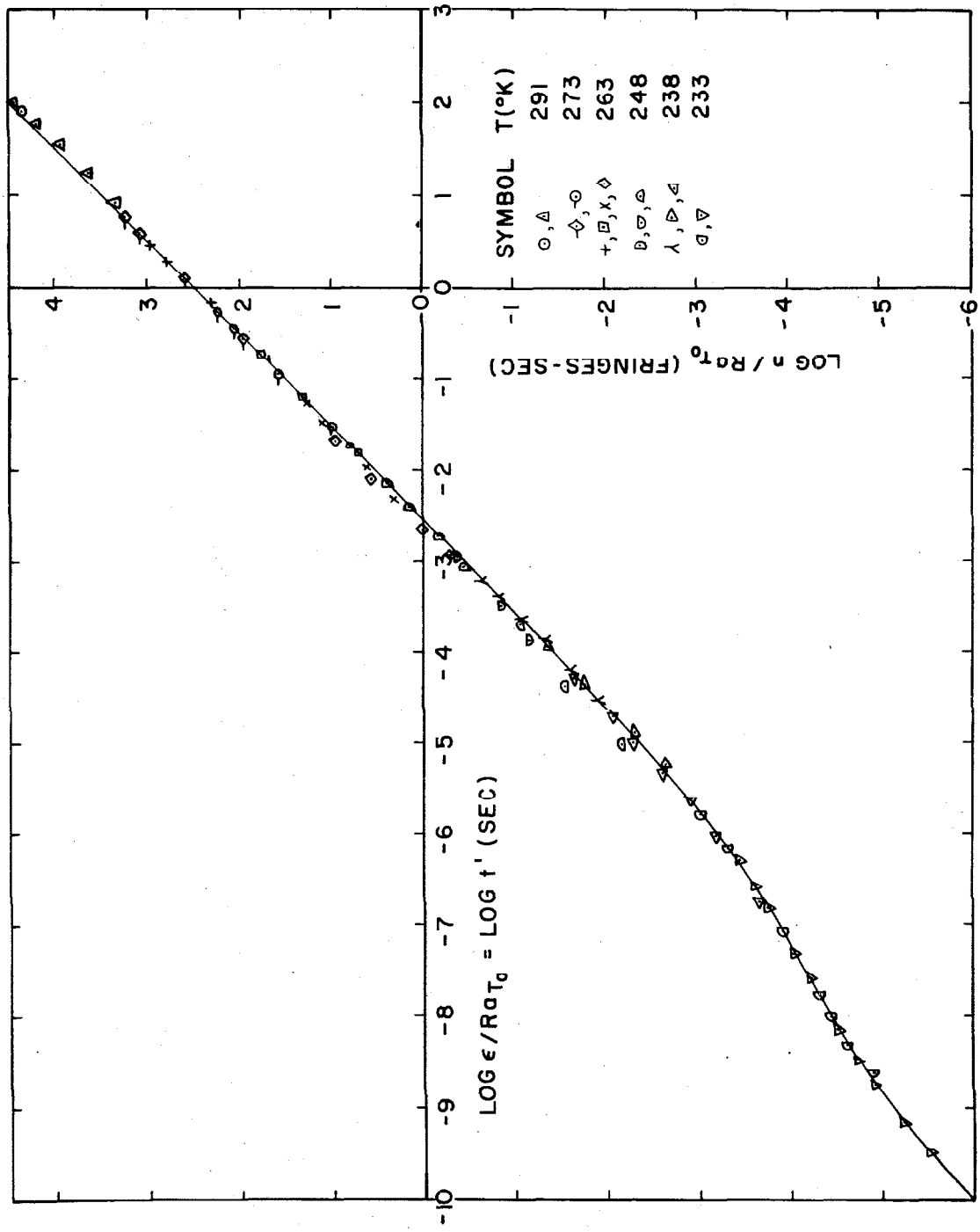

FIG. 19 MASTER CURVE OF REDUCED BIREFRIGENCE AND STRAIN FOR CONSTANT STRAIN RATE TEST OF HYSOL 8705 MATERIAL; T_o = 291° K

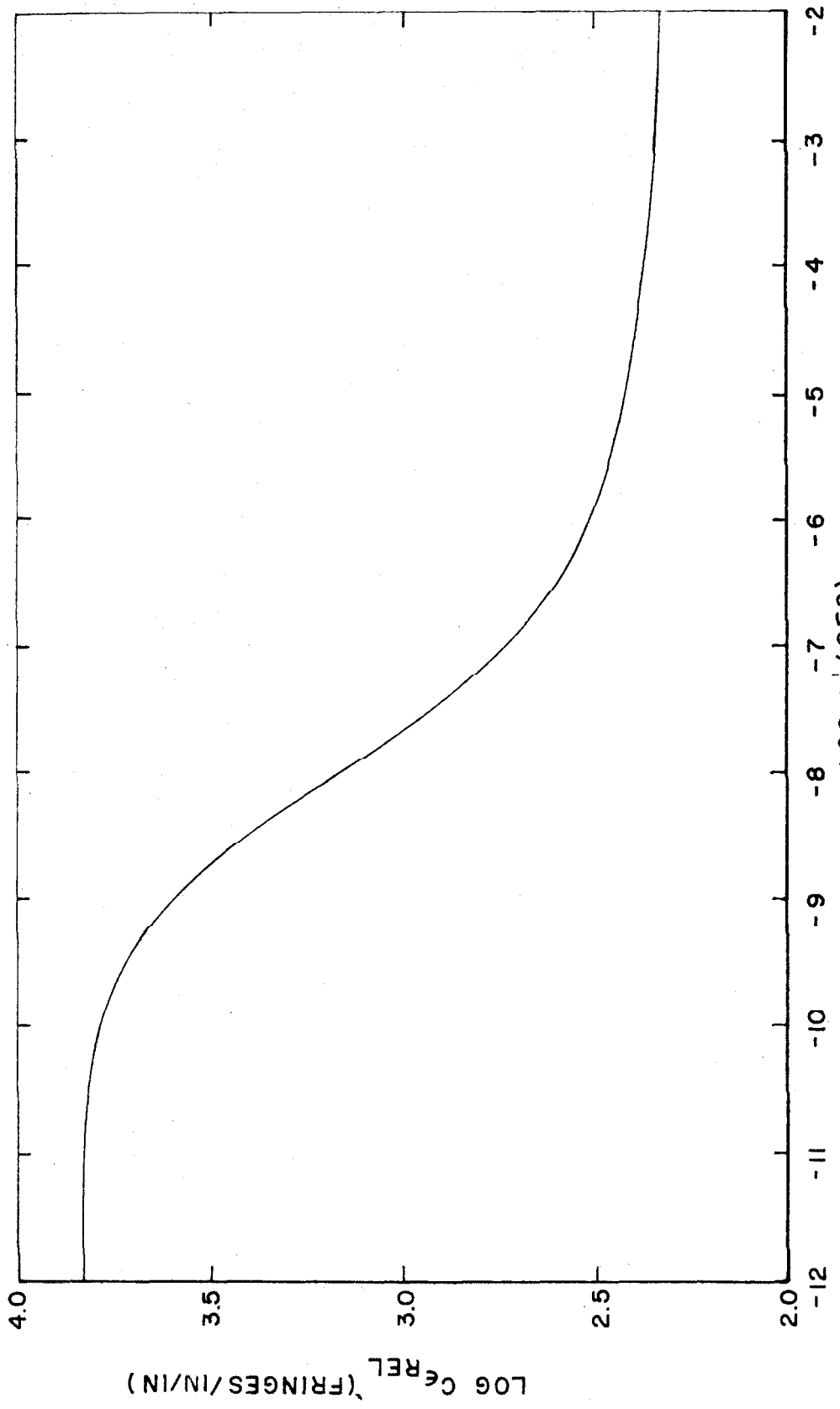

FIG.20 RELAXATION BIREFRINGENCE-STRAIN COEFFICIENT AS A FUNCTION OF REDUCED TIME FOR HYSOL 8705 MATERIAL; h = 1/2 INCH; T_o = 291°K

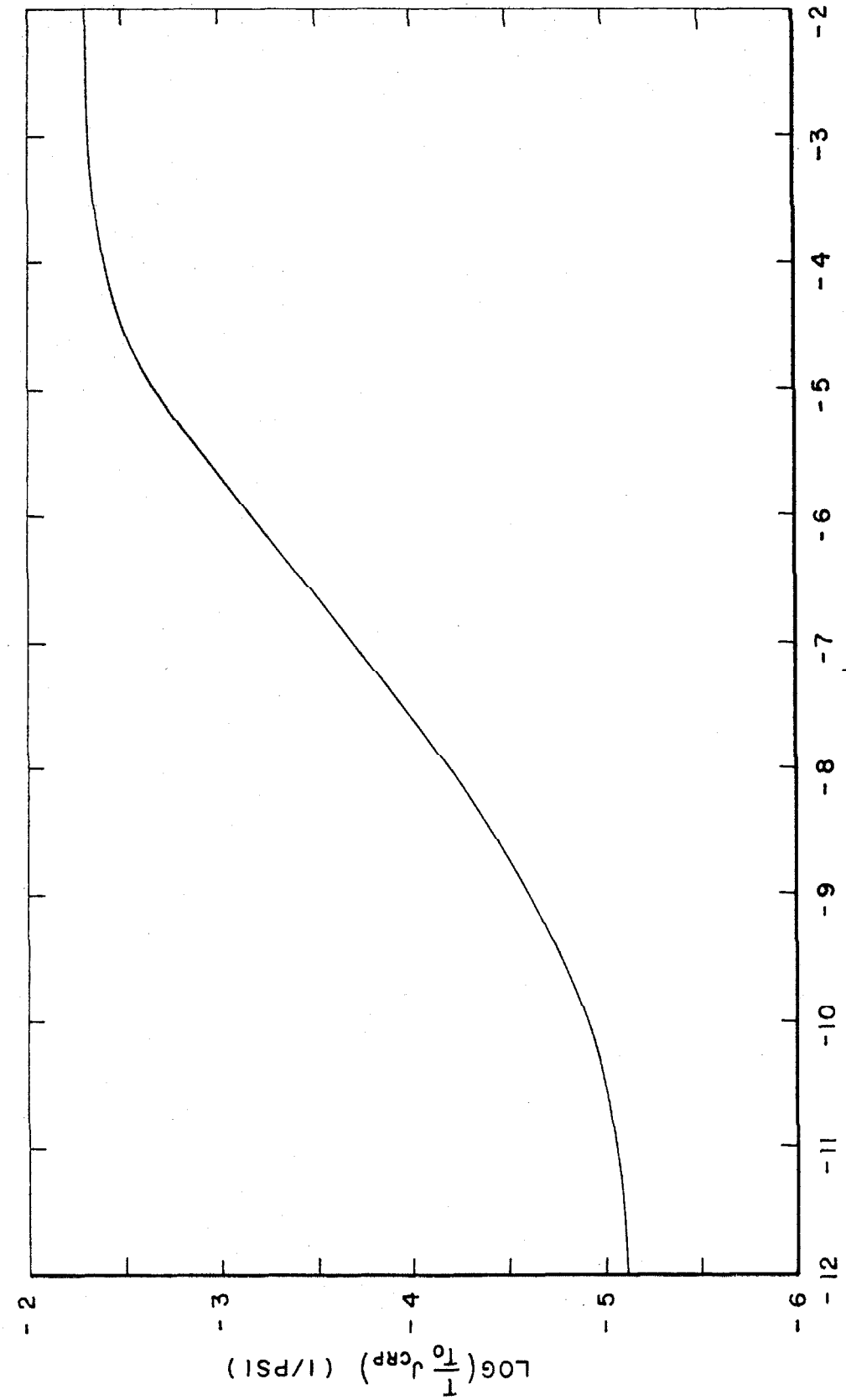

FIG. 21 SHEAR CREEP COMPLIANCE AS A FUNCTION OF REDUCED TIME FOR HYSOL 8705 MATERIAL ; $T_o = 291°K$

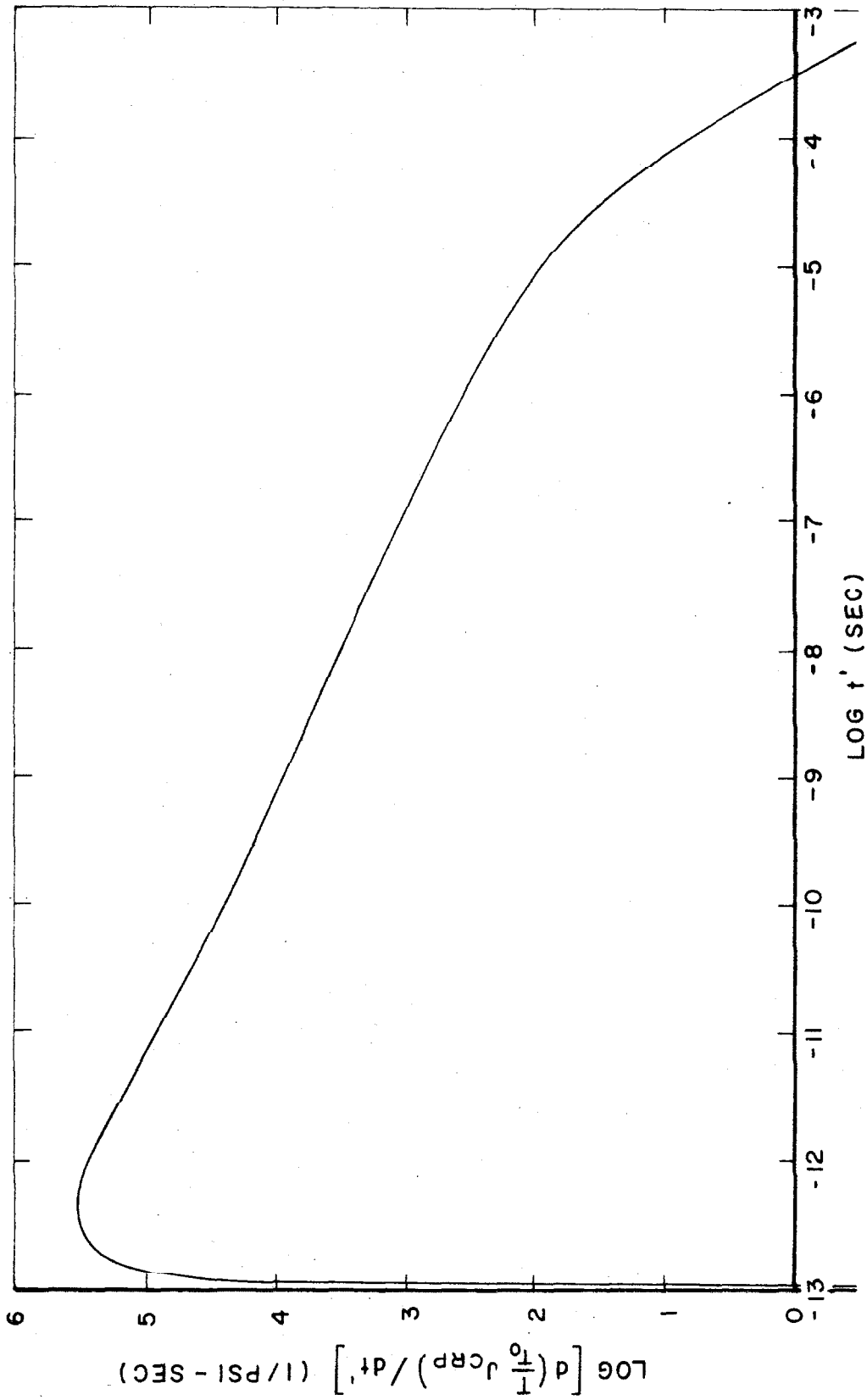

FIG. 22 SLOPE OF SHEAR CREEP COMPLIANCE VS. REDUCED TIME CURVE FOR HYSOL 8705 MATERIAL; T_0 = 291° K

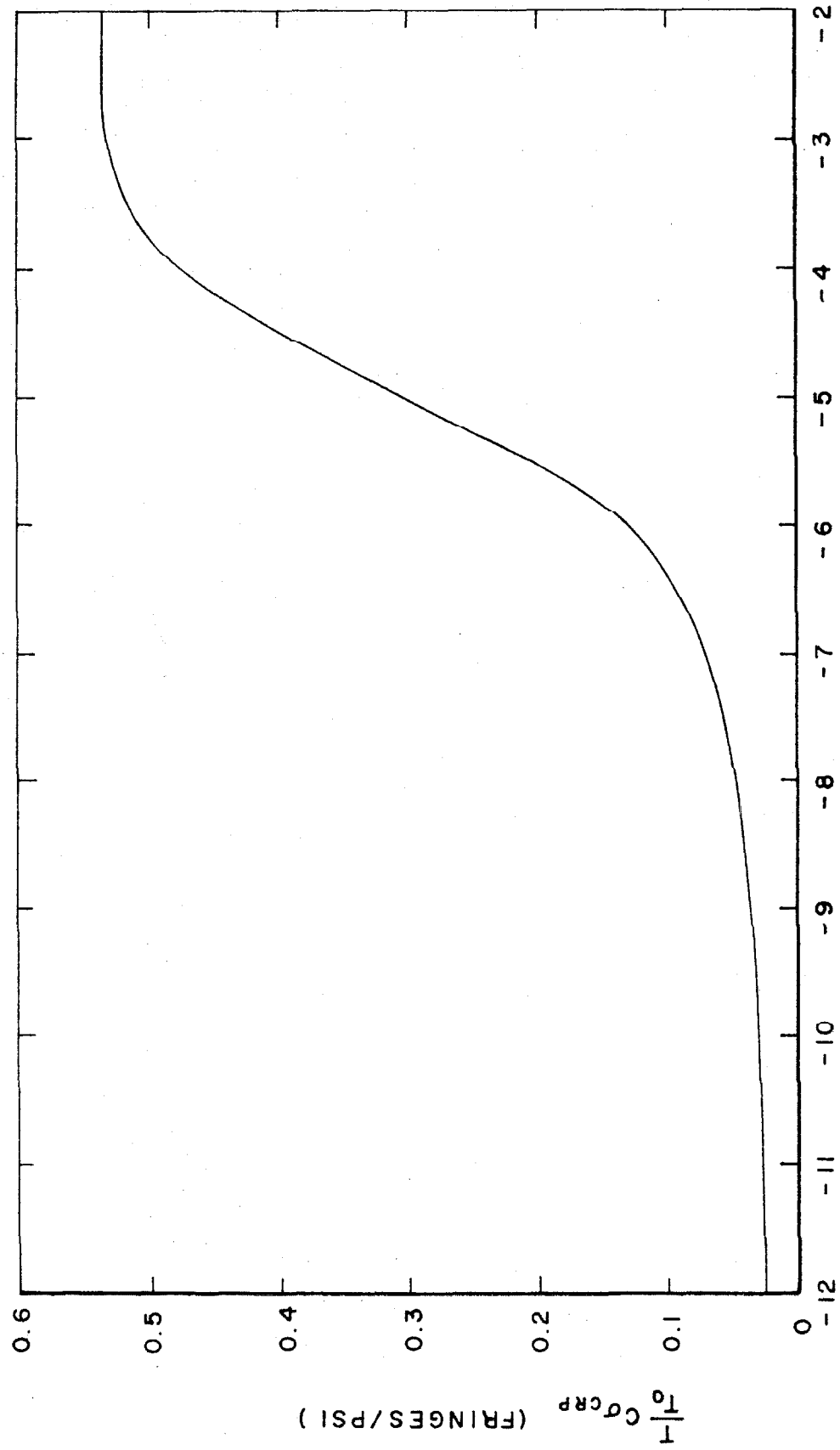

FIG. 23 CREEP BIREFRINGENCE-STRESS COEFFICIENT AS A FUNCTION OF REDUCED TIME FOR HYSOL 8705 MATERIAL; h = 1/2 INCH; T_0 = 291°K

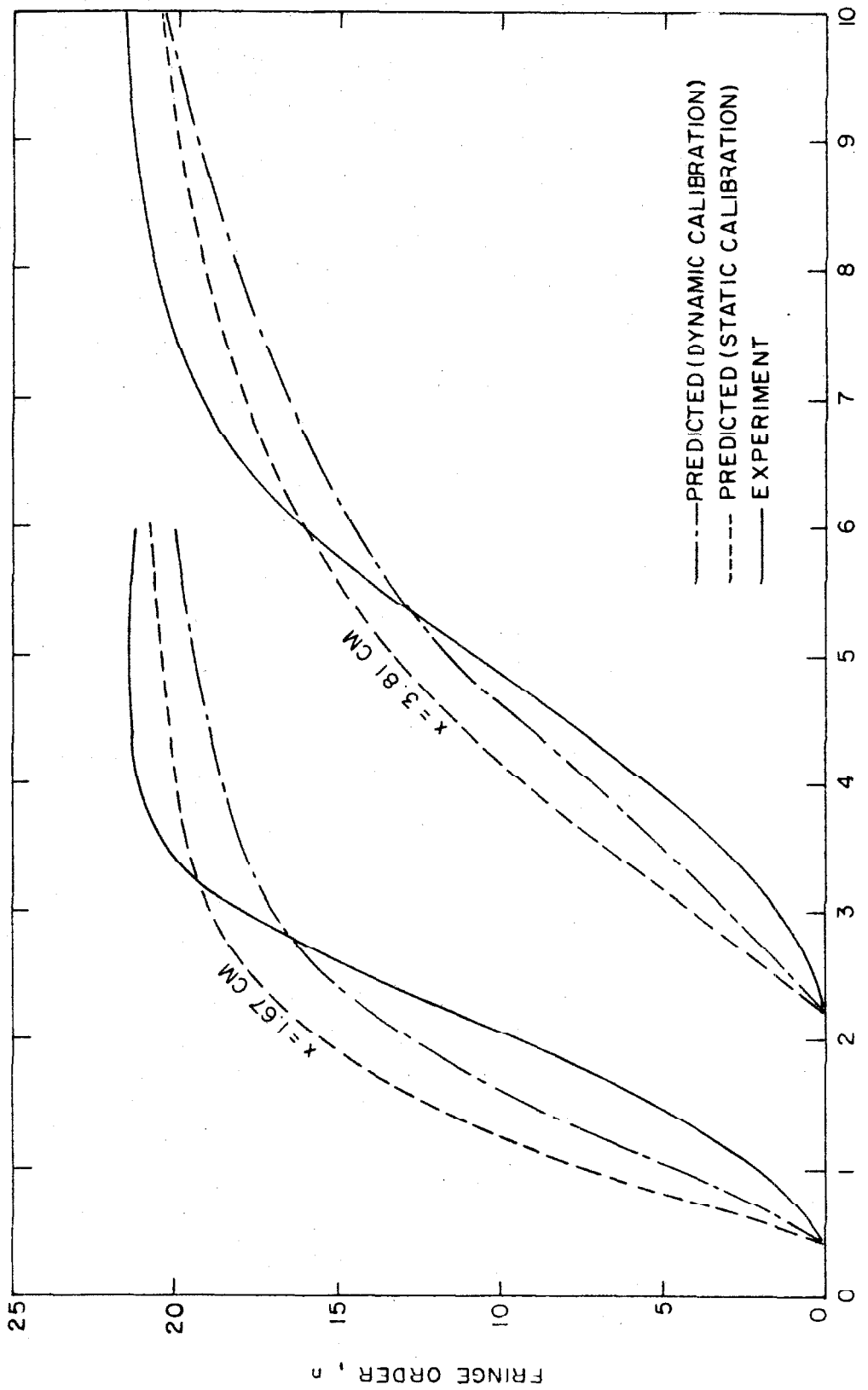

FIG. 24 VARIATION OF FRINGE ORDER AS A FUNCTION OF TIME IN A BAR OF HYSOL 8705 LOADED BY STEP STRESS INPUT ON THE END; T = 291°K

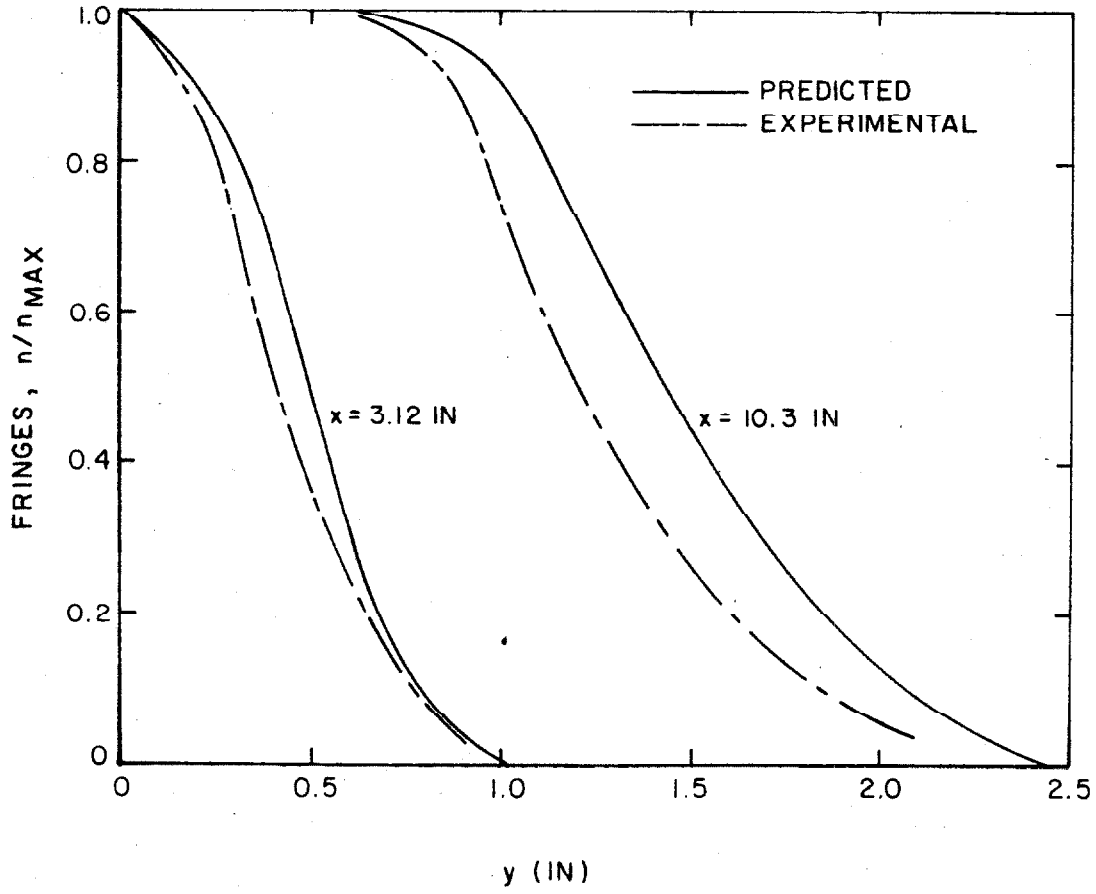

FIG.25 COMPARISON OF PREDICTED AND EXPERIMENTAL FRINGE VARIATION WITH DEPTH FOR WAVE PROPAGATION IN A HYSOL 8705 PLATE LOADED BY A SHOCK WAVE MOVING ON THE FREE SURFACE.

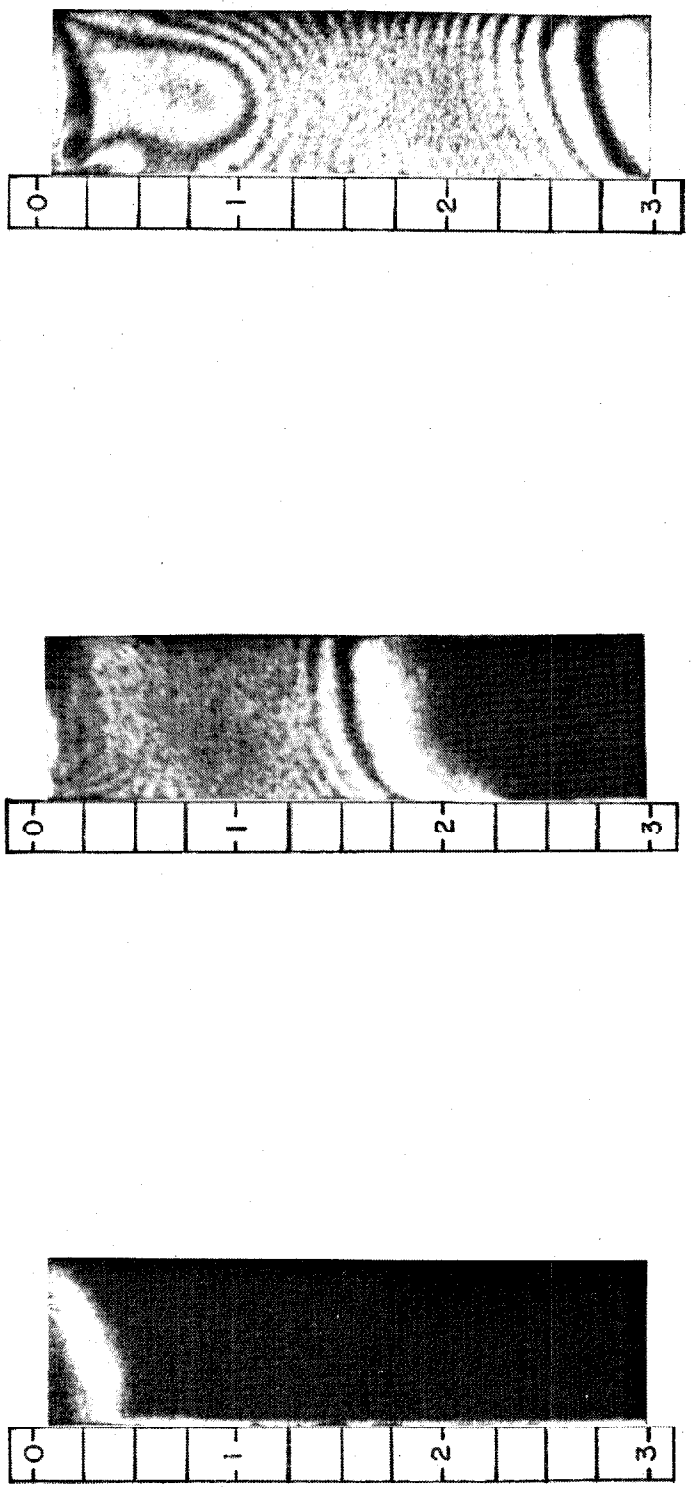

FIG. 26 DYNAMIC FRINGE PATTERNS IN A 0.365 INCH THICK BAR OF HYSOL 8705 MATERIAL AFTER SHOCK WAVE IMPACT ON UPPER END (DISTANCES SHOWN IN INCHES)

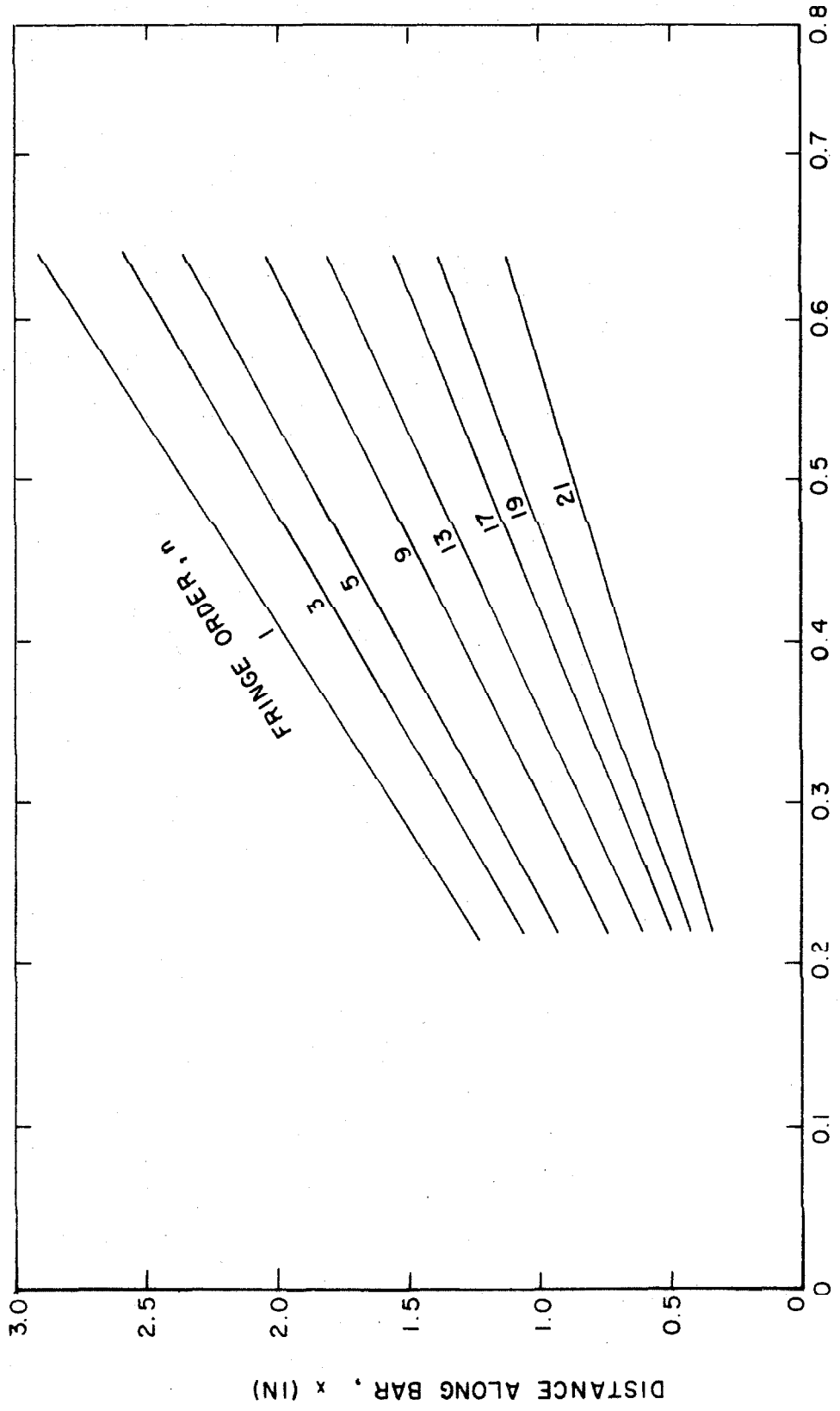

FIG.27 FRINGE ORDER AS A FUNCTION OF TIME FOR A BAR OF HYSOL 8705 MATERIAL SUBJECTED TO SHOCK WAVE LOADING ON THE END

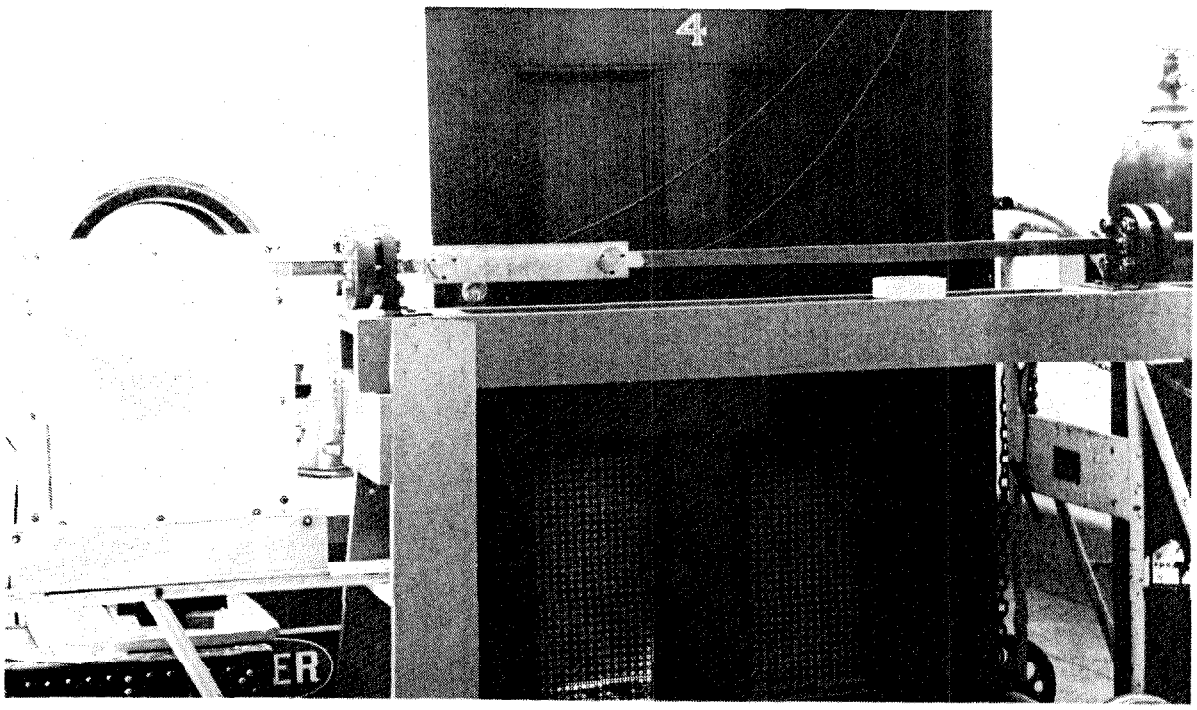

FIG.28 SHOCK TUBE WITH RESISTANCE THERMOMETER PICKUPS AND MODEL HOLDER (LEFT) CONTAINING RECTANGULAR HYSOL 8705 MODEL

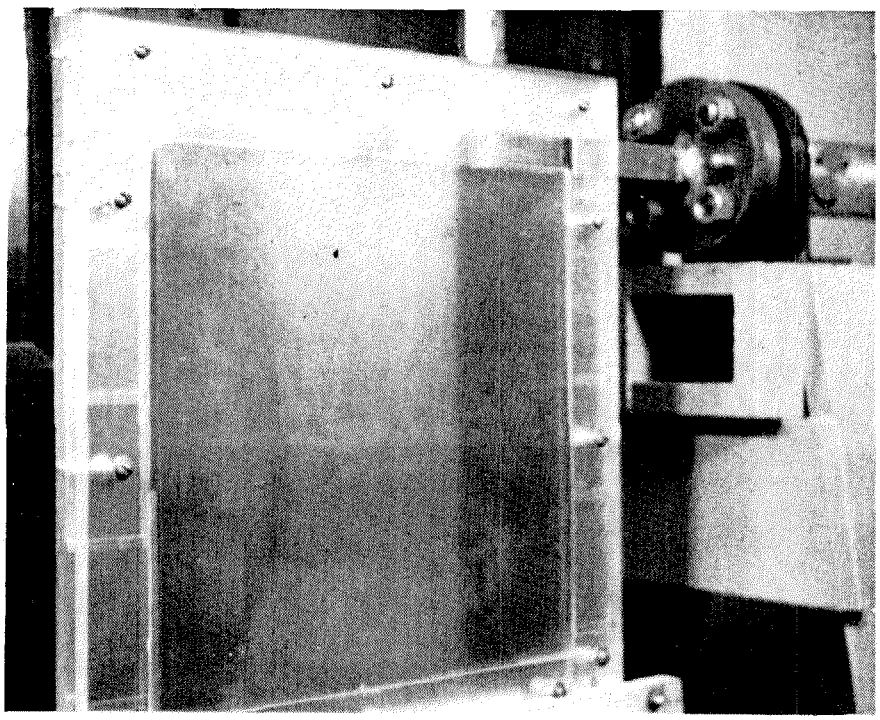

FIG.29 CLOSE-UP OF MODEL IN ITS HOLDER

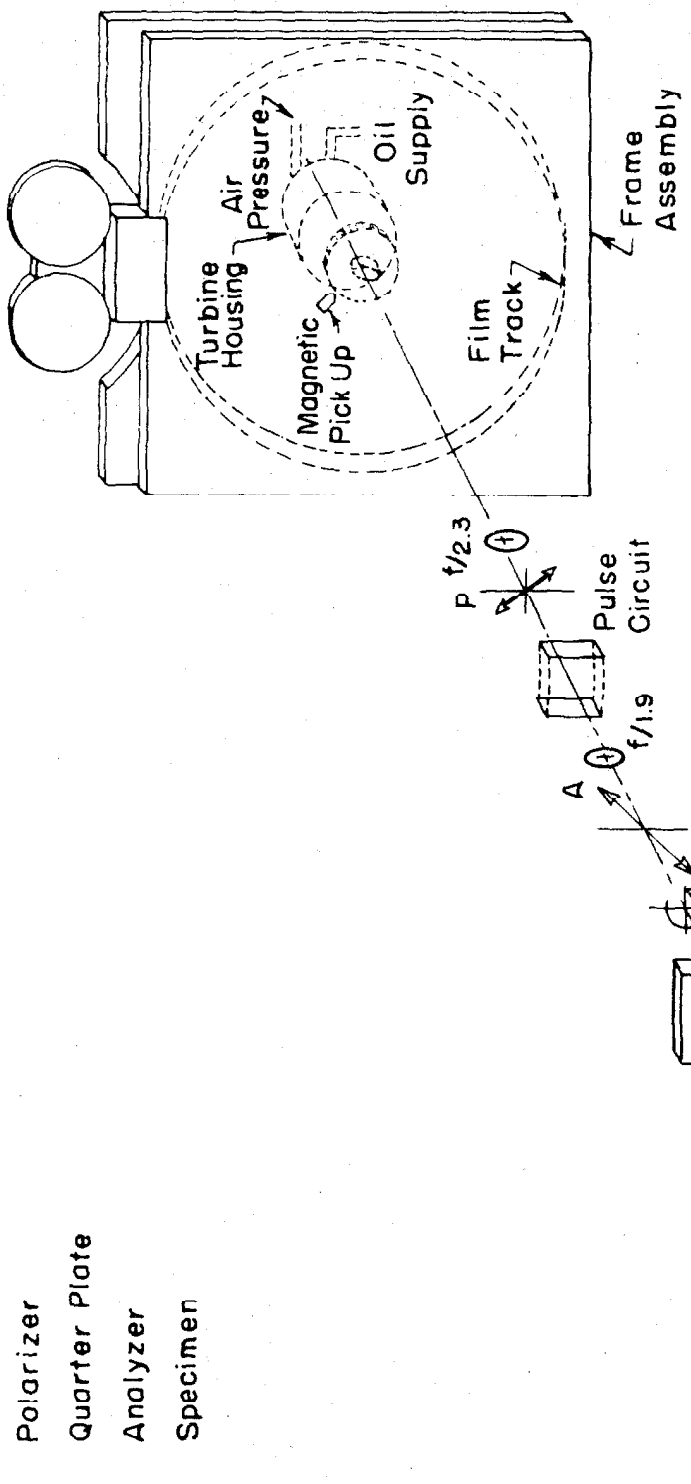

FIG.30 SCHEMATIC LAYOUT OF HIGH SPEED CAMERA ASSEMBLY

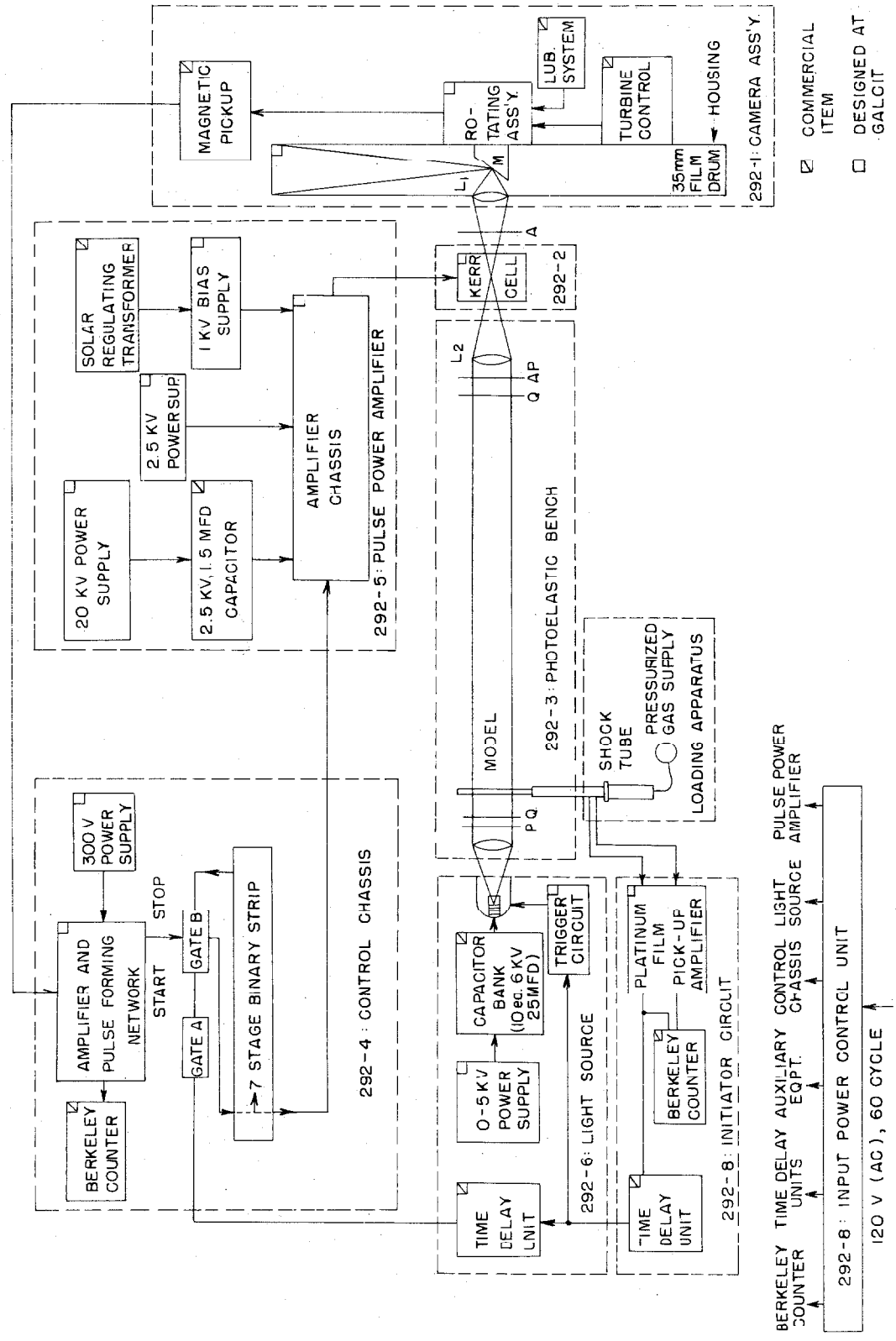

FIG. 31 BLOCK DIAGRAM OF HIGH SPEED PHOTOELASTIC CAMERA EQUIPPED FOR SHOCK TUBE LOADING OF MODEL

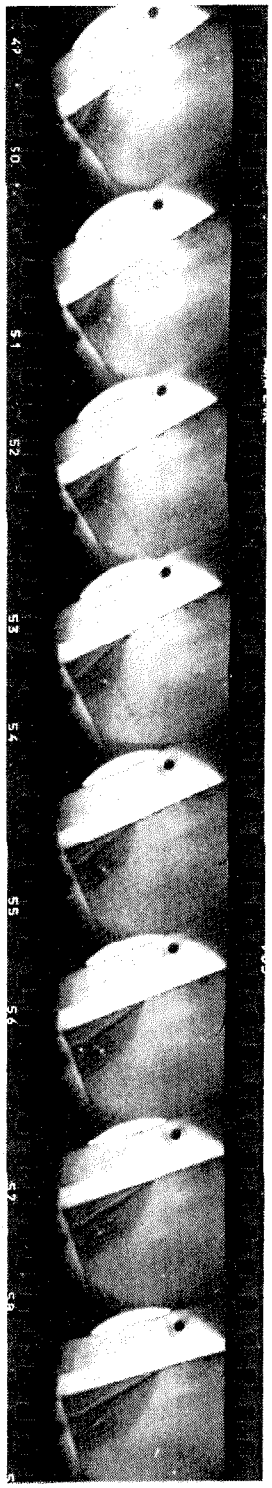

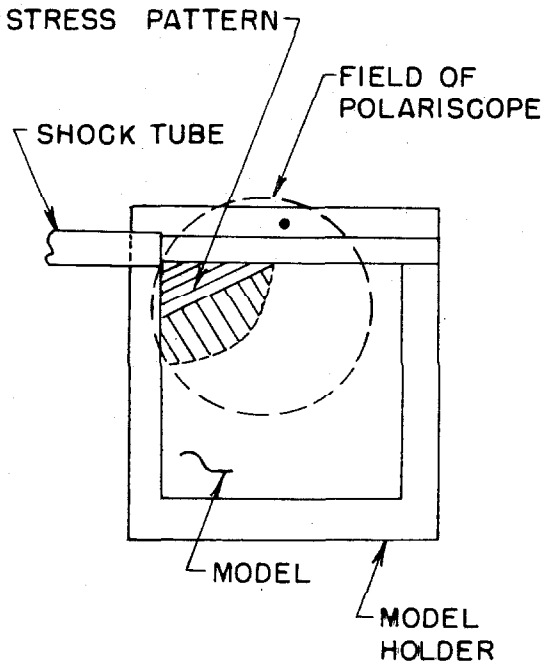

MODEL: HYSOL 8705, URETHANE RUBBER COMPOUND, 1/2" THICK

FRAMING RATE: 72,000 FRAMES/SEC

LOAD: SHOCK WAVE PASSING OVER FREE SURFACE

POLARISCOPE: LIGHT FIELD

FIG. 32 DYNAMIC FRINGE PATTERNS ASSOCIATED WITH STRESS WAVE PROPAGATION IN RECTANGULAR THIN PLATE OF VISCOELASTIC MATERIAL

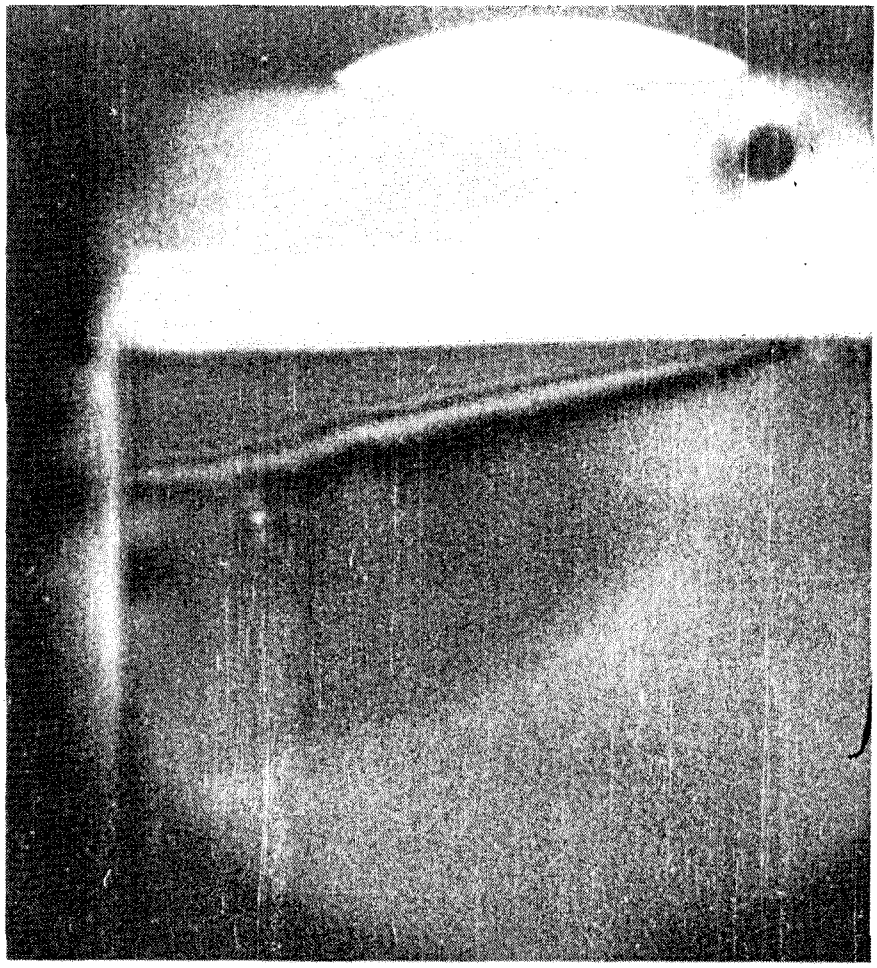

FIG. 33 ENLARGED VIEW OF A SINGLE FRAME AT $t = 250\ \mu$ SEC FROM THE FILM STRIP OF FIG. 32